N° d'ordre : 3800

THÈSE

PRÉSENTÉE A

L'UNIVERSITÉ BORDEAUX 1

ÉCOLE DOCTORALE DES SCIENCES PHYSIQUES ET DE L'INGÉNIEUR

Par Arnaud ROYON

POUR OBTENIR LE GRADE DE

DOCTEUR

SPÉCIALITÉ : LASERS ET MATIÈRE ET NANOSCIENCES

Structuration non-linéaire de verres oxydes par laser femtoseconde dans le proche infrarouge

Soutenue le : mercredi 17 juin 2009

Après avis de :

Mme. Kathleen RICHARDSON	Professeur, Clemson University (USA)	Rapporteur
M. Bertrand POUMELLEC	Directeur de Recherches, Université Paris-Sud XI	Rapporteur

Devant la commission d'examen formée de :

M. Laurent SARGER	Professeur, Université de Bordeaux 1	Président
M. Lionel CANIONI	Professeur, Université de Bordeaux 1	Directeur de thèse
M. Martin RICHARDSON	Professeur, University of Central Florida (USA)	Directeur de thèse
M. Eric AUDOUARD	Professeur, Université Jean Monnet	Examinateur

NONLINEAR FEMTOSECOND NEAR INFRARED LASER STRUCTURING IN OXIDE GLASSES

by

ARNAUD ROYON
B.S. University of Bordeaux 1, 2002
M.S. University of Bordeaux 1, 2004

A dissertation submitted in partial fulfillment of the requirements
for the degree of Doctor of Philosophy in Optics
in the College of Optics and Photonics
at the University of Central Florida
Orlando, Florida

Spring Term
2009

Major Professors: Martin C. Richardson and Lionel Canioni

ABSTRACT

Three-dimensional femtosecond laser structuring has a growing interest because of its ease of implementation and the numerous possible applications in the domain of photonic components. Structures such as waveguides, diffraction gratings, optical memories or photonic crystals can be fabricated thanks to this technique. Its use with oxide glasses is promising because of several advantages; they are resistant to flux and ageing, their chemical composition can easily be changed to fit the well-defined requirements of an application. They can already be found in Raman amplifiers, optical fibers, fiber lasers, and other devices.

This thesis is based on two axes. The first axis consists in characterizing the linear and nonlinear optical properties of bulk vitreous materials in order to optimize their composition with a particular application in view. Within this context, the nonlinear optical properties, their physical origins (electronic and nuclear) as well as their characteristic response times (from a few femtoseconds to a few hundreds of picoseconds) are described within the Born-Oppenheimer approximation. Fused silica and several sodium-borophosphate glasses containing different concentrations in niobium oxide have been studied. Results show that the nonlinear optical properties of fused silica are mainly from electronic origin, whereas in the sodium-borophosphate glasses, the contribution from nuclear origin becomes predominant when the concentration of niobium oxide exceeds 30%.

The second axis is based on the structuring of materials. Three commercially available fused silica samples presenting different fabrication conditions (therefore distinct impurity levels) and irradiated with a near infrared femtosecond laser have been studied. The laser induced defects have been identified by means of several spectroscopic techniques. They show the formation of color centers as well as a densification inside the irradiated area. Their linear refractive index and nonlinear third-order susceptibility properties have been measured.

Moreover, the structuring of fused silica at the subwavelength scale into “nanogratings” is observed and the form of birefringence induced by these structures is discussed.

In addition to the fused silica samples, several oxide glasses presenting very distinct chemical compositions have been studied. A sodium-borophosphate glass containing niobium oxide exhibits micro-cracks and nano-crystallites following irradiation. A silicate glass with or without a silver component reveals fluorescent rings or “nanograting” structures. A zinc phosphate glass containing silver also presents fluorescent ring structures, with a size of the order of 80 nm, well below the diffraction limit. Pump-probe microscope techniques have been performed on this glass to investigate the laser-glass interaction. The absorption mechanism is determined to be four-photon absorption. The generated free electron density is $\sim 10^{17}$ cm^{-3}, which suggests the conclusion that an electron gas rather than a plasma is formed during the laser irradiation.

A mes parents…

A mon frère…

A ma famille et mes amis…

A Mamie Edith.

ACKNOWLEDGMENTS

This thesis took place within the framework of a cotutelle degree exchange program between the CREOL at the University of Central Florida (USA) and the CPMOH at the University of Bordeaux 1 (France). It lasted five years, with approximately an equal time spent at each institution. At the end of my study, I will receive two doctorate diplomas, one in the field of Optics from UCF and another in Lasers, Materials and Nanosciences from UB1. Within this context, I had two advisors, one at CREOL and one at CPMOH.

First, I would like to thank my CREOL advisor, Dr. Martin C. Richardson, for having provided an ideal environment to conduct scientific research, for having permitted me to discover another academic and research system than the French one, and for having been my dissertation committee chair. The freedom of action he gave me enabled me to acquire an essential quality in Sciences: autonomy.

Then, I would like to acknowledge my CPMOH advisor, Dr. Lionel Canioni, for having given the direction of this thesis and for having been my dissertation committee co-chair. The numerous ideas he shared with me enabled me to get a much wider field of view in research than the narrow topic of this thesis. Even though many experiments did not work, the obtained experience will be very priceless in my scientific future. I would like to highlight as well his permanent good mood and his jovial nature. It has really been a pleasure to work with him and I consider him not only as an adviser, but also as a friend. La prochaine fois que tu viens me rendre visite à Orlando, je te promets qu'on pourra aller à Playa Linda.

I thank my advisory committee members, Dr. Kathleen Richardson, Dr. David J. Hagan and Dr. Demetrios Christodoulides (for the US defense) as well as Dr. Bertrand Poumellec and Dr. Eric Audouard (for the French defense) for their constructive remarks on my thesis work and for sharing their expertise and knowledge in Chemistry and Optics.

I address my acknowledgements to Dr. Laurent Sarger, the initiator of the exchange program on the French side, in collaboration with Dr. Martin C. Richardson and Dr. Kathleen Richardson on the US side. He is the person who permitted me to perform an internship at CREOL during my first year of master within the framework of the REU program. This period made me enjoy working in a laboratory and was the bend in my studies towards research. He is also the person not to ask when you look for an accommodation to attempt a conference (*cf.* CLEO 2005 in Baltimore and CLEO 2008 in San Jose).

I thank the technical and administrative staff of CREOL and CPMOH. Without their help, this thesis would not have been possible.

I thank the "Laser Plasma Laboratory" group at CREOL, and more particularly the "Laser Materials Processing" team, composed of Ji Yeon Choi, Troy Anderson and Mark Ramme, for welcoming me among them and for sharing their knowledge with me.

I express gratitude to the members of the "Matériaux en Régime Femtoseconde" group at CPMOH. Thanks to the permanent members Dr. Bruno Bousquet (alias "El Bruno"), Dr. Patrick Mounaix (alias "Patoche"), Dr. Jean-Christophe Delagnes (alias "Jean-Christophe"). We really have to find another group name, guys!!! Thanks to the past Ph.D. students and non-permanent members: Arnaud Brocas (alias "Senior", my THG microscopy mentor), Stéphane Santran (alias "El Stephano", my triathlon tutor), Jean-Baptiste Sirven (alias "Jay-Bi", my first guitar teacher), Aurélie Moreau, Patrice Nagtegaele, Guillaume Guimbretière (Houhou Hellwarth) and Abdel Fatimy. Thanks to the current Ph.D. students and non-permanent members: Edwin Nguema Agnandji (alias "Ed"), Grégoire Travaillé (alias "El Grego"), Ayesha Younus, Riad Yahiaoui and Amina Ismaël (alias "heart breaker"). Special thanks to Matthieu Bellec (alias "Belloc" or "Pious"), with whom looking for the "nanos" for hours and hours in complete darkness while the weather outside was hot and sunny was really a pleasure.

I acknowledge the cooks (sorry, the chemists) of the “Matériaux pour l’Optique” group at ICMCB. Thanks to the permanent members Dr. Thierry Cardinal and Dr. Evelyne Fargin and the Ph.D. students Frédéric Rocco, Clément Maurel, Nicolas Nowak, Aurélien Delestre and Kevin Bourhis. For the two latter, you should really spend less time on Facebook, guys!!!

I acknowledge the permanent members of the “Spectroscopie Moléculaire” group at ISM: Dr. Michel Couzi, Vincent Rodriguez and Frédéric Adamietz.

I would like to thank all the CPMOH and CREOL students I have met during my Ph.D.: Mickaël Hemmer (alias “Pupuce”), Tim McComb, Umar Piracha (guitar tonight?), Azer Reza, Ibrahim Ozdur, Leo Siiman (the most French of the Americans), Oleksiy Andrusyak, David Haefner, Clarisse Mazuir (what is the recipe of the English cream?), Marco Melino (the only person who could beat me at poker, except the twenty others in Las Vegas) and Florien Fournier (thanks for the apartment).

At the beginning of this thesis, for one month, I had the chance to perform a doctorate internship in Seoul (South Korea), in the Nonlinear Optics group lead by Dr. Seung-Han Park, at Yonsei University. This stay was supported by the French embassy of South Korea through the STAR program which aims to show the Korean research system to French scientists in order to initiate collaborations. For this unforgettable experience, I would like to acknowledge the French embassy of South Korea for giving me the opportunity to visit this country and Dr. Seung Han Park and his team for their warm welcome.

I thank the people I have met during my stays in Orlando, who I did not know before and who have become friends. Most of them were REU students who spent a few months in the USA: Etienne Puyoo (alias “Pouyoute”), Gaetan Calbris (alias Guéguette”), Axel Quinsac (de patates), Teddy Péponnet (alias “Pépoune”), Franck Brückner (alias “Frankiki”) and

Darragh Ryan (the most French from the Irish guys, because he cried when the French soccer team was defeated by the Italian one during the world cup in Germany).

I thank the French connection of Orlando. I have had so many good memories with you. Just for that, I do not regret having performed my thesis in cotutelle. They are: Charline Motir (alias “Choupie Choupe”), Marie Laure Anne (alias “Rizadinha”), Christophe Brandily (alias “un Branditof, des Branditeef”), Julien and Séverine Lumeau, Clémence Jollivet (un glaçon pour te rafraîchir ?), François Labaye (alias “Fanfan la banane”), Gautier Papon (un étudiant plein d’avenir…), Sandrine Ricaud (qui se débrouille pas trop mal au tennis), Mickaël Faugeron (alias “Coloc”), Anne-Claire Coignard (alias “la Ptite”) and the Connemara team (Adrien “Crevette” Chlot, Gérald “Jay-Jay” Favereaud and Guillaume “Nénette” Cabrol) for having visited me.

Thanks to the team-mates of the soccer team Sciences 1 and to the coaches Bernard Péjot (alias “Nanard”) and Robert Varachaud (alias “Roro”). After three following lost finals, we finally succeeded to win the academic championship, vintage 2008-2009, against our eternal opponent, Bordeaux 4.

Finally, and above everything, I would like to express my full gratitude to my parents, Bernard and Annie, for their continuous sustain, to my brother Romain for having supported me during my studies, and to my family. THANK YOU.

Oh I was forgetting. I acknowledge myself too, of course.

TABLE OF CONTENTS

LIST OF ACRONYMS

AFM	Atomic Force Microscopy
BBO	Barium -Borate-Oxygen
BOA	Born-Oppenheimer Approximation
CFM	Confocal Fluorescence Microscopy
CGS	Centimeter Gram Second
CPMOH	Centre de Physique Moléculaire, Optique et Hertzienne
CREOL	Center for Research and Education in Optics and Lasers
FWHM	Full Width at Half Maximum
HW1/e	Hall Width at 1/e of the maximum
ICMCB	Institut de Chimie de la Matière Condensée de Bordeaux
IR	Infrared
ISM	Institut des Sciences Moléculaires
KDP	Potassium-Dihydrogen-Phosphate
LPL	Laser Plasma Laboratory
NBOHC	Non-Bridging Oxygen Hole Center
NIR	Near Infrared
ODC	Oxygen-Deficient Center
OKE	Optical Kerr Effect
PMT	Photomultiplier Tube
REU	Research Experiences for Undergraduates
SEM	Scanning Electron Microscopy
SI	Système International
STAR	Science and Technology Amical Relationships
TBS	Tungsten Bronze Structure
TE	Transverse Electric
THG	Third-Harmonic Generation
TM	Transverse Magnetic
UB	Université de Bordeaux
UB1	Université de Bordeaux 1
UCF	University of Central Florida
UV	Ultraviolet
2D	Two Dimensions
3D	Three Dimensions

GLOSSARY

Fundamental constants

c	Speed of light in the vacuum (299792458 $m.s^{-1}$)
ε_0	Dielectric permittivity in the vacuum ($8.85418782 \times 10^{-12}$ $F.m^{-1}$)
μ_0	Magnetic permeability in the vacuum ($4\pi \times 10^{-7}$ $H.m^{-1}$)
h	Planck's constant (6.626176×10^{-34} J.s)
k_B	Boltzmann's constant (1.380662×10^{-23} $J.K^{-1}$)
e	Electron charge ($1.6021892 \times 10^{-19}$ C)
m_e	Electron rest mass ($0.9109534 \times 10^{-30}$ kg)
eV	Electron volt (1eV = $1.6021892 \times 10^{-19}$ J)

Notations

D	Electric displacement ($C.m^{-2}$)
E	Electric field ($V.m^{-1}$)
B	Magnetic induction ($Wb.m^{-2}$ or T)
H	Magnetic field ($A.m^{-1}$)
M	Magnetization ($A.m^{-1}$)
P	Polarization ($C.m^{-2}$)
J	Current density ($A.m^{-2}$)
J	Conduction current density ($A.m^{-2}$)
J	Magnetism current density ($A.m^{-2}$)
J	Polarization current density ($A.m^{-2}$)
ρ_V	Volume charge density ($C.m^{-3}$)
σ	Conductivity ($S.m^{-1}$)
P_L, P_{NL}	Linear and nonlinear polarizations ($C.m^{-2}$)
$P^{(n)}$	n^{th}-order polarization ($C.m^{-2}$)
$R^{(n)}$	n^{th}-order response function
$\chi^{(n)}$	n^{th}-order dielectric susceptibility
$P^{(3)}_{elec}$, $P^{(3)}_{nuc}$	Electronic and nuclear third-order polarizations ($C.m^{-2}$)
$\chi^{(1)}$, $\chi^{(2)}$, $\chi^{(3)}$	First-order (dimensionless), second-order ($m.V^{-1}$) and third-order ($m^2.V^{-2}$) dielectric susceptibilities
$R^{(1)}$, $R^{(2)}$, $R^{(3)}$	First-order (s^{-1}), second-order ($m.V^{-1}.s^{-1}$) and third-order ($m^2.V^{-2}.s^{-1}$) response functions
$\sigma^{(1)}$, $\sigma^{(3)}$	Electronic first-order (dimensionless) and third-order ($m^2.V^{-2}$) dielectric susceptibilities
$D^{(3)}$	Nuclear third-order dielectric susceptibility ($m^2.V^{-2}$)
$d^{(3)}$	Nuclear third-order response function ($m^2.V^{-2}.s^{-1}$)
k_ω, $k_{3\omega}$	Wave vectors ($rad.m^{-1}$) of the fundamental and third-harmonic beams
Δk	Phase mismatch ($rad.m^{-1}$)

A_{0_ω}, $A_{0\_3\omega}$	Electric field magnitude ($V.m^{-1}$) of the fundamental and third-harmonic beams
I_{ω}, $I_{3\omega}$	Irradiance ($W.m^{-2}$) of the fundamental and third-harmonic beams
n_{ω}, $n_{3\omega}$	Refractive indices (dimensionless) at the angular frequencies. ω and 3ω
T_{ω}, $T_{3\omega}$	Fresnel transmission coefficients (dimensionless) at the angular frequencies. ω and 3ω
ρ	Radial coordinate (m)
ξ	Normalized longitudinal coordinate (dimensionless)
z_R	Rayleigh length (m)
b	Confocal parameter (m)
λ_0	Wavelength (m) in the vacuum
λ	Wavelength (m) in the medium
λ_c	Cutoff wavelength (m) of the glass, defined as the crossing between the wavelength axis and the continuation of the absorption front
ω	Angular frequency ($rad.s^{-1}$)
ω_0	Resonance angular frequency ($rad.s^{-1}$)
ω_P	Plasma angular frequency ($rad.s^{-1}$)
$J_{3\omega}$	Third-harmonic effective interaction length (m)
z_0	Position (m) of the entrance of the nonlinear medium
x, y, z	Cartesian coordinates (m)
r	Position vector (m)
t	Time (s)
T	Temperature (K)
m	Permanent dipole moment (C.m)
α	Polarizability ($C^2.m^2.J^{-1}$)
β	First-order hyperpolarizability ($C^3.m^3.J^{-2}$)
γ	Second-order hyperpolarizability ($C^4.m^4.J^{-3}$)
N_V	Electron density (m^{-3}) in the valence band
N_C	Electron density (m^{-3}) in the conduction band (or free electron density)
N_{cr}	Critical electron density (m^{-3})
τ_1	Delay (s) between the reference and the probe pulses (without pump)
τ_2	Delay (s) between the reference and the probe pulses (with pump)
E_g	Band gap energy (J)
τ_c	Electron collision time (s)
$\Delta\lambda_1$	Pseudo-period (m) of the spectral fringes (without pump)
$\Delta\lambda_2$	Pseudo-period (m) of the spectral fringes (with pump)

$\Delta\lambda$	Shift (m) of the spectral fringes (with pump) with respect to the reference fringes (without pump)
n_0	Linear refractive index (dimensionless)
n_2	Nonlinear refractive index ($m^2.W^{-1}$)
α_0	Linear absorption coefficient (m^{-1})
α_2	Nonlinear absorption coefficient ($m.W^{-1}$)
v	Writing speed ($m.s^{-1}$)
NA	Numerical aperture (dimensionless)
w_0	Beam waist (m)
P_{av}	Average power (W)
P_{peak}	Peak power (W)
E_p	Pulse energy (J)
F	Fluence ($J.m^{-2}$)
I	Irradiance ($W.m^{-2}$)
D	Dose ($J.m^{-3}$)
τ_p	Pulse duration (s)
R	Laser repetition rate (Hz)
N	Number of pulses (dimensionless)
τ_D	Thermal diffusion time (s)
τ_ρ	Electrostrictive characteristic time (s)

LIST OF FIGURES

LIST OF TABLES

CHAPTER ONE: INTRODUCTION

The nonlinear optical properties of materials play a role in many applications, ranging from telecommunications to laser sources, through laser material processing. For the conception of all-optical systems in information technology (modulator, detector, amplifier, switch…), the materials must exhibit high nonlinearities. On the contrary, for the information transport through optical fibers or the fabrication of fiber laser sources, low nonlinearities are essential to prevent self-focusing, self-phase modulation, Raman and Brillouin scatterings. Between both, in laser material processing, materials must present a trade-off between a sufficient multiphoton absorption and a not too important photosensitivity. From all these examples, it is clear that the intrinsic properties of the nonlinear materials must be optimized depending on the application in view.

Transparent optical glasses exhibiting nonlinearity in the visible/near infrared (NIR) range have been examined far from resonance in order to avoid significant multiphoton absorption. These glasses are of interest and have been evaluated as possible candidates for optical switching. Among all vitreous systems, oxide glasses containing a large amount of heavy atoms (*i.e.* highly polarizable species) have attracted attention since they exhibit significant nonlinearity for use in the near infrared telecommunication windows and appear to be promising candidates as Raman gain media [Mil88] [Ste03] [Riv04] [Riv05].

Within the Born-Oppenheimer approximation, which indicates that optical pulses shorter than a few hundreds of picoseconds should be considered, the origin of the optical nonlinearity in glasses, far from resonance, is attributed to electronic and nuclear contributions. The electronic response is related to the spontaneous nonlinear distortion of the electronic distribution around the nuclei while the nuclear response is due to a slower optical-field-induced change arising from the motions of the nuclei [Hel75]. It is known that these

two contributions have distinctly different relaxation times, with the first (electronic) being less than one femtosecond whereas the second process (nuclear) is on the order of several hundreds of femtoseconds to a few picoseconds. In 1975, Hellwarth *et al.* [Hel75] showed that the nuclear contribution to the nonlinear refractive index of some glasses is not negligible, being as high as up to 15 - 30% of the total nonlinearity, depending on the glass composition.

The knowledge of the electronic and nuclear contributions to the nonlinear response as well as its magnitude is crucial for many telecommunication applications. For fast all-optical switching and soliton propagation in optical fibers, the instantaneous contribution will be favored. On the contrary, for these applications, the non-instantaneous contributions are potential sources of limitation in high bit-rate transmission systems. However, for Raman amplification, one would tend to favor the nuclear contribution. The nuclear contribution can also be used to modulate the nonlinear response with varying the pulse duration.

On the other hand, progress in femtosecond laser direct writing permit now to fabricate devices such as waveguides [Dav96], gratings [Hir98], memories [Gle96], photonic band gap crystals [Sun99], 3D microstructures [Mas03] and functional crystals [Dai07]. The application of this technique to glasses containing nanocomposites or nanocrystallites is promising. Indeed, these glasses present incontrovertible advantages. Their ease of implementation, their good resistance to flux and ageing and their flexibility of composition give them a high adaptability. The possibility to dope these vitreous matrices with photosensitive nano-components elaborated in situ permits the use of a femtosecond laser to structure and functionalize these materials with a high spatial resolution.

On a fundamental point of view, few is known about femtosecond laser-material interaction. A lot of work has been performed on glasses, mainly on fused silica, to investigate the induced structural changes and their relation with the optical properties of the

exposed regions [Zou05] [Zou06]. But the characterization was carried out after irradiation, at a wavelength scale, ignoring the dynamic of the interaction. Moreover, it has been revealed recently that the irradiation of glasses could lead to a self-organized sub-wavelength structuring, so called “nanograting” structures [Shi03], complicating even more the picture of the phenomenon. Thus, real time measurements still need to be performed to get an overall view of the laser-material interaction.

This work follows in the footsteps of Arnaud Zoubir who opened the way to femtosecond laser direct writing [Zou04] in the LPL group and Clara Rivero who investigated new oxide glasses for Raman amplification [Riv05bis]. It is in the framework of a collaboration between the University of Central Florida (USA) and the University of Bordeaux 1 (France). Mastery in femtosecond laser direct writing and plasma characterizations are centered at CREOL whereas competences in synthesis, metrology and modeling are gathered at the University of Bordeaux 1 (CPMOH, ICMCB and ISM). This collaboration is part of a cotutelle degree exchange program between both universities, which has already supported the two students cited above and is currently integrated by three more students, Jiyeon Choi, Troy Anderson and myself.

This dissertation discusses results about the nonlinear characterization and structuring of different oxide glasses. It is organized in two main parts. Part A concerns the investigation of the nonlinear optical properties of bulk oxide glasses. It deals with the theoretical and experimental procedures enabling to characterize a glass in terms of its nonlinear optical properties. Chapter two gives background information about nonlinear optics, necessary for the understanding of this manuscript. Chapter three describes the different physical mechanisms involved in the nonlinear response of a material. It will be shown that the laser properties and the origin of the physical phenomena strongly influence the magnitude and the dynamics of the nonlinear optical properties. In this thesis, femtosecond lasers have been

used. The nonlinear optical properties can then be described within the framework of the Born-Oppenheimer approximation. Chapter four presents this approximation, as it was suggested by Hellwarth in his well-known paper [Hel77], and a very useful relation permitting to predict the nuclear third-order susceptibility from Raman spectroscopy. Chapter five describes two degenerate third-order processes, third-harmonic generation and optical Kerr effect, within the context of this approximation. Two techniques based on these processes, third-harmonic generation microscopy and pump-probe experiment, have been used to measure the nonlinear optical properties of two glass families, namely fused silica and sodium-borophosphate-niobium glass. Chapter six shows the application of Hellwarth's model to these glasses, for which the magnitude and the relative strength of the instantaneous and non-instantaneous contributions to the nonlinear response are investigated. This nonlinear characterization, presented in Part A, is used as a springboard towards femtosecond-laser-structuring, discussed in Part B. Chapter seven deals with the mechanisms involved in the interaction of a femtosecond laser pulse train with a glass as well as the different regimes of photo-induced modifications. Femtosecond laser exposed fused silica has been investigated at both micron and submicron scales. Chapter eight gives a complete characterization of three different fused silica samples presenting different impurity levels for comparison purposes. The links between the variation in the optical properties, the initial impurity levels and the photo-induced structures are investigated. To get a larger view about laser-material interaction, other oxide glasses (sodium-borophosphate-niobium, silicate, silver-doped silicate and silver zinc phosphate) have been investigated. Chapter nine shows the behavior of these glasses to femtosecond laser irradiation. In addition, it presents microscopy and pump-probe techniques applied to a photosensitive glass, in order to investigate the properties of the laser induced electron gas, more particularly the free electron density, the ionization mechanisms

involved in the structuring and the influence of the cumulative effects. Chapter ten gives a general conclusion and a summary of all the findings and discusses about future perspectives.

PART ONE: NONLINEAR OPTICAL CHARACTERIZATION

CHAPTER TWO: NONLINEAR OPTICS BACKGROUND

This chapter aims to give the formalism of nonlinear optics. The linear and nonlinear polarizations and susceptibilities are given in their most general form, as well as their properties. A reminder of the definition of the Fourier transform as it is used in nonlinear optics is also supplied because it will appear later in the manuscript.

2.1. The Fourier transform

The Fourier transform is a powerful mathematical tool permitting to pass from the time domain to the frequency domain, and vice-versa. There are several ways to write the Fourier transform. In Optics, the Fourier transform and its inverse are defined as following, for any function f

$$\begin{cases} F(\omega) = \int_{-\infty}^{+\infty} f(t) \exp(i\omega t) dt \\ f(t) = \frac{1}{2\pi} \int_{-\infty}^{+\infty} F(\omega) \exp(-i\omega t) d\omega \end{cases} \quad \text{(A.2.1)}$$

Thus, the direct and inverse Fourier transforms of the electric field and the polarization are given by

$$\begin{cases} \vec{E}_i(\omega) = \int_{-\infty}^{+\infty} \vec{E}_i(t) \exp(i\omega t) dt \\ \vec{E}_i(t) = \frac{1}{2\pi} \int_{-\infty}^{+\infty} \vec{E}_i(\omega) \exp(-i\omega t) d\omega \end{cases} \quad \text{(A.2.2)}$$

$$\begin{cases} \vec{P}_i(\omega) = \int_{-\infty}^{+\infty} \vec{P}_i(t) \exp(i\omega t) dt \\ \vec{P}_i(t) = \frac{1}{2\pi} \int_{-\infty}^{+\infty} \vec{P}_i(\omega) \exp(-i\omega t) d\omega \end{cases} \quad \text{(A.2.3)}$$

However, the Fourier transform of the first-order susceptibility and its inverse, the first-order response function, are written as

$$\begin{cases} \chi_{ij}^{(1)}(\omega) = \int_{-\infty}^{+\infty} R_{ij}^{(1)}(t) \exp(i\omega t) dt \\ R_{ij}^{(1)}(t) = \int_{-\infty}^{+\infty} \chi_{ij}^{(1)}(\omega) \exp(-i\omega t) d\omega \end{cases} \quad \text{(A.2.4)}$$

, without the $1/2\pi$ factor.

This discrepancy is due to the definition of the polarization in the frequency domain, which is the simple product of the first-order susceptibility with the electric field

$$\vec{P}_i(\omega) = \varepsilon_0 \chi_{ij}^{(1)}(\omega) \vec{E}_j(\omega) \quad \text{(A.2.5)}$$

where the Einstein notation of the implicit summation has been used ($a_{ij} b_j = \sum_j a_{ij} b_j$).

2.2. The polarization response of a material

The polarization of a material under the influence of an applied electric field is described in terms of a power series of the field

$$\vec{P}_i(\vec{r};t) = \vec{P}_i^{(0)}(\vec{r};t) + \vec{P}_i^{(1)}(\vec{r};t) + \vec{P}_i^{(2)}(\vec{r};t) + ... + \vec{P}_i^{(n)}(\vec{r};t) + ... \quad \text{(A.2.6)}$$

where $\vec{P}_i^{(0)}(\vec{r};t)$ is independent of the field and would represent the static polarization found in some crystals, $\vec{P}_i^{(1)}(\vec{r};t)$ is linear in the field, $\vec{P}_i^{(2)}(\vec{r};t)$ is quadratic, and so on.

2.2.1. The linear polarization

The most general expression for the linear polarization, with only the assumptions of *homogeneity* of the material and *invariance by time translation*, is in the form

$$\vec{P}_i^{(1)}(\vec{r};t) = \varepsilon_0 \int_V \int_{-\infty}^{t} R_{ij}^{(1)}(\vec{r} - \vec{r}';t - t_1) \vec{E}_j(\vec{r}';t_1) dt_1 d^3\vec{r}' \quad \text{(A.2.7)}$$

where $R_{ij}^{(1)}$ is a second-rank tensor denoted as the first-order response function of the material.

If the response is entirely *local* ($R_{ij}^{(1)} \propto \delta(\vec{r}-\vec{r}')$), which means that the polarization at a position $\vec{r}$ depends only on the value of the electric field at the same position $\vec{r}$, then the linear polarization is written as

$$\vec{P}_i^{(1)}(\vec{r};t) = \varepsilon_0 \int_{-\infty}^{t} R_{ij}^{(1)}(\vec{r};t-t_1)\vec{E}_j(\vec{r};t_1)dt_1 \tag{A.2.8}$$

The *causality principle* states that the effect cannot precede the cause; the polarization at a time t cannot depend on the electric field at future times. This implies that the response function is strictly null when its argument is negative. The linear polarization becomes

$$\vec{P}_i^{(1)}(\vec{r};t) = \varepsilon_0 \int_{0}^{t} R_{ij}^{(1)}(\vec{r};t-t_1)\vec{E}_j(\vec{r};t_1)dt_1 = \varepsilon_0 R_{ij}^{(1)}(t) \otimes \vec{E}_j(t) \tag{A.2.9}$$

Since this last expression is a convolution product, it is natural to pass in the frequency domain, where the linear polarization is a simple product

$$\vec{P}_i(\omega) = \varepsilon_0 \chi_{ij}^{(1)}(-\omega_\sigma;\omega)\vec{E}_j(\omega) \tag{A.2.10}$$

where $\chi_{ij}^{(1)}(-\omega_\sigma;\omega) = \int_{-\infty}^{+\infty} R_{ij}^{(1)}(t_1)\exp(i\omega t_1)dt_1$ is the first-order susceptibility of the material and a second-rank tensor too. In these equations, $\omega_\sigma = \omega$. The broader meaning of ω_σ will become apparent for the nonlinear susceptibilities.

2.2.2. The nonlinear polarization

With the same assumptions as in the previous paragraph (homogeneity, time invariance, locality and causality), the quadratic, cubic and higher order polarizations are expressed as

$$\vec{P}_i^{(2)}(\vec{r};t) = \varepsilon_0 \int_0^t \int_0^t R_{ijk}^{(2)}(\vec{r};t-t_1,t-t_2)\vec{E}_j(\vec{r};t_1).\vec{E}_k(\vec{r};t_2)dt_1 dt_2$$

(A.2.11)

$$\vec{P}_i^{(3)}(\vec{r};t) = \varepsilon_0 \int_0^t \int_0^t \int_0^t R_{ijkl}^{(3)}(\vec{r};t-t_1,t-t_2,t-t_3)\vec{E}_j(\vec{r};t_1).\vec{E}_k(\vec{r};t_2).\vec{E}_l(\vec{r};t_3)dt_1 dt_2 dt_3$$

(A.2.12)

$$\vec{P}_i^{(n)}(\vec{r};t) = \varepsilon_0 \int_0^t \int_0^t \ldots \int_0^t R_{ij\ldots\eta}^{(n)}(\vec{r};t-t_1,t-t_2,\ldots,t-t_n)\vec{E}_j(\vec{r};t_1).\vec{E}_k(\vec{r};t_2)\ldots\vec{E}_\eta(\vec{r};t_n)dt_1dt_2\ldots dt_n$$

(A.2.13)

where $R_{ij\ldots\eta}^{(n)}$ is an $(n+1)$-rank tensor denoted as the n^{th}-order response function of the material.

By expressing the response functions and the electric fields with their respective Fourier transforms, the equations (A.2.11), (A.2.12) and (A.2.13) can be rewritten as

$$\vec{P}_i^{(2)}(\vec{r};t) = \frac{\varepsilon_0}{(2\pi)^2} \int_{-\infty}^{+\infty}\int_{-\infty}^{+\infty} \chi_{ijk}^{(2)}(-\omega_\sigma;\omega_1,\omega_2)\vec{E}_j(\vec{r};\omega_1).\vec{E}_k(\vec{r};\omega_2) \times \exp[-i(\omega_1+\omega_2)t]d\omega_1 d\omega_2$$

(A.2.14)

$$\vec{P}_i^{(3)}(\vec{r};t) = \frac{\varepsilon_0}{(2\pi)^3} \int_{-\infty}^{+\infty}\int_{-\infty}^{+\infty}\int_{-\infty}^{+\infty} \chi_{ijkl}^{(3)}(-\omega_\sigma;\omega_1,\omega_2,\omega_3)\vec{E}_j(\vec{r};\omega_1).\vec{E}_k(\vec{r};\omega_2).\vec{E}_l(\vec{r};\omega_3) \times \exp[-i(\omega_1+\omega_2+\omega_3)t]d\omega_1 d\omega_2 d\omega_3$$

(A.2.15)

$$\vec{P}_i^{(n)}(\vec{r};t) = \frac{\varepsilon_0}{(2\pi)^n} \int_{-\infty}^{+\infty}\int_{-\infty}^{+\infty}\ldots\int_{-\infty}^{+\infty} \chi_{ij\ldots\eta}^{(n)}(-\omega_\sigma;\omega_1,\omega_2,\ldots,\omega_n)\vec{E}_j(\vec{r};\omega_1).\vec{E}_k(\vec{r};\omega_2)\ldots\vec{E}_\eta(\vec{r};\omega_n) \times \exp[-i(\omega_1+\omega_2+\ldots+\omega_n)t]d\omega_1 d\omega_2\ldots d\omega_n$$

(A.2.16)

where $\chi^{(n)}$ is the n^{th}-order susceptibility defined as the Fourier transform of the response function of the material

$$\chi_{ijk}^{(2)}(-\omega_\sigma;\omega_1,\omega_2) = \int_{-\infty}^{+\infty} R_{ijk}^{(2)}(t_1,t_2)\exp[i(\omega_1 t_1+\omega_2 t_2)]dt_1 dt_2$$

(A.2.17)

$$\chi_{ijkl}^{(3)}(-\omega_\sigma;\omega_1,\omega_2,\omega_3) = \int_{-\infty}^{+\infty} R_{ijkl}^{(3)}(t_1,t_2,t_3)\exp[i(\omega_1 t_1+\omega_2 t_2+\omega_3 t_3)]dt_1 dt_2 dt_3$$

(A.2.18)

$$\chi_{ij\ldots\eta}^{(n)}(-\omega_\sigma;\omega_1,\omega_2,\ldots,\omega_n) = \int_{-\infty}^{+\infty} R_{ij\ldots\eta}^{(n)}(t_1,t_2,\ldots,t_n)\exp[i(\omega_1 t_1+\omega_2 t_2+\ldots+\omega_n t_n)]dt_1 dt_2\ldots dt_n$$

(A.2.19)

Unlike the linear polarization in the Fourier space, which is a simple product, the quadratic and cubic polarizations are complicated convolution products and they will therefore not be written in this manuscript.

2.3. The properties of the susceptibility

2.3.1. The reality

The electric field, as well as the polarization, are real measurable quantities. Thus, the response function is also real. Therefore, it comes from the Fourier relation between the susceptibility and the response function that the susceptibility is a complex quantity

$$\chi_{ij...\eta}^{(n)}\left(-\omega_\sigma;\omega_1,\omega_2,...,\omega_n\right)=\mathrm{Re}\left\{\chi_{ij...\eta}^{(n)}\left(\omega_\sigma;-\omega_1,-\omega_2,...,-\omega_n\right)\right\}+i\,\mathrm{Im}\left\{\chi_{ij...\eta}^{(n)}\left(\omega_\sigma;-\omega_1,-\omega_2,...,-\omega_n\right)\right\}$$

(A.2.20)

obeying the following relation

$$\chi_{ij...\eta}^{(n)}\left(-\omega_\sigma;\omega_1,\omega_2,...,\omega_n\right)=\chi_{ij...\eta}^{(n)\,*}\left(\omega_\sigma;-\omega_1,-\omega_2,...,-\omega_n\right) \qquad \text{(A.2.21)}$$

where the symbol * denotes the complex conjugate [But90].

2.3.2. The causality

The causality principle states that the effect cannot precede the cause. In the frequency domain, this is expressed mathematically by the Kramers-Krönig relations, which relate the real and imaginary parts of the susceptibility one to another. They are given in their well-known general form for the linear susceptibility by

$$\begin{cases} \mathrm{Re}\left\{\chi_{ij}^{(1)}(\omega)\right\} = -\dfrac{1}{\pi}\wp\displaystyle\int_{-\infty}^{+\infty}\dfrac{\mathrm{Im}\left\{\chi_{ij}^{(1)}(s)\right\}}{\omega - s}ds \\ \mathrm{Im}\left\{\chi_{ij}^{(1)}(\omega)\right\} = \dfrac{1}{\pi}\wp\displaystyle\int_{-\infty}^{+\infty}\dfrac{\mathrm{Re}\left\{\chi_{ij}^{(1)}(s)\right\}}{\omega - s}ds \end{cases} \tag{A.2.22}$$

where $\wp$ denotes the Cauchy principal part of the integral.

The Kramers-Krönig relations can also be applied to the nonlinear susceptibilities as follow

$$\begin{cases} \mathrm{Re}\left\{\chi_{ij\ldots\eta}^{(n)}(\omega_\sigma;-\omega_1,-\omega_2,\ldots,-\omega_m,\ldots,-\omega_n)\right\} = -\dfrac{1}{\pi}\wp\displaystyle\int_{-\infty}^{+\infty}\dfrac{\mathrm{Im}\left\{\chi_{ij\ldots\eta}^{(n)}(\omega_\sigma;-\omega_1,-\omega_2,\ldots,-\omega_n)\right\}}{\omega_m - s}ds \\ \mathrm{Im}\left\{\chi_{ij\ldots\eta}^{(n)}(\omega_\sigma;-\omega_1,-\omega_2,\ldots,-\omega_m,\ldots,-\omega_n)\right\} = \dfrac{1}{\pi}\wp\displaystyle\int_{-\infty}^{+\infty}\dfrac{\mathrm{Re}\left\{\chi_{ij\ldots\eta}^{(n)}(\omega_\sigma;-\omega_1,-\omega_2,\ldots,-\omega_n)\right\}}{\omega_m - s}ds \end{cases}$$

(A.2.23)

More details about the Kramers-Krönig relations in nonlinear optics can be found in [She04].

2.3.3. The intrinsic permutation symmetry

The intrinsic permutation symmetry is a completely rigorous property which arises from the principles of reality and causality, and which applies universally. Here is its statement. The polarization $\vec{P}_i^{(n)}$ is defined uniquely by the equation (A.2.13), but the tensor $R_{ij\ldots\eta}^{(n)}$ is not unique because of the $n!$ possible orders in which the terms $\vec{E}_j(t_1).\vec{E}_k(t_2)...\vec{E}_\eta(t_n)$ may be written. To remove the arbitrariness of this tensor, $R_{ij\ldots\eta}^{(n)}(t-t_1,t-t_2,\ldots,t-t_n)$ must be required to be invariant under all $n!$ permutations of the n pairs $(i;t-t_1)$, $(j;t-t_2)$, …, $(\eta;t-t_n)$. This can be translated mathematically by

$$R_{ij\ldots\eta}^{(n)}(t-t_1,t-t_2,\ldots,t-t_n) = \frac{1}{n!}S\left[R_{ij\ldots\eta}^{(n)}(t-t_1,t-t_2,\ldots,t-t_n)\right] \tag{A.2.24}$$

where S indicates a summation over all the tensors obtained by making the $n!$ permutations of the n pairs $(i;t-t_1)$, $(j;t-t_2)$, …, $(\eta;t-t_n)$ [But90].

2.4. The Maxwell's equations and the constitutive relations

In the following paragraphs of this chapter, the Einstein notation of the implicit summation will not be written, for simplification. All the phenomena in classical electromagnetism are ruled by the four differential Maxwell's equations

$$\begin{cases} \vec{\nabla}.\vec{D}(\vec{r};t) = \rho_V(\vec{r};t) \\ \vec{\nabla}.\vec{B}(\vec{r};t) = 0 \\ \vec{\nabla}\times\vec{E}(\vec{r};t) = -\dfrac{\partial\vec{B}(\vec{r};t)}{\partial t} \\ \vec{\nabla}\times\vec{H}(\vec{r};t) = \dfrac{\partial\vec{D}(\vec{r};t)}{\partial t} + \vec{J}(\vec{r};t) \end{cases} \tag{A.2.25}$$

where $\vec{D}$ is the electric displacement, $\vec{E}$ the electric field, $\vec{B}$ the magnetic induction, $\vec{H}$ the magnetic field, $\vec{J}$ the current density and ρ_V the volume charge density.

The constitutive relations of the material are given by

$$\begin{cases} \vec{D}(\vec{r};t) = \varepsilon_0\vec{E}(\vec{r};t) + \vec{P}(\vec{r};t) \\ \vec{B}(\vec{r};t) = \mu_0\left[\vec{H}(\vec{r};t) + \vec{M}(\vec{r};t)\right] \end{cases} \tag{A.2.26}$$

where ε_0 is the dielectric permittivity of vacuum, $\vec{P}$ the polarization, μ_0 the magnetic permeability of vacuum and $\vec{M}$ the magnetization.

The current density $\vec{J}$ is the sum of the conduction current density $\vec{J}_C$, the magnetism current density $\vec{J}_M$ and the polarization current density $\vec{J}_P$, such that

$$\begin{aligned} \vec{J}(\vec{r};t) &= \vec{J}_C(\vec{r};t) + \vec{J}_M(\vec{r};t) + \vec{J}_P(\vec{r};t) \\ &= \sigma\vec{E}(\vec{r};t) + \vec{\nabla}\times\vec{M}(\vec{r};t) + \frac{\partial\vec{P}(\vec{r};t)}{\partial t} \end{aligned} \tag{A.2.27}$$

where σ is the conductivity.

2.5. The propagation equation

Throughout this manuscript, isotropic dielectric materials will be examined, which are non-magnetic ($\vec{M} = \vec{0}$). Moreover, it will be assumed that the materials are charge free ($\rho_V = 0$) and current free ($\vec{J} = \vec{0}$). With these assumptions and by combining the Maxwell's equations with the constitutive relations, one can obtain the following wave propagation equation in the time domain

$$\nabla^2 \vec{E}(\vec{r};t) - \frac{1}{c^2}\frac{\partial^2 \vec{E}(\vec{r};t)}{\partial t^2} = \mu_0 \frac{\partial^2 \vec{P}(\vec{r};t)}{\partial t^2} \tag{A.2.28}$$

where c is the speed of light in vacuum.

Depending on the considered problem, one may choose to work in the time domain with the equation (A.2.28), or in the frequency domain with the following equation, obtained by expressing $\vec{E}$ and $\vec{P}$ in terms of their Fourier transforms

$$\nabla^2 \vec{E}(\vec{r};\omega) - \frac{\omega^2}{c^2}\vec{E}(\vec{r};\omega) = \mu_0 \omega^2 \vec{P}(\vec{r};\omega) \tag{A.2.29}$$

These wave equations are second-order differential equations with the polarization acting as a source term. For a linear response, a particular solution to these equations is the plane wave. For a nonlinear response, these equations have no solution. Nevertheless, by using the slowly-varying envelope approximation, these equations can be solved in particular cases.

2.5.1. The nonlinear propagation equation

The polarization is the sum of two components, one linear and one nonlinear with the electric field. Assuming an instantaneous response ($R^{(1)}(t) = \sigma^{(1)}\delta(t)$, where δ is the Dirac delta function), the polarization is given as

$$\vec{P}(\vec{r};t)=\vec{P}_L(\vec{r};t)+\vec{P}_{NL}(\vec{r};t)=\varepsilon_0\sigma^{(1)}\vec{E}(\vec{r};t)+\vec{P}_{NL}(\vec{r};t) \tag{A.2.30}$$

By substituting the above expression of the polarization in the wave propagation equation (A.2.28), one can find the nonlinear propagation equation

$$\nabla^2\vec{E}(\vec{r};t)-\frac{1+\sigma^{(1)}}{c^2}\frac{\partial^2\vec{E}(\vec{r};t)}{\partial t^2}=\mu_0\frac{\partial^2\vec{P}_{NL}(\vec{r};t)}{\partial t^2} \tag{A.2.31}$$

2.5.2. The paraxial propagation equation

By decomposing the Laplacian operator into two components, one transverse and one longitudinal, as $\nabla^2=\frac{\partial^2}{\partial x^2}+\frac{\partial^2}{\partial y^2}+\frac{\partial^2}{\partial z^2}=\nabla_\perp^2+\frac{\partial^2}{\partial z^2}$, the nonlinear propagation equation becomes

$$\nabla_\perp^2\vec{E}(\vec{r};t)+\frac{\partial^2\vec{E}(\vec{r};t)}{\partial z^2}-\frac{1+\sigma^{(1)}}{c^2}\frac{\partial^2\vec{E}(\vec{r};t)}{\partial t^2}=\mu_0\frac{\partial^2\vec{P}_{NL}(\vec{r};t)}{\partial t^2} \tag{A.2.32}$$

Let us assume a monochromatic plane wave propagating in the direction of increasing z (direct wave) is a solution of the nonlinear wave equation (A.2.28). The electric field and the polarization are written as

$$\vec{E}(\vec{r}\,;t)=\frac{1}{2}\left\{\vec{A}(\vec{r}\,;t)\exp\left[i(kz-\omega t)\right]+\vec{A}^*(\vec{r}\,;t)\exp\left[-i(kz-\omega t)\right]\right\} \tag{A.2.33}$$

$$\vec{P}_{NL}(\vec{r}\,;t)=\frac{1}{2}\left\{\vec{p}_{NL}(\vec{r}\,;t)\exp\left[i(k'z-\omega t)\right]+\vec{p}^{\,*}_{NL}(\vec{r}\,;t)\exp\left[-i(k'z-\omega t)\right]\right\} \tag{A.2.34}$$

where $\vec{A}$ and $\vec{p}_{NL}$ are the electric field and nonlinear polarization magnitudes and k and k' the wave vectors associated to the electric field and the nonlinear polarization, respectively.

By substituting the electric field and the nonlinear polarization expressions and their derivative in equation (A.2.32), one can get

$$\nabla_{\perp}^{2}\vec{A}(\vec{r};t)+\frac{\partial^{2}\vec{A}(\vec{r};t)}{\partial z^{2}}+2ik\frac{\partial\vec{A}(\vec{r};t)}{\partial z}-\frac{1+\sigma^{(1)}}{c^{2}}\frac{\partial^{2}\vec{A}(\vec{r};t)}{\partial t^{2}}+2ik\frac{1+\sigma^{(1)}}{c}\frac{\partial\vec{A}(\vec{r};t)}{\partial t}$$
$$=\left[\mu_{0}\frac{\partial^{2}\vec{p}_{NL}(\vec{r};t)}{\partial t^{2}}-2\mu_{0}i\omega\frac{\partial\vec{p}_{NL}(\vec{r};t)}{\partial t}-\mu_{0}\omega^{2}\vec{p}_{NL}(\vec{r};t)\right]\exp(i\Delta kz)$$

(A.2.35)

where $\Delta k=k'-k$ is the phase mismatch.

The slowly-varying envelope approximation assumes that the magnitudes of the electric field and the polarization vary slowly on a spatial period (or wavelength) and a temporal period. This is translated mathematically by the following inequalities

$$\begin{cases}\left|\frac{\partial^{2}\vec{A}}{\partial z^{2}}\right|<<\left|k\frac{\partial\vec{A}}{\partial z}\right|<<k^{2}\vec{A}\\ \left|\frac{\partial^{2}\vec{A}}{\partial t^{2}}\right|<<\left|\omega\frac{\partial\vec{A}}{\partial t}\right|<<\omega^{2}\vec{A}\\ \left|\frac{\partial^{2}\vec{p}_{NL}}{\partial t^{2}}\right|<<\left|\omega\frac{\partial\vec{p}_{NL}}{\partial t}\right|<<\omega^{2}\vec{p}_{NL}\end{cases}\qquad\text{(A.2.36)}$$

Finally, here comes the paraxial propagation equation

$$\nabla_{\perp}^{2}\vec{A}(\vec{r};t)+2ik\left[\frac{\partial\vec{A}(\vec{r};t)}{\partial z}+\frac{1+\sigma^{(1)}}{c}\frac{\partial\vec{A}(\vec{r};t)}{\partial t}\right]=-\mu_{0}\omega^{2}\vec{p}_{NL}(\vec{r};t)\exp(i\Delta kz)\qquad\text{(A.2.37)}$$

$\nabla_{\perp}^{2}\vec{A}(\vec{r};t)$ is the diffraction term, $2ik\left[\frac{\partial\vec{A}(\vec{r};t)}{\partial z}+\frac{1+\sigma^{(1)}}{c}\frac{\partial\vec{A}(\vec{r};t)}{\partial t}\right]$ the propagation term and $-\mu_{0}\omega^{2}\vec{p}_{NL}(\vec{r};t)\exp(i\Delta kz)$ the source term. The paraxial propagation equation will be applied later in the manuscript to two particular nonlinear effects: Third-Harmonic Generation (THG) and Optical Kerr Effect (OKE).

CHAPTER THREE: ORIGIN OF THE DIFFERENT CONTRIBUTIONS TO THE NONLINEAR RESPONSE

The magnitude of the nonlinear response of a material depends on the physical involved processes. These effects have different origins, namely, electronic polarization, nuclear response, electrostriction and thermal response. The third-order susceptibility can therefore be decomposed in a sum of terms corresponding to each contribution

$$\chi^{(3)} = \chi^{(3)}_{elec} + \chi^{(3)}_{nuc} + \chi^{(3)}_{str} + \chi^{(3)}_{th} \qquad \text{(A.3.1)}$$

Depending on the duration of the pulse and/or the repetition rate of the laser, these phenomena contribute more or less to the nonlinear response. They are described in this chapter and their magnitude is discussed in the femtosecond regime with MHz laser systems. The electronic and nuclear responses are not discussed at length in this chapter because they will be described in detail in the subsequent chapters.

3.1. The electronic response

Except near a resonance, the electronic response is quasi-instantaneous, less than one femtosecond. It is due to the spontaneous nonlinear distortion of the electronic distribution around the nuclei and it is independent of the temperature.

Far from any resonance, this process involves an important relation between the different components of the third-order susceptibility tensor for isotropic materials [But90]

$$\chi^{(3)}_{xxxx} = 3\chi^{(3)}_{xxyy} = 3\chi^{(3)}_{xyxy} = 3\chi^{(3)}_{xyyx} \qquad \text{(A.3.2)}$$

Thus, all the components of the $\chi^{(3)}$ tensor can be defined from the knowledge of only one of them.

Whatever the duration of the pulse and the repetition rate of the laser, the electronic response is always present. The magnitude of the electronic contribution for fused silica is on the order of $\chi^{(3)}_{elec} \approx 10^{-22}\ \mathrm{m}^2.\mathrm{V}^{-2}$.

3.2. The nuclear response

The nuclear response corresponds to the rearrangement of the position of the nuclei in the new potential created by the electric field of the electrons. These motions are much slower than the electronic ones and depend on the temperature. There are different types of nuclear response: molecular reorientation, molecular redistribution, vibrations and librations.

- Molecular reorientation comes from the alignment of the molecules having acquired or possessing naturally a dipolar moment in the direction of the exciting electric field. This process is therefore important in polar molecules.
- Molecular redistribution is particularly present in dense polarizable media. The application of an intense electric field produces interactions between the created dipoles and leads to a redistribution of the molecules which acquire a new equilibrium state by minimization of the energy.
- Vibrations are collective motions of molecules, in same or opposite directions.
- Librations are vibrations based on a rotational motion of the molecules on sites that prevent overall rotation. They are more descriptively called “rotational vibrations”.

The response time of the nuclear processes is on the order of several hundreds of femtoseconds to a few picoseconds. With a laser presenting a repetition rate in the MHz regime, there is no accumulation pulse after pulse of the nuclear effect. Moreover, if the laser pulse is short enough (less than 50 fs), this process is negligible. The magnitude of the Raman contribution for fused silica is on the order of $\chi^{(3)}_{nuc} \approx 10^{-23}\ \mathrm{m}^2.\mathrm{V}^{-2}$.

3.3. The electrostrictive response

Electrostriction is the process in which the material density increases in response to an applied electric field. The electric field polarizes the molecules which lead to an inter-molecular attraction and therefore to a compression of the material. The local increase of the pressure induces an increase of the nonlinear response.

The presence of an electric field within a material produces a pressure given by [Boy99]

$$P_{str} = \frac{\gamma_{str}}{4 n_0 c} I \tag{A.3.3}$$

where n_0 is the non-disrupted refractive index, c the speed of light in the vacuum and $I(\vec{r};t)$ the irradiance. $\gamma_{str} = \rho_0 \left(\frac{\partial \varepsilon_r}{\partial \rho} \right)_{\rho=\rho_0}$ is known as the electrostrictive constant, with ρ_0 the non-disrupted density and ε_r the relative dielectric permittivity. This parameter can be evaluated with the Lorentz-Lorenz formula

$$\gamma_{str} = \frac{(\varepsilon_{r0} - 1)(\varepsilon_{r0} + 2)}{3} \tag{A.3.4}$$

where ε_{r0} is the non-disrupted relative dielectric permittivity.

In the case of solid, which is both isotropic and elastic, the spatial and temporal density variation $\Delta\rho(\vec{r};t)$ in the material can be described by the acoustic differential equation

$$\nabla^2 \Delta\rho - \frac{1}{v_s^2} \frac{\partial^2 \Delta\rho}{\partial t^2} + \frac{\Gamma'}{v_s^2} \nabla^2 \left(\frac{\partial \Delta\rho}{\partial t} \right) = \frac{\gamma_{str}}{2 n_0 c v_s^2} \nabla^2 I \tag{A.3.5}$$

where v_s is the sound velocity in the material and Γ' is a damping factor (which can be neglected for most optical materials).

For a Gaussian beam with a beam waist w_0, the change in the density will be established in a time τ_ρ on the order of [Oli04]

$$\tau_\rho \approx \frac{w_0}{v_s} \tag{A.3.6}$$

In fused silica, $v_s \approx 5970\,\text{m.s}^{-1}$. For a beam waist of $w_0 = 10\,\mu\text{m}$, the corresponding characteristic time is $\tau_\rho \approx 2\,\text{ns}$.

The maximal density variation on the optical axis is given by the source term of the acoustic differential equation [Oli04]

$$\Delta\rho_{\max} = \frac{\gamma_{str} I_0}{2 n_0 c v_s^2} \tag{A.3.7}$$

For fused silica, $\varepsilon_{r0} \approx 2.1$, $\gamma_{str} = \frac{(\varepsilon_{r0}-1)(\varepsilon_{r0}+2)}{3} \approx 1.5$, $n_0 \approx 1.46$, $v_s \approx 5970\,\text{m.s}^{-1}$ and a peak irradiance of $I_0 \approx 2.4\times10^{16}\ \text{W.m}^{-2}$, then $\Delta\rho_{\max} \approx 1.2\,\text{kg.m}^{-3}$.

This density variation corresponds to a third-order susceptibility variation of

$$\chi_{str}^{(3)} = \frac{\varepsilon_0 \gamma_{str}^2}{3\rho_0 v_s^2} \tag{A.3.8}$$

With $\rho_0 \approx 2200\,\text{kg.m}^{-3}$ for fused silica, the electrostrictive contribution can be as high as $\chi_{str}^{(3)} \approx 10^{-22}\ \text{m}^2.\text{V}^{-2}$.

The electrostrictive effect has a response time of approximately a tens of nanoseconds, the typical transit time of an acoustic wave. With MHz systems, there is no cumulative effect for this process. In the femtosecond regime, electrostriction cannot occur because the rise time is too long compared to the pulse duration.

Buckland and Boyd have plotted the evolution of the electrostrictive contribution to the fast nonresonant electronic response as a function of the pulse width for a fused silica fiber [Buc96]. They found that the electrostrictive contribution is maximal for pulses longer

than 1 ns and it is as high as 16% of the total nonlinearity (*cf.* figure 1). For pulses shorter than 10 ps, this contribution is null.

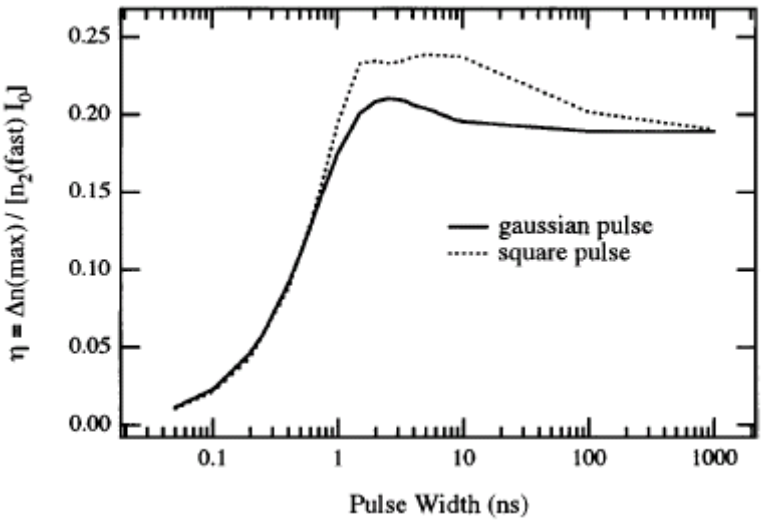

Figure 1: Evolution of the electrostrictive contribution relative to the fast non-resonant electronic response versus the pulse width (FWHM) [Buc96].

3.4. The thermal response

The thermal response is due to the absorption of the electric field by the material, which is then dissipated in the form of heat. This warming induces a change in the nonlinear properties. The response time of thermal effects is on the order of a ten of microseconds.

The spatial and temporal repartition of the temperature $T(\vec{r};t)$ in the material obeys to the differential equation of the heat with a source term coming from the conversion into heat of part of the power of the pulse

$$\rho_0 C_p \frac{\partial T}{\partial t} - \kappa \nabla^2 T = \alpha I \qquad \text{(A.3.9)}$$

where ρ_0 is the density of the medium, C_p the heat capacity at constant pressure, κ the thermal conductivity, α the absorption coefficient and $I(\vec{r};t)$ the irradiance. The term $\kappa\nabla^2 T$ represents the thermal diffusion. The source term αI represents the fraction of power of the beam converted into heat by unit of volume.

The relaxation time of thermal diffusion is determined by the thermal diffusivity $D = \kappa / \rho_0 C_p$. For a Gaussian beam with a beam waist w_0, the heat will evacuate the point of focus by diffusion in a time τ_D on the order of [Oli04]

$$\tau_D \approx \frac{w_0^2}{4D} \tag{A.3.10}$$

In the case of fused silica, the thermal diffusivity is $D \approx 0.85 \times 10^{-6}\ \mathrm{m}^2.\mathrm{s}^{-1}$. For a beam waist of $w_0 = 10\,\mu\mathrm{m}$, the corresponding diffusion time is $\tau_D \approx 30\,\mu\mathrm{s}$. Thus, with a MHz laser system, there is accumulation pulse after pulse of the thermal effect.

For a pulse of 100 fs, the thermal diffusion has no influence on the beam itself. Therefore, the term $\kappa \nabla^2 T$ in the differential equation of the heat can be neglected. This equation can therefore be integrated to supply the temporal evolution of the increase of temperature on the optical axis at the point of focus [Oli04]

$$\Delta T(t) = T(t) - T(-\infty) = \frac{\alpha}{\rho_0 C_p} \int_{-\infty}^{t} I(\vec{0}; \tau) d\tau \tag{A.3.11}$$

The variation of the third-order susceptibility associated with the thermal effect can be written as

$$\chi_{th}^{(3)} = \frac{4\varepsilon_0 n_0^2 c}{3 I_0} \frac{\partial n}{\partial T} \Delta T = \frac{\partial \chi^{(3)}}{\partial T} \Delta T \tag{A.3.12}$$

where $\partial n / \partial T$ is the thermo-optical coefficient and I_0 the peak irradiance.

To estimate the magnitude of the thermal contribution, the following features for fused silica have been assumed: $\alpha \approx 10^{-2}\ \mathrm{m}^{-1}$, $\rho_0 \approx 2200\ \mathrm{kg.m}^{-3}$, $C_p \approx 703\ \mathrm{J.kg}^{-1}.\mathrm{K}^{-1}$, $n_0 \approx 1.46$ and $\frac{\partial n}{\partial T} = 10^{-5}\ \mathrm{K}^{-1}$. The evolution of the thermal contribution is plotted in figure 2 for a Gaussian pulse with a half-width at $1/e$ of $\tau_p = 120\,\mathrm{fs}$ and a peak irradiance of $I_0 \approx 2.4 \times 10^{16}\ \mathrm{W.m}^{-2}$.

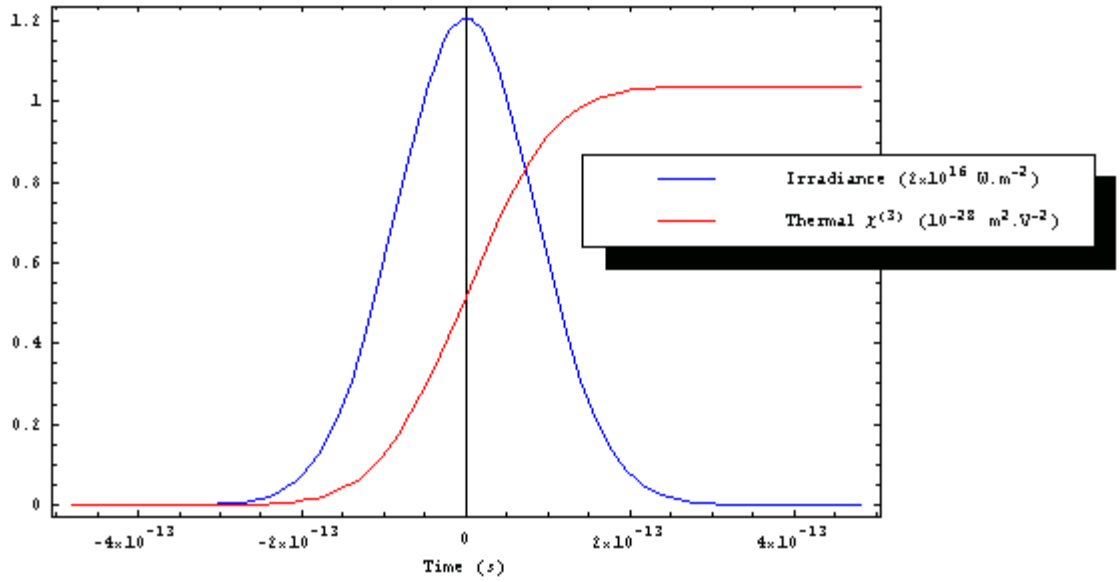

Figure 2: Evolution of the irradiance (blue curve) and of the thermal contribution (red curve) versus time.

From figure 2, one can see that the maximal magnitude of the thermal contribution is on the order of $\chi_{th}^{(3)} \approx 10^{-28}\ \mathrm{m}^2.\mathrm{V}^{-2}$, well below the other contributions. Thus, this contribution can be neglected in the femtosecond regime, *when only one pulse is considered*. However, *if many pulses are involved*, typically more than one million, a cumulative effect pulse after pulse can give rise to a non-negligible thermal contribution if the characteristic diffusion time of the heat is longer than the period of repetition of the laser. This is typically true for MHz systems but not for kHz systems.

3.5. Summary

The laser systems considered in the part A of this manuscript deliver pulses of about 100 fs in the visible/near infrared region with an 80 MHz repetition rate, *i.e.* a period of 12.5 ns. The physical processes with a response time higher than 12.5 ns will experience a cumulative effect. The only effect which satisfies this condition is the thermal one. Nevertheless, it has a negligible magnitude in the femtosecond regime if only one pulse is

considered. Table 1 recapitulates different features of the physical processes involved in the nonlinear response.

Process	**Response time**	**Cumulative effect**	**Magnitude ($m^2.V^{-2}$)**	**Negligible in the femtosecond regime**
Electronic	1 fs	No	10^{-22}	No
Nuclear	100 fs	No	10^{-23}	No
Electrostrictive	1 ns	No	10^{-22}	Yes
Thermal	10 µs	No in the kHz regime Yes in the MHz regime	10^{-28}	Yes in the kHz regime No in the MHz regime

Table 1: Recapitulation of the different processes involved in the nonlinear response of a material. Typical values for fused silica have been assumed.

CHAPTER FOUR: THE BORN-OPPENHEIMER APPROXIMATION IN NONLINEAR OPTICS

This chapter is based on Hellwarth's reference paper discussing third-order nonlinear optics [Hel77]. This article deals with the application of the Born-Oppenheimer approximation in order to dissociate, thanks to their different response times, the electronic and nuclear contributions to the third-order nonlinear optical properties. For a modern understanding, this chapter is written in SI units rather than in CGS, like in Hellwarth's paper.

4.1. Outline of the approximation method

The Born-Oppenheimer approximation is valid only when all the electromagnetic frequencies involved are much lower than the electronic resonances and much higher than the vibrational ones. In this particular case, the motions of the nuclei and the electrons can be treated separately. The action of the electric field on the medium is decomposed into two processes:

- The electronic processes, which appear when the nuclei position are frozen. They are due to the instantaneous distortion at the scale of the optical cycle (~ 1 fs) of the electronic cloud and they are temperature independent.
- The nuclear processes, which correspond to the rearrangements of the nuclei position in the new potential created by the electric field of the electrons. These motions are much slower and they are temperature dependent.

4.2. The electronic energy

Let us consider a system with N particles (electrons and nuclei of several species) in a cubic volume $V = L^3$, the operator electric dipole moment is given by

$$\vec{D}_i = \sum_{\alpha=1}^{N} e_\alpha \vec{x}_{i\alpha} \tag{A.4.1}$$

where e_α is the electric charge of the particle α, $\vec{x}_{i\alpha}$ the position coordinate of the particle α, $i = x, y, z$ and $\alpha = 1,2,...,N$.

Within the context of the electric dipole approximation (the variations of the electric field in a region which dimension is lower than the wavelength can be neglected), the Hamiltonian of the system is written as

$$H(t) = H_0 + H_E(t) \tag{A.4.2}$$

where

$$H_0 = H_{0\_e} + H_{0\_n} + H_{0\_e-n} \tag{A.4.3}$$

is the non-disrupted Hamiltonian ($\vec{E} = \vec{0}$) of the system (sum of the electronic H_{0_e}, the nuclear H_{0_n} and the electronic-nuclear interaction H_{0_e-n} non-disrupted Hamiltonians) and

$$H_E(\vec{r};t) = -\vec{D}_i.\vec{E}_i(\vec{r};t) \tag{A.4.4}$$

is the Hamiltonian of interaction between the electric field and the particles.

Within the context of the *Born-Oppenheimer approximation*, the Hamiltonian of interaction between the electric field and the particles H_E can be decomposed into a Hamiltonian of interaction between the electric field and the electrons H_{E-e} and another one between the electric field and the nuclei H_{E-n}

$$H_E = H_{E-e} + H_{E-n} \tag{A.4.5}$$

with

$$H_{E-e} = -e \sum_{electrons} \vec{r}_{i\alpha}.\vec{E}_i \tag{A.4.6}$$

and

$$H_{E-n} = e \sum_{nuclei} Z_\alpha \vec{R}_{i\alpha}.\vec{E}_i \tag{A.4.7}$$

where e is the electric charge of the electron, $\vec{r}_{i\alpha}$ and $\vec{R}_{i\alpha}$ the positions of the electron and the nucleus α, respectively, and Z_α the atomic number of the nucleus α.

As the perturbation H_{E-e} varies linearly with the electric field, the theory of the time-independent perturbations (Rayleigh-Schrödinger theory) can be applied and the energy of the fundamental electronic state be developed in a series of ascending power of the electric field

$$\begin{aligned} &W_0\left(\vec{R}_{i\alpha};\vec{E}_i\right) \\ &= W_{00} - \left[\vec{\mu}_i\left(\vec{R}_{i\alpha}\right).\vec{E}_i + \frac{1}{2}\alpha_{ij}\left(\vec{R}_{i\alpha}\right)\vec{E}_i.\vec{E}_j + \frac{1}{3}\vec{\beta}_{ijk}\left(\vec{R}_{i\alpha}\right).\vec{E}_i.\vec{E}_j.\vec{E}_k + \frac{1}{6}\gamma_{ijkl}\left(\vec{R}_{i\alpha}\right)\vec{E}_i.\vec{E}_j.\vec{E}_k.\vec{E}_l + ... \right] V \end{aligned}$$

(A.4.8)

where W_{00} is the kinetic energy, $\vec{\mu}$ the dipole moment, α the polarizability, $\vec{\beta}$ the first-order hyperpolarizability and γ the second-order hyperpolarizability of the electrons.

Within the context of the Born-Oppenheimer approximation, the electrons can be eliminated from the general perturbation calculus, assuming they are always in the fundamental state, independently of the nuclear configuration and of the strength of the external electric field. In the non-disrupted system, their presence is manifested as an effective potential for the nuclear motion. Thus, the global Hamiltonian of the system is written as

$$H_{BO} = H_{0\_n} + H_{\text{int}} \tag{A.4.9}$$

with

$$H_{0\_n} = W_{00} + T_N + \frac{1}{4\pi\varepsilon_0} \sum_{\alpha,\beta} \frac{e_\alpha e_\beta}{\left\| \vec{R}_\alpha - \vec{R}_\beta \right\|} \tag{A.4.10}$$

which is the non-disrupted effective Hamiltonian of the nuclei (kinetic energy of the electrons + kinetic energy of the nuclei + Coulomb interaction between the nuclei) and

$$H_{\text{int}} = \left[-\vec{m}_i.\vec{E}_i - \frac{1}{2}\alpha_{ij}\vec{E}_i.\vec{E}_j - \frac{1}{3}\vec{\beta}_{ijk}.\vec{E}_i.\vec{E}_j.\vec{E}_k - \frac{1}{6}\gamma_{ijkl}\vec{E}_i.\vec{E}_j.\vec{E}_k.\vec{E}_l + \ldots \right] V \\ = H_{\text{int}}^{(0)} + H_{\text{int}}^{(1)} + H_{\text{int}}^{(2)} + H_{\text{int}}^{(3)} + \ldots \tag{A.4.11}$$

which is the Hamiltonian of interaction with the electric field where

$$\vec{m}_i = \frac{e}{V}\sum_{nuclei} Z_\alpha \vec{R}_{i\alpha} + \vec{\mu}_i\left(\vec{R}_{i\alpha}\right) \tag{A.4.12}$$

is the permanent dipole moment of the medium.

4.3. The effective polarization operator

For a given configuration $\left\{\vec{R}_{i\alpha};\vec{E}_i\right\}$ of the nuclei and the electric field, the electrons will occupy a fundamental state $\left|0;\left\{\vec{R}_{i\alpha};\vec{E}_i\right\}\right\rangle$ in which they have an electric dipole moment $\vec{M}_i^{elec}$ given by

$$\vec{M}_i^{elec} = \left\langle 0;\left\{\vec{R}_{i\alpha};\vec{E}_i\right\}\right| - e\sum_{electrons}\vec{r}_{i\alpha}\left|0;\left\{\vec{R}_{i\alpha};\vec{E}_i\right\}\right\rangle \tag{A.4.13}$$

The electric dipole moment can also be expressed in function of the energy of the fundamental state

$$\vec{M}_i^{elec} = -\frac{\partial W_0}{\partial \vec{E}_i} \tag{A.4.14}$$

The total dipole moment is the sum of the electronic dipole moment $\vec{M}_i^{elec}$ and the permanent dipole moment of the nuclei $e\sum_{nuclei} Z_\alpha \vec{R}_{i\alpha}$

$$\vec{p}_i = \frac{1}{V}\left[e\sum_{nuclei} Z_\alpha \vec{R}_{i\alpha} - \frac{\partial W_0}{\partial \vec{E}_i} \right] \tag{A.4.15}$$

$$\Leftrightarrow \begin{aligned} \vec{p}_i &= \vec{m}_i + \alpha_{ij}\vec{E}_j + \vec{\beta}_{ijk}.\vec{E}_j.\vec{E}_k + \gamma_{ijkl}\vec{E}_j.\vec{E}_k.\vec{E}_l + \ldots \\ &= \vec{p}_i^{(0)} + \vec{p}_i^{(1)} + \vec{p}_i^{(2)} + \vec{p}_i^{(3)} + \ldots \end{aligned} \qquad \text{(A.4.16)}$$

4.4. The total expected polarization

The total polarization at the instant t in a small volume centered at the position $\vec{r}$ is the ensemble average of the total dipole moment

$$\vec{P}_i(\vec{r};t) = \left\langle U^{-1}(t)\vec{p}_i(t)U(t)\right\rangle \qquad \text{(A.4.17)}$$

where $U(t)$ is the unitary time-evolution operator which satisfies the equation

$$i\hbar\frac{dU(t)}{dt} = H_{BO}(t)U(t) \qquad \text{(A.4.18)}$$

with the initial condition $U(t=0)=1$ (the electric field is applied at the time $t=0$). $\hbar = \dfrac{h}{2\pi}$ is the Planck constant.

The expansion of the operators $U(t)$ and $U^{-1}(t)$ in the Heisenberg representation gives

$$\begin{aligned} U^{-1}(t)\vec{p}_i(t)U(t) &= \tilde{\vec{p}}_i(t) + (i\hbar)^{-1}\int_{-\infty}^{t} ds\left[\tilde{\vec{p}}_i(t);\tilde{H}_{\text{int}}(s)\right] + (i\hbar)^{-2}\int_{-\infty}^{t} ds\int_{-\infty}^{s} du\left[\left[\tilde{\vec{p}}_i(t);\tilde{H}_{\text{int}}(s)\right];\tilde{H}_{\text{int}}(u)\right] \\ &\quad + (i\hbar)^{-3}\int_{-\infty}^{t} ds\int_{-\infty}^{s} du\int_{-\infty}^{u} dv\left[\left[\left[\tilde{\vec{p}}_i(t);\tilde{H}_{\text{int}}(s)\right];\tilde{H}_{\text{int}}(u)\right];\tilde{H}_{\text{int}}(v)\right] + \ldots \\ &= \vec{\Pi}_i^{(0)} + \vec{\Pi}_i^{(1)} + \vec{\Pi}_i^{(2)} + \vec{\Pi}_i^{(3)} + \ldots \end{aligned}$$

(A.4.19)

where $\left[O_i;O_j^{'}\right] = O_iO_j^{'} - O_j^{'}O_i$ indicates the "commutator" between the arbitrary operators O_i and $O_j^{'}$ and the tilde over an operator means that the parameters must be taken in their unperturbed (without any applied electric field) Heisenberg representation at the given time, that is

$$\tilde{O}_i(t) = U_0^{-1}(t)O_iU_0(t) \qquad \text{(A.4.20)}$$

The n-order polarization is therefore written as

$$\vec{P}_i^{(n)}(\vec{r};t) = \left\langle \vec{\Pi}_i^{(n)} \right\rangle \tag{A.4.21}$$

For each order of the polarization, one has to insert the equations (A.4.16) for $\vec{p}_i$ and (A.4.11) for H_{int} in the equation (A.4.19) and group together the terms of the same order in the macroscopic electric field $\vec{E}_i^n$. The first and the second orders will not be discussed here because we are mainly interested in constructing the third-order polarization $\vec{P}_i^{(3)}$.

4.5. The third-order polarization

At the third order, the polarization is the sum of eight terms corresponding to the power 3 of the electric field. These terms are expressed below and their contributions to the third-order polarization are discussed. The tildes in this section have been omitted for simplicity from the time-dependent operators which are nonetheless assumed to be in their Heisenberg representations.

The first term contains the essentially instantaneous purely electronic contribution

$$\varepsilon_0 \left\langle \gamma_{ijkl} \right\rangle \vec{E}_j(t).\vec{E}_k(t).\vec{E}_l(t) \tag{A.4.22.a}$$

It exists for all the material symmetries and can contribute to all the third-order nonlinear effects.

The second term contains the following three contributions

$$\varepsilon_0 V(i\hbar)^{-1} \int_{-\infty}^{t} ds \left\langle \left[\vec{m}_i(t); \frac{1}{3}\vec{\beta}_{jkl}(s) \right] \right\rangle \vec{E}_j(s).\vec{E}_k(s).\vec{E}_l(s) \tag{A.4.22.b}$$

$$\varepsilon_0 V(i\hbar)^{-1} \vec{E}_j(t) \int_{-\infty}^{t} ds \left\langle \left[\alpha_{ij}(t); \frac{1}{2}\alpha_{kl}(s) \right] \right\rangle \vec{E}_k(s).\vec{E}_l(s) \tag{A.4.22.c}$$

$$\varepsilon_0 V(i\hbar)^{-1} \vec{E}_j(t).\vec{E}_k(t) \int_{-\infty}^{t} ds \left\langle \left[\vec{\beta}_{ijk}(t); \vec{m}_l(s) \right] \right\rangle \vec{E}_l(s) \tag{A.4.22.d}$$

The third term contains the following three contributions

$$\varepsilon_0 V^2 (i\hbar)^{-2} \int_{-\infty}^{t} ds \vec{E}_j(s) \int_{-\infty}^{s} du \left\langle \left[\left[\vec{m}_i(t); \vec{m}_j(s) \right]; \frac{1}{2} \alpha_{kl}(u) \right] \right\rangle \vec{E}_k(u) . \vec{E}_l(u) \qquad \text{(A.4.22.e)}$$

$$\varepsilon_0 V^2 (i\hbar)^{-2} \int_{-\infty}^{t} ds \vec{E}_j(s) . \vec{E}_k(s) \int_{-\infty}^{s} du \left\langle \left[\left[\vec{m}_i(t); \frac{1}{2} \alpha_{jk}(s) \right]; \vec{m}_l(u) \right] \right\rangle \vec{E}_l(u) \qquad \text{(A.4.22.f)}$$

$$\varepsilon_0 V^2 (i\hbar)^{-2} \vec{E}_j(t) \int_{-\infty}^{t} ds \vec{E}_k(s) \int_{-\infty}^{s} du \left\langle \left[\left[\alpha_{ij}(t); \vec{m}_k(s) \right]; \vec{m}_l(u) \right] \right\rangle \vec{E}_l(u) \qquad \text{(A.4.22.g)}$$

The fourth term contains the following contribution

$$\varepsilon_0 V^3 (i\hbar)^{-3} \int_{-\infty}^{t} ds \vec{E}_j(s) \int_{-\infty}^{s} du \vec{E}_k(u) \int_{-\infty}^{u} dv \left\langle \left[\left[\left[\vec{m}_i(t); \vec{m}_j(s) \right]; \vec{m}_k(u) \right]; \vec{m}_l(v) \right] \right\rangle \vec{E}_l(v) \qquad \text{(A.4.22.h)}$$

For each equation (A.4.22), we are now going to discuss the approximations we can make and the terms we can neglect. Using the following representation

$$\left\langle \left[O_i(t); O_j'(s) \right] \right\rangle = \sum_{l,n} w_l \exp\left[i(\omega_l - \omega_n)(t-s) \right] \left\langle l \left| O_i \right| n \right\rangle \left\langle n \left| O_j' \right| l \right\rangle - c.c. \qquad \text{(A.4.23)}$$

in which w_l is the statistical weight of the state $|l\rangle$, the commutators in the equations (A.4.24.b), (A.4.24.c) and (A.4.24.d) are expressed as

$$\left\langle \left[\vec{m}_i(t); \frac{1}{3} \vec{\beta}_{jkl}(s) \right] \right\rangle = \frac{1}{3} \sum_{l,n} w_l \exp\left[i(\omega_l - \omega_n)(t-s) \right] \left\langle l \left| \vec{m}_i(t) \right| n \right\rangle \left\langle n \left| \vec{\beta}_{jkl}(s) \right| l \right\rangle - c.c. \qquad \text{(A.4.24)}$$

$$\left\langle \left[\alpha_{ij}(t); \frac{1}{2} \alpha_{kl}(s) \right] \right\rangle = \frac{1}{2} \sum_{l,n} w_l \exp\left[i(\omega_l - \omega_n)(t-s) \right] \left\langle l \left| \alpha_{ij}(t) \right| n \right\rangle \left\langle n \left| \alpha_{kl}(s) \right| l \right\rangle - c.c. \qquad \text{(A.4.25)}$$

$$\left\langle \left[\vec{\beta}_{ijk}(t); \vec{m}_l(s) \right] \right\rangle = \sum_{l,n} w_l \exp\left[i(\omega_l - \omega_n)(t-s) \right] \left\langle l \left| \vec{\beta}_{ijk}(t) \right| n \right\rangle \left\langle n \left| \vec{m}_l(s) \right| l \right\rangle - c.c. \qquad \text{(A.4.26)}$$

The equations (A.4.24) and (A.4.26) depend only on the time difference $t-s$ and on the product of the permanent dipole moment $\vec{m}$ with the hyperpolarizability of the first-order $\vec{\beta}$. Since the resonance frequencies of $\vec{m}$ for the nuclei are much lower than the resonance frequencies of $\vec{\beta}$ for the electrons, then $\vec{m}$ acts like a low-pass filter for the electric field. Moreover, the third-order nonlinear effects are generally studied at the optical frequencies,

which are well above the frequencies corresponding to the nuclear motions and well below the frequencies corresponding to the electronic ones. Therefore, the equations (A.4.22.b) and (A.4.22.d) do not contribute significantly to the third-order polarization.

Following the same argument, the equations (A.4.22.e) to (A.4.22.h) do not play a role either in the third-order polarization, even though they are responsible of hybrid resonances which translate the coupling between a nuclear level and an electronic level.

Consequently, within the context of the Born-Oppenheimer approximation and for purely optical nonlinear effects, the third-order nonlinear polarization is written as

$$\begin{aligned}\vec{P}_i^{(3)}(t) &= \vec{P}_{elec\_i}^{(3)}(t) + \vec{P}_{nuc\_i}^{(3)}(t) \\ &= \varepsilon_0 \sigma_{ijkl}^{(3)} \vec{E}_j(t).\vec{E}_k(t).\vec{E}_l(t) + \varepsilon_0 \vec{E}_j(t) \int_{-\infty}^{+\infty} d_{ijkl}^{(3)}(t-\tau) \vec{E}_k(\tau).\vec{E}_l(\tau) d\tau\end{aligned} \tag{A.4.27}$$

where $\sigma_{ijkl}^{(3)} \equiv \langle \gamma_{ijkl} \rangle$ is the electronic coefficient defined as the average value of the second-order hyperpolarizability of the electrons and $d_{ijkl}(t) \equiv \frac{iV}{2\hbar} \langle [\alpha_{ij}(t); \alpha_{kl}(0)] \rangle \Theta(t)$ is the nuclear response function depending on the polarizability of the electrons, with $\Theta(t)$ the Heaviside function (or unit step function). The first term is a simple product and it corresponds to the instantaneous electronic nonlinearity; the second term is a convolution product and it translates the non-instantaneous nuclear contribution.

To conclude, the response function of the medium can be decomposed into two components with different response times, one electronic and the other nuclear

$$R_{ijkl}^{(3)}(t) = \sigma_{ijkl}^{(3)} \delta(t) + d_{ijkl}^{(3)}(t) \tag{A.4.28}$$

where δ is the Dirac delta function.

4.6. Symmetry properties of the third-order susceptibility

For isotropic materials, typically glasses, the electronic coefficient and the nuclear response function are expressed as follow

$$\sigma_{ijkl}^{(3)} = \frac{1}{6}\sigma^{(3)}\left(\delta_{ij}\delta_{kl} + \delta_{ik}\delta_{jl} + \delta_{il}\delta_{jk}\right) \tag{A.4.29}$$

$$d_{ijkl}^{(3)}(t) = a(t)\delta_{ij}\delta_{kl} + \frac{1}{2}b(t)\left(\delta_{il}\delta_{jk} + \delta_{ik}\delta_{jl}\right) \tag{A.4.30}$$

where a and b are functions which will be defined later and $\delta_{ij} = \begin{cases} 1 \text{ if } i = j \\ 0 \text{ if } i \neq j \end{cases}$ is the Krönecker delta function.

The nuclear response function in the frequency domain can be obtained by a Fourier transform as follow

$$D_{ijkl}^{(3)}(\omega) = \int_{-\infty}^{+\infty} d_{ijkl}^{(3)}(t)\exp(i\omega t)dt \tag{A.4.31}$$

Equations (A.4.30) and (A.4.31) imply

$$D_{ijkl}^{(3)}(\omega) = A(\omega)\delta_{ij}\delta_{kl} + \frac{1}{2}B(\omega)\left(\delta_{il}\delta_{jk} + \delta_{ik}\delta_{jl}\right) \tag{A.4.32}$$

where $A(\omega) = \int_{-\infty}^{+\infty} a(t)\exp(i\omega t)dt$ and $B(\omega) = \int_{-\infty}^{+\infty} b(t)\exp(i\omega t)dt$.

The third-order dielectric susceptibility is the Fourier transform of the response function of the medium

$$\begin{aligned} \chi_{ijkl}^{(3)}(\omega) &= \int_{-\infty}^{+\infty} R_{ijkl}^{(3)}(t)\exp(i\omega t)dt \\ &= \int_{-\infty}^{+\infty} \sigma_{ijkl}^{(3)}\delta(t)\exp(i\omega t)dt + \int_{-\infty}^{+\infty} d_{ijkl}^{(3)}(t)\exp(i\omega t)dt \\ &= \sigma_{ijkl}^{(3)} + D_{ijkl}^{(3)}(\omega) \end{aligned} \tag{A.4.33}$$

$\chi_{ijkl}^{(3)}$, $\sigma_{ijkl}^{(3)}$ and $D_{ijkl}^{(3)}$ are the total, electronic and nuclear dielectric susceptibilities, respectively, and they are expressed in $m^2.V^{-2}$. Let us notice that the electronic coefficient

$\sigma_{ijkl}^{(3)}$ is independent of the angular frequency because it translates an instantaneous phenomenon.

4.7. Relation between the third-order susceptibility and the spontaneous Raman scattering

There is a well-known formula which relates the stimulated Raman gain g_R to the spectral differential cross-section of spontaneous Raman scattering $\frac{\partial^2\sigma}{\partial\Omega\partial\omega_S}$ [Hel63]. Similarly, the nuclear susceptibility $D_{ijkl}^{(3)}$ can also be related to this latter, but only when the Born-Oppenheimer approximation is valid. The energy diagram of the Stokes Raman process is given in figure 3.

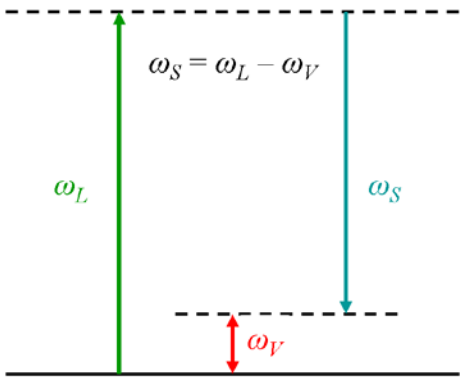

Figure 3: Energy diagram of the Stokes Raman process.

Let us consider the Stokes Raman scattered radiation emitted by an oscillating electric dipole $P_{nuc\_i}^{(3)}$ with orthogonal polarizations $\eta = x, y$. The scattered irradiance I_{S_η} at a point situated at a large distance r (in the far field) and oriented at 90° from the polarization $P_{nuc\_i}^{(3)}$ is

$$I_{S\_\eta} = \frac{V^2}{32\pi^2\varepsilon_0 c^3 r^2}\int_{-\infty}^{+\infty} n_S \omega_S^4 \left\langle \left| P_{nuc\_i}^{(3)}(\omega_S) \right|^2 \right\rangle d\omega_S \tag{A.4.34}$$

where V is the unit cell volume, n_S the refractive index at the Stokes angular frequency ω_S and $\left|P_{nuc\_i}^{(3)}\right|^2$ the power spectrum of the third-order nuclear polarization ($C^2.m^{-4}.s$), such that $\int_{-\infty}^{+\infty}\left\langle \left| P_{nuc\_i}^{(3)}(t) \right|^2 \right\rangle dt = \int_{-\infty}^{+\infty}\left\langle \left| P_{nuc\_i}^{(3)}(\omega) \right|^2 \right\rangle d\omega$. The brackets $\langle\ \rangle$ denote the average on the quantum and thermal fluctuations.

The scattering cross-section σ_η, defined as the scattered photons flux per unit volume divided by the laser photons flux per unit area, is expressed as

$$\sigma_\eta\left(m^{-1}\right) = \frac{1}{V}\frac{P_{S\_\eta} \big/ \hbar\omega_S}{I_L \big/ \hbar\omega_L} \tag{A.4.35}$$

where P_{S_η} is the Stokes power, I_L the laser irradiance and ω_L the laser angular frequency.

By integrating over all the solid angles Ω, the scattering cross-section becomes

$$\sigma_\eta = \frac{1}{V}\frac{\omega_L}{\omega_S}\frac{1}{I_L}\int_{4\pi} I_{S\_\eta} r^2 d\Omega \tag{A.4.36}$$

Let us introduce the differential scattering cross-section, defined as $\sigma_\eta = \int_{4\pi}\frac{d\sigma_\eta}{d\Omega}d\Omega$, which implies the following

$$\begin{aligned}\frac{d\sigma_\eta}{d\Omega}\left(m^{-1}.sr^{-1}\right) &= \frac{1}{V}\frac{\omega_L}{\omega_S}\frac{1}{I_L} I_{S\_\eta} r^2 \\ &= \frac{1}{V}\frac{\omega_L}{\omega_S}\frac{1}{I_L} r^2 \frac{V^2}{32\pi^2\varepsilon_0 c^3 r^2}\int_{-\infty}^{+\infty} n_S \omega_S^4 \left\langle \left| P_{nuc\_i}^{(3)}(\omega_S) \right|^2 \right\rangle d\omega_S \\ &= \frac{V\omega_L}{32\pi^2\varepsilon_0 c^3 \omega_S I_L}\int_{-\infty}^{+\infty} n_S \omega_S^4 \left\langle \left| P_{nuc\_i}^{(3)}(\omega_S) \right|^2 \right\rangle d\omega_S\end{aligned} \tag{A.4.37}$$

In the same way, we bring in the spectral differential scattering cross-section defined as $\frac{d\sigma_\eta}{d\Omega} = \int_{-\infty}^{+\infty}\frac{\partial^2\sigma_\eta}{\partial\Omega\partial\omega_S}d\omega_S$, which is the fraction of incident photons per unit of length at the

laser angular frequency ω_L scattered non-elastically in a solid angle $\partial\Omega$ in a spectral window $\partial\omega_S$. It comes then

$$\frac{\partial^2\sigma_\eta}{\partial\Omega\partial\omega_S}\left(m^{-1}.sr^{-1}.s\right)=\frac{V\omega_L}{32\pi^2\varepsilon_0 c^3 I_L}n_S\omega_S^3\left\langle\left|P^{(3)}_{nuc\_i}(\omega_S)\right|^2\right\rangle \tag{A.4.38}$$

By inserting the expression of the laser irradiance $I_L=\frac{1}{2}n_L c\varepsilon_0\left|E_L\right|^2$, where E_L is the laser electric field, in the previous equation, one can obtain

$$\frac{\partial^2\sigma_\eta}{\partial\Omega\partial\omega_S}=\frac{n_S\omega_L\omega_S^3V\left\langle\left|P^{(3)}_{nuc\_i}(\omega_S)\right|^2\right\rangle}{16\pi^2\varepsilon_0^2c^4n_L\left|E_L\right|^2} \tag{A.4.38}$$

Now, we would like to relate this last equation to the third-order nuclear susceptibility. To do that, we will use the quantum mechanics fluctuation-dissipation theorem (or Nyquist's formula). In a general way, this theorem states that the mean-square fluctuation in some physical quantity is related to the imaginary part of an appropriately defined susceptibility. Mathematically, this is expressed for the present case as

$$\left\langle\left|P^{(3)}_{nuc\_i}(\omega_S)\right|^2\right\rangle=\frac{\varepsilon_0\hbar}{10\pi V}n_{BE}(\omega_V;T)\,\mathrm{Im}\left\{D^{(3)}_{ijkl}(\omega_V)\right\}\left|E_L\right|^2 \tag{A.4.39}$$

where $n_{BE}(\omega_V;T)=\left[1-\exp\left(\frac{\hbar\omega_V}{k_BT}\right)\right]^{-1}$ is the Bose-Einstein population factor, k_B the Boltzmann constant and T the temperature. The Bose-Einstein population factor is a correction for the thermal statistical fluctuations.

By substituting equation (A.4.39) into equation (A.4.38), the following formula is obtained

$$\frac{\partial^2\sigma_\eta}{\partial\Omega\partial\omega_S}=\frac{\hbar\omega_L\omega_S^3n_S}{160\pi^3\varepsilon_0c^4n_L}n_{BE}(\omega_V;T)\,\mathrm{Im}\left\{D^{(3)}_{ijkl}(\omega_V)\right\} \tag{A.4.40}$$

Since $\omega_S \approx \omega_L$, we can assume that $n_S \approx n_L$. Finally, the imaginary part of the nuclear third-order susceptibility is related to the spectral differential cross-section of spontaneous Raman scattering by the following relation

$$\mathrm{Im}\left\{D_{ijkl}^{(3)}(\omega_V)\right\} = \frac{160\pi^3\varepsilon_0 c^4}{\hbar\omega_L\omega_S^3}\frac{\partial^2\sigma_\eta}{\partial\Omega\partial\omega_S}\left[1-\exp\left(-\frac{\hbar\omega_V}{k_B T}\right)\right] \tag{A.4.41}$$

From equation (A.4.41), it is obvious that the imaginary part of the nuclear susceptibility can be determined from a Raman scattering experiment with absolute spectral differential cross-section.

By performing the following Kramers-Krönig integral, the real part of the nuclear susceptibility can also be found

$$\mathrm{Re}\left\{D_{ijkl}^{(3)}(\omega_V)\right\} = \frac{1}{\pi}\wp\int_{-\infty}^{+\infty}\frac{\mathrm{Im}\left\{D_{ijkl}^{(3)}(s)\right\}}{s-\omega_V}ds \tag{A.4.42}$$

The Kramers-Krönig relation integrates over all the angular frequencies, from $-\infty$ to $+\infty$. However, Raman spectroscopy of glasses stands on a limited range of frequencies, in general from 0 to 2000 cm^{-1}. Fortunately, above this value, the Raman signal is null and the integration can be performed as if it was over an infinite range of frequencies. Therefore, in principle at least, a Raman spectrum uniquely can lead to the determination of both the imaginary and real parts of the nuclear susceptibility.

As shown before, it is possible to compute directly the imaginary part of the functions A and B from polarized (// or VV-HH) and depolarized ($\perp$ or HV-VH) Raman spectra as follow

$$\begin{cases}\mathrm{Im}\{A(\omega_V)\} = \dfrac{160\pi^3\varepsilon_0 c^4}{\hbar\omega_L(\omega_L-\omega_V)^3}\left(\dfrac{1}{2}\dfrac{\partial^2\sigma_{//}}{\partial\Omega\partial\omega_S}-\dfrac{\partial^2\sigma_\perp}{\partial\Omega\partial\omega_S}\right)\left[1-\exp\left(-\dfrac{\hbar\omega_V}{k_B T}\right)\right] \\ \mathrm{Im}\{B(\omega_V)\} = \dfrac{160\pi^3\varepsilon_0 c^4}{\hbar\omega_L(\omega_L-\omega_V)^3}\dfrac{\partial^2\sigma_\perp}{\partial\Omega\partial\omega_S}\left[1-\exp\left(-\dfrac{\hbar\omega_V}{k_B T}\right)\right]\end{cases} \tag{A.4.43}$$

In terms of wave number and wavelength (parameters used in practice), these expressions become

$$\begin{cases} \mathrm{Im}\{A(\sigma_V)\} = \dfrac{10\varepsilon_0\lambda_L}{\pi hc\left(\dfrac{1}{\lambda_L}-\sigma_V\right)^3}\left(\dfrac{1}{2}\dfrac{\partial^2\sigma_{//}}{\partial\Omega\partial\sigma_S}-\dfrac{\partial^2\sigma_{\perp}}{\partial\Omega\partial\sigma_S}\right)\left[1-\exp\left(-\dfrac{hc\sigma_V}{k_BT}\right)\right] \\ \mathrm{Im}\{B(\sigma_V)\} = \dfrac{10\varepsilon_0\lambda_L}{\pi hc\left(\dfrac{1}{\lambda_L}-\sigma_V\right)^3}\dfrac{\partial^2\sigma_{\perp}}{\partial\Omega\partial\sigma_S}\left[1-\exp\left(-\dfrac{hc\sigma_V}{k_BT}\right)\right] \end{cases} \quad \text{(A.4.44)}$$

where λ_L is the laser wavelength, σ_S the Stokes wave number and σ_V the vibrational wave number.

From this point, two methods exist to calculate the functions a and b. The first one, which is quite laborious, is based on the Kramers-Krönig relations. The second one, more direct, relies on the cosine and sine Fourier transforms.

First method:

Once the imaginary parts of the functions A and B are computed, the Kramers-Krönig integral permits to determine their real part as follow

$$\begin{cases} \mathrm{Re}\{A(\omega_V)\} = \dfrac{1}{\pi}\wp\int_{-\infty}^{+\infty}\dfrac{\mathrm{Im}\{A(s)\}}{s-\omega_V}ds \\ \mathrm{Re}\{B(\omega_V)\} = \dfrac{1}{\pi}\wp\int_{-\infty}^{+\infty}\dfrac{\mathrm{Im}\{B(s)\}}{s-\omega_V}ds \end{cases} \quad \text{(A.4.45)}$$

Once the real and imaginary parts of the functions A and B are computed, they can be written in complex notation as follow

$$\begin{cases} A(\omega_V) = \mathrm{Re}\{A(\omega_V)\} + i\,\mathrm{Im}\{A(\omega_V)\} \\ B(\omega_V) = \mathrm{Re}\{B(\omega_V)\} + i\,\mathrm{Im}\{B(\omega_V)\} \end{cases} \quad \text{(A.4.46)}$$

Then, the functions a and b are found by using the inverse Fourier transform

$$\begin{cases} a(t) = \dfrac{1}{2\pi}\int_{-\infty}^{+\infty} A(\omega_V)\exp(-i\omega_V t)d\omega_V \\ b(t) = \dfrac{1}{2\pi}\int_{-\infty}^{+\infty} B(\omega_V)\exp(-i\omega_V t)d\omega_V \end{cases} \quad \text{(A.4.47)}$$

Second method:

The second method uses the parity of the functions A and B. Since their imaginary part is an odd function, the functions a and b can be found by a sine Fourier transform

$$\begin{cases} a(t) = \dfrac{2}{\pi}\int_{0}^{+\infty} \mathrm{Im}\{A(\omega_V)\}\sin(\omega_V t)d\omega_V \\ b(t) = \dfrac{2}{\pi}\int_{0}^{+\infty} \mathrm{Im}\{B(\omega_V)\}\sin(\omega_V t)d\omega_V \end{cases} \quad \text{(A.4.48)}$$

The knowledge of the functions a and b gives access to all the different tensor elements of the nuclear response function, as shown as follow

$$\begin{cases} d_{xxxx}(t) = a(t) + b(t) \\ d_{xyxy}(t) = \dfrac{1}{2}b(t) \\ d_{xxyy}(t) = a(t) \\ d_{xyyx}(t) = \dfrac{1}{2}b(t) \end{cases} \quad \text{(A.4.49)}$$

with $d_{xxxx}(t) = d_{xxyy}(t) + d_{xyxy}(t) + d_{xyyx}(t)$.

The challenge is the measurement the Raman differential spectral cross-section. Absolute measurements are very difficult to perform in spontaneous Raman scattering spectroscopy. They require knowledge of the exact amount of power scattered in the given solid angle and this is a hard task to do. That is why spontaneous Raman scattering measurements are usually carried out relative to a reference sample, whose spectral differential cross-section is known with accuracy. Nevertheless, this measurement on a reference sample had to be done in an absolute manner. This was achieved with enough accuracy by Kato and Takuma [Kat71] who determined the spectral differential cross-section of liquid benzene with 3% of uncertainty, relative to the radiation of a perfectly calibrated

blackbody. The very good knowledge of the radiation of a blackbody explains this very low uncertainty. The same year, the same authors performed wavelength-dependence measurements of the spectral differential cross-section [Kat71bis], opening the door to measurements of any sample relative to liquid benzene at many wavelengths.

Hellwarth *et al.* in 1975 [Hel75] measured first the polarized spectral differential cross-section $\frac{\partial\sigma_{//}}{\partial\Omega\partial\sigma_S}$ of fused silica at 514.5 nm relative to liquid benzene with 10% of uncertainty. In the sequel, other measurements at different wavelengths have been performed and a recapitulation of these values for the line at 440 cm^{-1} is given in figure 4, in which one can notice the well known $1/\lambda_S^4$ dependence of the cross-section. Thus, rather than performing measurements relative to liquid benzene, it is possible to directly compare the Raman cross-section of any glass with respect to fused silica, which is a reference material in the literature.

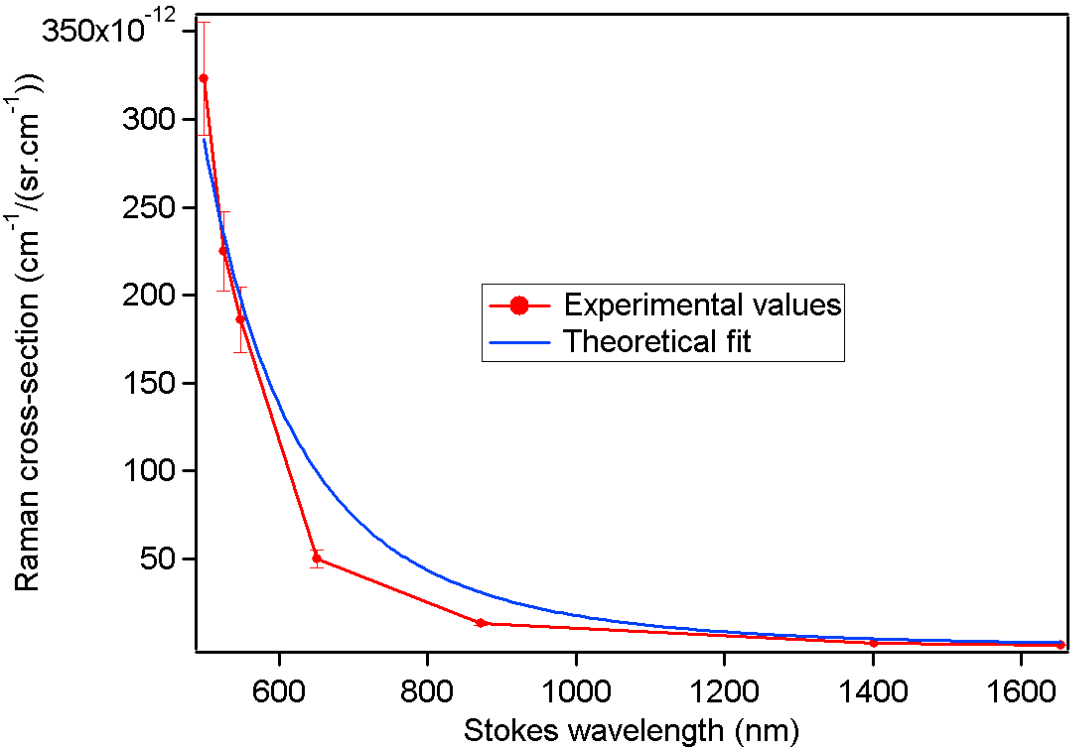

Figure 4: Evolution of the differential spectral Raman cross-section of the 440 cm^{-1} line of fused silica versus the Stokes wavelength. The experimental values come from the references

[Sto73], [Hel75], [Hei79] and [Far99]. The fitted curve shows the $1/\lambda_S^4$ dependence of the cross-section.

However, to measure the Raman cross-section of glasses with respect to fused silica, three types of refractive index correction have to be performed besides the ω_S^4 dependence:

- A correction due to the resonant enhancement of the polarizability for angular frequencies well below any electronic resonance. The corresponding corrective factor is $n^2(\omega_S)-1$ [Riv05bis].

- A correction due to the losses introduced by the reflection undergone by the laser beam on one face and by the scattered light on another. The corresponding corrective factor is $\frac{1}{[1-R(\omega_L)][1-R(\omega_S)]}$, where $R(\omega)=\left[\frac{n(\omega)-1}{n(\omega)+1}\right]^2$ is the Fresnel reflection coefficient under normal incidence [Gal78].

- A correction due to the refraction of the scattered light which is different from a sample to another, leading to a change of the collection solid angle. The corresponding corrective factor is $n^2(\omega_S)$ [Gal78].

The experimental Raman setup is described in figure 5. A 90 degree collection configuration has been chosen rather than forward-scattering or back-scattering configurations in order to avoid the use of a Notch filter and thus to be able to have access to low vibrational frequencies. With a Notch filter, vibrational frequencies below 200 cm^{-1} are not accessible. That is why a triple monochromator is preferred (to ensure good spectral resolution).

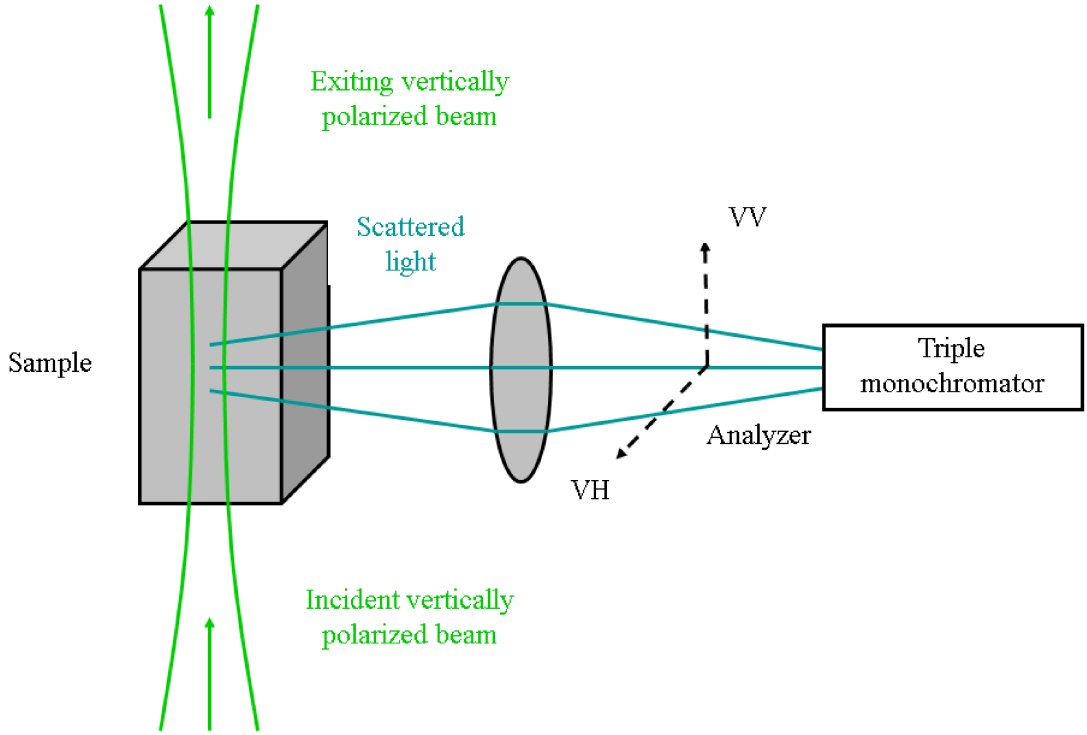

Figure 5: Spontaneous Raman scattering experimental setup.

4.8. Summary

This chapter showed that the electronic and nuclear contributions to the third-order susceptibility can be distinguished within the framework of the Born-Oppenheimer approximation. This achievement is of importance because each contribution can be evaluated separately. For example, an experiment based on third-harmonic generation, an electronic process, will measure the electronic contribution. On the other hand, an experiment based on optical Kerr effect will be sensitive to both electronic and nuclear contributions. Finally, from expression (A.4.43), the nuclear contribution will be determined from Raman spectroscopy.

CHAPTER FIVE: TWO DEGENERATE THIRD-ORDER PROCESSES IN THE BO APPROXIMATION

A monochromatic electric field of the form $\vec{E}(\vec{r};t)=\vec{A}(\vec{r};t)\cos\left(\vec{k}_{\omega}.\vec{r}-\omega t\right)$ incident onto a material induces a third-order nonlinear polarization, which is the sum of two different contributions: one at the angular frequency ω, responsible for the Optical Kerr Effect (OKE) and one at the angular frequency 3ω, responsible for the Third-Harmonic Generation (THG) process.

THG is a purely electronic process, since only the electronic polarization is able to quickly respond to a high-frequency all-optical field excitation. The cubic polarization associated to the THG process is given by

$$\vec{P}^{(3)}_{i\_3\omega}(\vec{r};t)=\frac{1}{4}\varepsilon_0\sigma^{(3)}_{ijkl}\vec{A}_j(\vec{r};t)\vec{A}_k(\vec{r};t)\vec{A}_l(\vec{r};t)\cos\left(3\vec{k}_{\omega}.\vec{r}-3\omega t\right) \tag{A.5.1}$$

where $\sigma^{(3)}_{ijkl}=\chi^{(3)}_{ijkl}(-3\omega;\omega,\omega,\omega)$ is the THG susceptibility.

The OKE is a process which is sensitive both to electronic and nuclear contributions. As discussed in chapter 3, the nuclear contribution is more or less important, depending on the pulse duration of the laser. The cubic polarization associated to the OKE is given by

$$\begin{aligned}\vec{P}^{(3)}_{i\_\omega}(\vec{r};t)=&\frac{3}{4}\varepsilon_0\sigma^{(3)}_{ijkl}\vec{A}_j(\vec{r};t)\vec{A}_k(\vec{r};t)\vec{A}^{*}_l(\vec{r};t)\cos\left(\vec{k}_{\omega}.\vec{r}-\omega t\right)\\&+\frac{1}{2}\varepsilon_0\vec{A}_j(\vec{r};t)\cos\left(\vec{k}_{\omega}.\vec{r}-\omega t\right)\int_{-\infty}^{t}d^{(3)}_{ijkl}(\vec{r};t-\tau)\vec{A}_k(\vec{r};\tau)\vec{A}^{*}_l(\vec{r};\tau)d\tau\end{aligned} \tag{A.5.2}$$

5.1. Third-harmonic generation

5.1.1. Theory

THG is a coherent third-order nonlinear process related to the third-order susceptibility $\chi^{(3)}(-3\omega;\omega,\omega,\omega)=\chi^{(3)}$ that mixes three photons at the optical angular frequency ω to

generate a photon at three times the angular frequency of the incident photons, *i.e.* 3ω. It is a pure electronic process, since only the electronic polarization is able to quickly respond to a high-frequency all-optical field excitation. The energy diagram for THG is shown in figure 6.

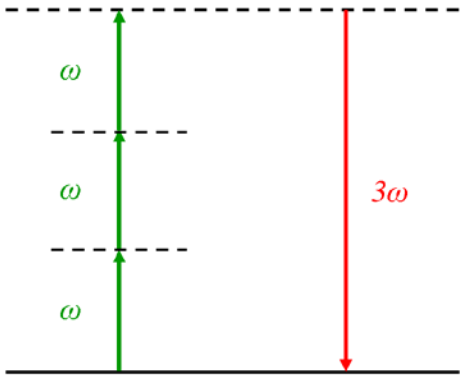

Figure 6: Energy diagram of the THG process. The full lines represent real energy levels whereas the dashed lines represent virtual energy levels.

5.1.1.1. THG in a bulk material

Let us consider an incident monochromatic linearly polarized beam at the angular frequency ω propagating in the positive z-direction (direct wave) for which the electric field is of the form

$$\vec{E}_{\omega}(\vec{r};t)=\frac{1}{2}\left\{\vec{A}_{\omega}(\vec{r})\exp\left[i\left(k_{\omega}z-\omega t\right)\right]+\vec{A}_{\omega}^{*}(\vec{r})\exp\left[-i\left(k_{\omega}z-\omega t\right)\right]\right\} \tag{A.5.3}$$

The THG polarization oscillating at the angular frequency 3ω is given by

$$\vec{P}_{3\omega}(\vec{r};t)=\frac{1}{2}\left\{\vec{p}_{3\omega}(\vec{r})\exp\left[i\left(3k_{\omega}z-3\omega t\right)\right]+\vec{p}_{3\omega}^{*}(\vec{r})\exp\left[-i\left(3k_{\omega}z-3\omega t\right)\right]\right\} \tag{A.5.4}$$

where $\vec{p}_{3\omega}(\vec{r})=\frac{1}{4}\varepsilon_0\chi^{(3)}\vec{A}_{\omega}^{3}(\vec{r})$ and $\chi^{(3)}\equiv\chi^{(3)}(-3\omega;\omega,\omega,\omega)$.

The scalar paraxial equation for the third-harmonic electric field is derived from the general paraxial equation (A.2.37) and is given by

$$\nabla_{\perp}^{2}A_{3\omega}(\vec{r})+2ik_{3\omega}\frac{\partial A_{3\omega}(\vec{r})}{\partial z}=-\mu_0(3\omega)^2\,p_{3\omega}(\vec{r})\exp(i\Delta kz) \tag{A.5.5}$$

where $\Delta k = 3k_\omega - k_{3\omega}$ is the phase mismatch between the fundamental and the third-harmonic waves and $k_\omega = n_\omega \frac{\omega}{c}$ and $k_{3\omega} = n_{3\omega} \frac{3\omega}{c}$ the wave vectors of the fundamental and third-harmonic beams, respectively.

In the case of Gaussian beams, the expressions of the fundamental and third-harmonic electric fields are given by

$$\begin{cases} A_\omega(\rho;z) = A_{0\_\omega} \frac{w_0}{w(z)} \exp\left[\frac{-\rho^2}{w^2(z)}\right] \exp\left[i\frac{k_\omega \rho^2}{2R(z)}\right] \exp[i\phi(z)] \\ A_{3\omega}(\rho;z) = A_{0\_3\omega}(z) \frac{w_0}{w(z)} \exp\left[\frac{-3\rho^2}{w^2(z)}\right] \exp\left[i\frac{k_{3\omega} \rho^2}{2R(z)}\right] \exp[i3\phi(z)] \end{cases} \quad \text{(A.5.6)}$$

where w_0 is the beam waist of the fundamental wave, $w(z) = w_0 \sqrt{1 + \left(\frac{z}{z_R}\right)^2}$ the radius of the beam, $R(z) = z\left[1 + \left(\frac{z_R}{z}\right)^2\right]$ the radius of curvature of the wave front, $\phi(z) = -\arctan\left(\frac{z}{z_R}\right)$ the Gouy phase shift of the wave, $z_R = \frac{\pi w_0^2}{\lambda}$ the Rayleigh length, $\rho = \sqrt{x^2 + y^2}$ the radial coordinate and z the longitudinal coordinate.

For a theoretical work, it is more convenient to represent a Gaussian beam in a more compact but less intuitive form

$$\begin{cases} A_\omega(\rho;z) = \frac{A_{0\_\omega}}{1+i\xi} \exp\left[\frac{-\rho^2}{w_0^2(1+i\xi)}\right] \\ A_{3\omega}(\rho;z) = \frac{A_{0\_3\omega}(z)}{1+i\xi} \exp\left[\frac{-3\rho^2}{w_0^2(1+i\xi)}\right] \end{cases} \quad \text{(A.5.7)}$$

where $\xi = \frac{z}{z_R} = \frac{2z}{b}$ is a longitudinal coordinate (dimensionless) defined in terms of confocal parameter $b = 2z_R = \frac{2\pi w_0^2}{\lambda} = k_\omega w_0^2$.

Substituting these expressions into the paraxial equation with no transverse dependence ($\rho \mapsto 0$) gives the following differential equation, which translates the evolution of the amplitude of the third-harmonic electric field with respect to the distance z

$$\frac{dA_{0\_3\omega}(z)}{dz} = i\frac{3\omega}{8n_{3\omega}c}\chi^{(3)}A_{0\_\omega}^{3}\frac{\exp(i\Delta kz)}{(1+i\xi)^{2}} \tag{A.5.8}$$

The solution of this equation is

$$A_{0\_3\omega}(z) = i\frac{3\omega}{8n_{3\omega}c}A_{0\_\omega}^{3}\chi^{(3)}J_{3\omega}(\Delta k; z_0; z) \tag{A.5.9}$$

where $J_{3\omega}(\Delta k; z_0; z) = \int_{z_0}^{z}\frac{\exp(i\Delta ku)}{\left(1+\frac{2iu}{b}\right)^{2}}du$ is the third-harmonic interaction length and z_0 the position of the entrance of the medium; the position of the beam waist is set to be at $z = 0$ (*cf.* figure 7).

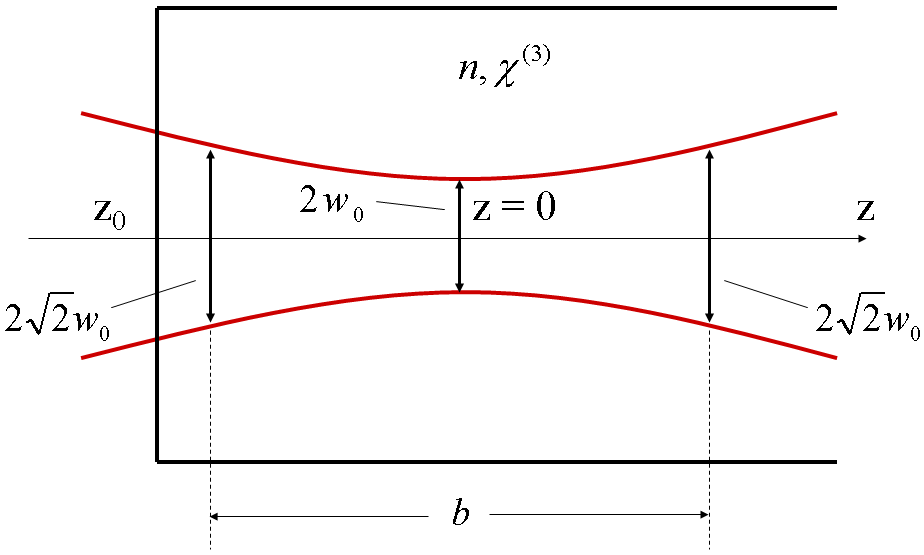

Figure 7: Geometry of the experiment with a Gaussian beam focused inside a bulk material.

This third-harmonic interaction length can be evaluated analytically in two particular cases. The first case corresponds to a slightly focused beam (plane wave limit), for which

$b >> |z_0|$ and $|z|$. In this plane wave limit, the usual phase matching behavior is found (*cf.* figure 8) since the third-harmonic interaction length is written as

$$\left|J_{3\omega}(\Delta k; z_0; z)\right|^2 = \left|\int_{z_0}^{z} \exp(i\Delta k u)du\right|^2 = \left|\frac{\exp(i\Delta k z) - \exp(i\Delta k z_0)}{i\Delta k}\right|^2 = L^2 \mathrm{sinc}^2\left(\frac{\Delta k L}{2}\right)$$

(A.5.10)

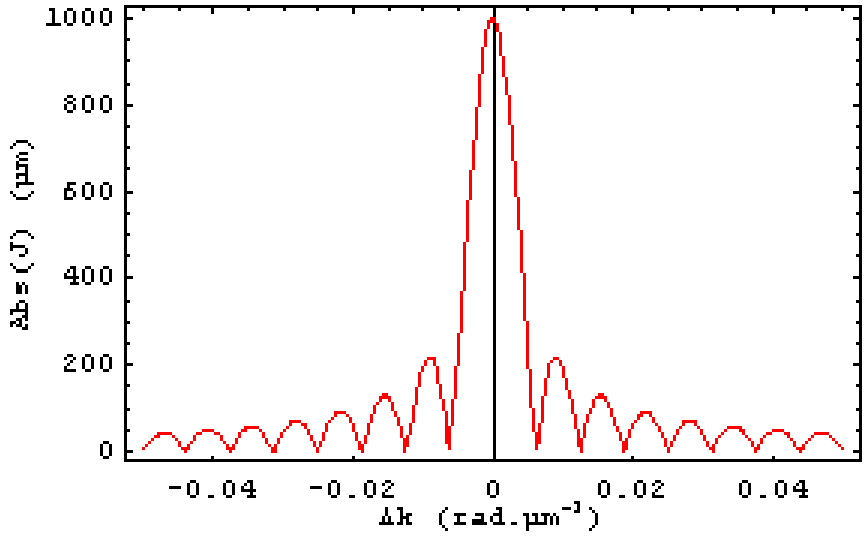

Figure 8: Evolution of the modulus the third-harmonic interaction length versus the phase mismatch (in the plane wave limit) computed for $L = z - z_0$, $z_0 = -1\,\mathrm{mm}$ and $z = 0$.

The second case corresponds to a strongly focused beam inside the medium, for which $z_0 = -|z_0|$, $z = |z|$ and $b << |z_0|$ and $|z|$ and the third-harmonic interaction length can be evaluated by a contour integral (*cf.* figure 9)

$$J_{3\omega}(\Delta k; z_0; z) = \int_{-\infty}^{+\infty} \frac{\exp(i\Delta k u)}{\left(1 + \frac{2iu}{b}\right)^2} du = \begin{cases} 0 \text{ if } \Delta k \le 0 \\ \pi \frac{b^2}{2} \Delta k \exp\left(-\frac{b\Delta k}{2}\right) \text{ if } \Delta k > 0 \end{cases} \qquad \text{(A.5.11)}$$

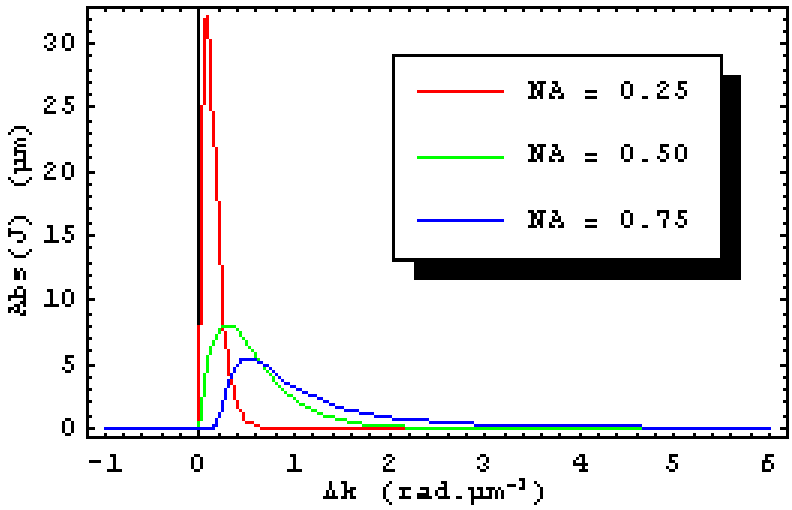

Figure 9: Evolution of the modulus of the third-harmonic interaction length versus the phase mismatch (in the strongly focused beam limit) computed for different numerical apertures ($NA = 0.25, 0.50$ and 0.75).

Finally, the third-harmonic irradiance generated in a bulk material and detected in the far-field is given by

$$I_{3\omega} = \left(\frac{3\omega}{4\varepsilon_0 c^2} \right)^2 \frac{1}{n_{3\omega} n_\omega^3} I_\omega^3 \left| \chi^{(3)} J_{3\omega}(\Delta k; z_0; z) \right|^2 \qquad \text{(A.5.12)}$$

From equation (A.5.11), one can notice that the third-harmonic interaction length is null when $\Delta k \leq 0$, which is the case for all the materials that have a normal dispersion in the wavelength range of interest ($\lambda_0/3 \rightarrow \lambda_0$). As a result, the third-harmonic irradiance is zero in the far-field when the incident fundamental laser beam is focused inside the medium. This is known as the Gouy phase shift anomaly, as it is explicitly illustrated in figure 10. For a positive phase mismatch (a), since the wave vectors of the fundamental beam present an angular dispersion due to its Gaussian nature (b), THG can occur with high efficiency. This cannot happen for a negative phase mismatch (c).

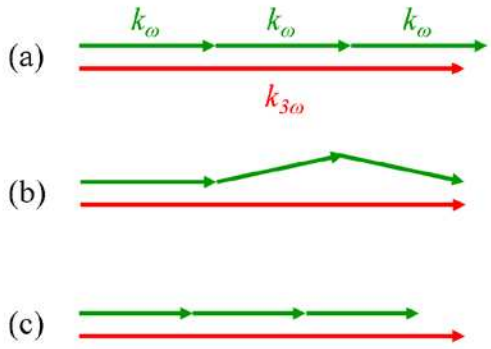

Figure 10: Wave vector diagrams for THG.

5.1.1.2. THG in the vicinity of an interface

Thus, if the fundamental beam is focused in the vicinity of an interface separating two media of different refractive indices and/or third-order susceptibilities (*cf.* figure 11), an appreciable third-harmonic beam can be detected in the far-field even if the media has a negative or null phase mismatch.

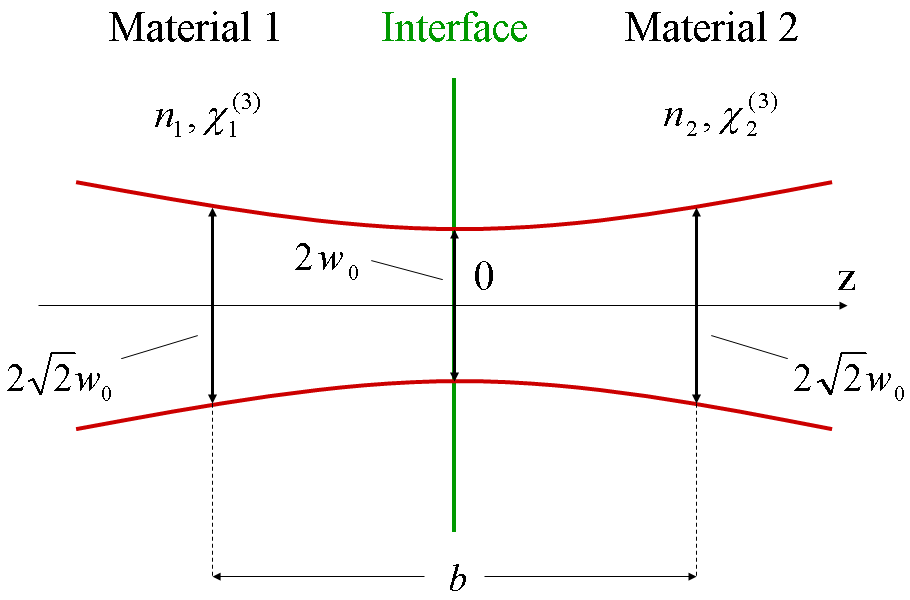

Figure 11: Geometry of the experiment with a focused Gaussian beam in the vicinity of an interface separating two media with different optical properties.

This is the imaging principle of THG microscopy [Bar97]. If the interface separates two infinite media with different refractive indices n_i and different third-order susceptibilities $\chi_i^{(3)}$ $(i = 1 \text{ or } 2)$ with the interface at $z = 0$, the third-harmonic irradiance in the far-field is

$$I_{3\omega} = \left(\frac{3\omega}{4\varepsilon_0 c^2}\right)^2 I_\omega^3 \left| \frac{n_{\omega,1}^{3/2}}{n_{3\omega,1}} \chi_1^{(3)} J_{3\omega,1}(\Delta k_1; -\infty; 0) + \frac{n_{\omega,2}^{3/2}}{n_{3\omega,2}} \chi_2^{(3)} J_{3\omega,2}(\Delta k_2; 0; +\infty) \right|^2 \quad \text{(A.5.13)}$$

Although equation (A.5.13) appears complicated, it can be simplified in two particular cases [Bro05]. The first case is an interface air/semi-infinite material. The third-order susceptibility of air (~ 10^{-25} $m^2.V^{-2}$) is negligible compared to that of the material. The third-harmonic irradiance is therefore given by

$$I_{3\omega} = \left(\frac{3\omega}{4\varepsilon_0 c^2}\right)^2 I_\omega^3 \left| \frac{n_{\omega,2}^{3/2}}{n_{3\omega,2}} \chi_2^{(3)} J_{3\omega,2}(\Delta k_2; 0; +\infty) \right|^2 \quad \text{(A.5.14)}$$

The second case is an interface separating two media presenting identical refractive indices and different third-order susceptibilities. This implies the following relations: $n_{\omega,1} = n_{\omega,2} = n_\omega$, $n_{3\omega,1} = n_{3\omega,2} = n_{3\omega}$, $\Delta k_1 = \Delta k_2 = \Delta k$ and $J_{3\omega,1}(\Delta k_1; -\infty; 0) = -J_{3\omega,2}(\Delta k_2; 0; +\infty)$. The third-harmonic irradiance is therefore given by

$$I_{3\omega} = \left(\frac{3\omega}{4\varepsilon_0 c^2}\right)^2 I_\omega^3 \frac{n_\omega^3}{n_{3\omega}^2} \left| J_{3\omega,1}(\Delta k; -\infty; 0) \right|^2 \left| \chi_1^{(3)} - \chi_2^{(3)} \right|^2 \quad \text{(A.5.15)}$$

5.1.1.3. THG with circularly polarized beams

Let us now discuss the symmetry properties of the THG process with either a linear ($E_y = aE_x$) or circular ($E_y = iE_x$) polarization. Considering an isotropic material, the Kleinman symmetry conditions show that the third-order susceptibility tensor presents 21 nonzero elements of which only 3 are independent. They are [But90]

$$\begin{cases} xxxx = yyyy = zzzz \\ yyzz = zzyy = zzxx = xxzz = xxyy = yyxx = \dfrac{\sigma}{3} \\ yzyz = zyzy = zxzx = xzxz = xyxy = yxyx = \dfrac{\sigma}{3} \\ yzzy = zyyz = zxxz = xzzx = xyyx = yxxy = \dfrac{\sigma}{3} \\ xxxx = xxyy + xyxy + xyyx = \sigma \end{cases} \tag{A.5.16}$$

Another way to write the third-order nonlinear polarization induced in the material is given by [But90]

$$\vec{P}_{i\_3\omega}(\vec{r};\omega) = \frac{1}{4}\varepsilon_0 \begin{bmatrix} \chi^{(3)}_{xxxx} E_x \left(E_x^2 + E_y^2\right) \\ \chi^{(3)}_{yyyy} E_y \left(E_x^2 + E_y^2\right) \\ 0 \end{bmatrix} \tag{A.5.17}$$

From equation (A.5.17), it appears that:

- The third-order nonlinear polarization induced by a linearly polarized electric field is not null and a THG signal can be generated. In this case, we have $\chi^{(3)}_{xxxx} = 3\chi^{(3)}_{xyxy} = 3\chi^{(3)}_{xyyx} = 3\chi^{(3)}_{xxyy}$.

- The third-order nonlinear polarization induced by a circularly polarized electric field is null; no third-harmonic can be generated with such a polarization. Nevertheless, if the material possesses a crystalline structure, the third-order nonlinear polarization is no longer null and THG can occur if the beam is focused in the vicinity of an interface. Hence, by changing the polarization of the incident beam, structural information of the studied material can be obtained [Oro03] [Oro04].

5.1.2. Experiment

The generic experimental setup is shown in figure 12. The laser source is an optical parametric oscillator (Spectra-Physics, Tsunami-Opal system) which delivers 130 fs pulses at the wavelength of 1500 nm at the repetition rate of 80 MHz. The laser beam is focused on the

sample with a microscope objective (*NA* = 0.75, *working distance* = 500 µm). The third-harmonic beam is collected with a condenser (*NA* = 0.6, *working distance* = 3 cm), filtered from the fundamental wavelength using an interference filter ($\lambda_0 = 500\,\text{nm}$, $\Delta\lambda = 40\,\text{nm}$) and measured with a photomultiplier tube (PMT, Hamamatsu R5700) [Bar02].

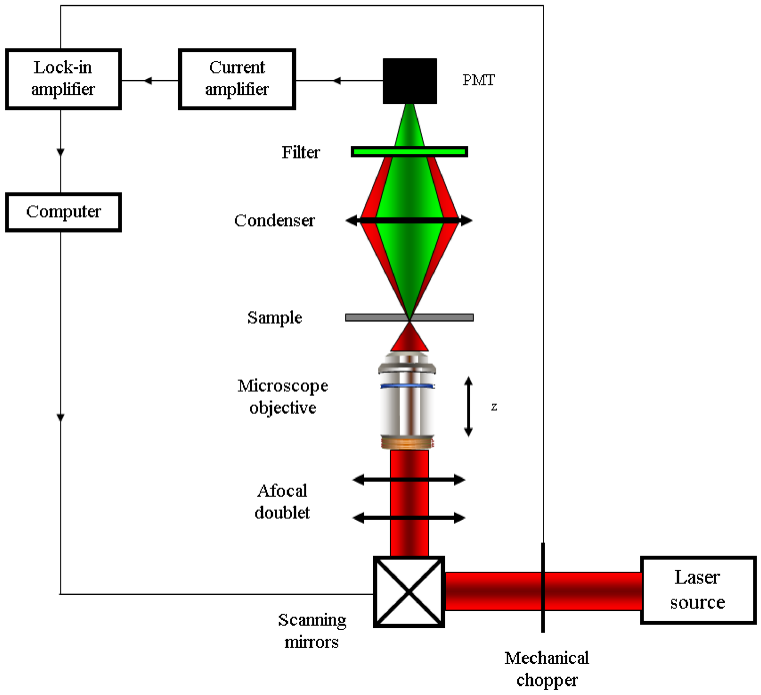

Figure 12: Generic THG microscopy experimental setup.

For measurement purposes, the photocurrent from the PMT is amplified and synchronously detected with a mechanical chopper via a lock-in amplifier, digitized and sent to a computer for acquisition. The sample is moved in the x-y-z-directions with piezoelectric translation stages. For imaging purposes, an x-y-scan of the beam is carried out in the sample with galvanometric mirrors. The photocurrent from the PMT is amplified and sent to a computer for acquisition. No lock-in amplifier is used because of its low response time.

The procedure to measure the $\chi^{(3)}$ value of a material from THG microscopy is the following. The third-harmonic signals generated by the investigated glass and a reference glass (fused silica in our case) are measured. When no significant two-photon absorption

occurs at both the fundamental and third-harmonic wavelengths, the imaginary part of the electronic susceptibility can be neglected and the calculated modulus of the susceptibility is set to the real part. Thus, the electronic susceptibility of the investigated glass relative to the reference glass is given by

$$\chi^{(3)}_{xxxx} = \sqrt{\frac{T_{3\omega,SiO_2} T^3_{\omega,SiO_2}}{T_{3\omega} T^3_{\omega}}} \sqrt{\frac{S_{3\omega}}{S_{3\omega,SiO_2}}} \sqrt{\frac{n_{3\omega} n^3_{\omega}}{n_{3\omega,SiO_2} n^3_{\omega,SiO_2}}} \left| \frac{J_{3\omega,SiO_2}\left(\Delta k_{SiO_2};0;L_{SiO_2}\right)}{J_{3\omega}\left(\Delta k;0;L\right)} \right| \chi^{(3)}_{xxxx,SiO_2}$$

(A.5.18)

where T_ω, n_ω, $T_{3\omega}$, $n_{3\omega}$ are the Fresnel transmission coefficients at normal incidence and the refractive indices at ω and 3ω, respectively, $S_{3\omega}$ the detected third-harmonic signal, $J_{3\omega}\left(\Delta k;0;L\right) = \int_0^L \frac{\exp\left(i\Delta k u\right)}{\left(1+\frac{2iu}{b}\right)^2} du$ the third-harmonic interaction length and L the sample thickness. The SiO_2 subscript refers to fused silica and no subscript is assigned to the investigated glass.

Knowing the refractive indices, the Fresnel transmission coefficients of both the investigated and the reference glasses at ω and 3ω as well as $\chi^{(3)}_{xxxx,SiO_2}$, one must apply equation (A.5.18) to determine the absolute $\chi^{(3)}$ value of the material under investigation. As a reference, we have chosen the value given by Hellwarth in 1977 for fused silica [Hel77] ($\chi^{(3)}_{xxxx} = 2.65\times10^{-22}$ m^2.V^{-2} $\pm 30\,\%$ at 694 nm). The huge uncertainty of the measurement of this value will be reported on our own measurement. However, if absolute measurements are not necessary, relative measurements (in % of $\chi^{(3)}_{xxxx,SiO_2}$) will be preferred, with an uncertainty of only 10%. This technique is unique because it enables to characterize both bulk and structured materials.

5.2. Optical Kerr effect

5.2.1. Theory

Contrary to THG, OKE relies on both electronic and nuclear effects, in the Born-Oppenheimer approximation. Therefore, it is a non-instantaneous process.

5.2.1.1. Phenomenological description of OKE

Let us consider an incident monochromatic linearly polarized beam at the angular frequency ω propagating in the positive z-direction (direct wave) which electric field is of the form

$$\vec{E}_\omega(\vec{r};t) = \frac{1}{2}\left\{\vec{A}_\omega(\vec{r})\exp\left[i\left(k_\omega z - \omega t\right)\right] + \vec{A}^*_\omega(\vec{r})\exp\left[-i\left(k_\omega z - \omega t\right)\right]\right\} \tag{A.5.19}$$

The OKE polarization oscillating at the angular frequency ω is given by

$$\vec{P}_\omega(\vec{r};t) = \frac{1}{2}\left\{\vec{p}_\omega(\vec{r})\exp\left[i\left(k_\omega z - \omega t\right)\right] + \vec{p}^*_\omega(\vec{r})\exp\left[-i\left(k_\omega z - \omega t\right)\right]\right\} \tag{A.5.20}$$

where $\vec{p}_\omega(\vec{r}) = \frac{3}{4}\varepsilon_0\chi^{(3)}\left|\vec{A}_\omega(\vec{r})\right|^2\vec{A}_\omega(\vec{r})$ and $\chi^{(3)} \equiv \chi^{(3)}(-\omega;\omega,-\omega,\omega)$.

The scalar paraxial equation for the electric field is derived from the general paraxial equation (A.2.37) and is given by

$$\nabla^2_\perp A_\omega(\vec{r}) + 2ik_\omega\frac{\partial A_\omega(\vec{r})}{\partial z} = -\mu_0\omega^2 p_\omega(\vec{r}) \tag{A.5.21}$$

OKE is responsible for self-focusing, self-phase modulation cross-phase modulation and two-photon absorption. In general, OKE is, in a phenomenological way, described by the famous equations

$$\begin{cases} n(I) = n_0 + n_2 I \\ \alpha(I) = \alpha_0 + \alpha_2 I \end{cases} \tag{A.5.22}$$

where n is the total refractive index, n_0 the linear refractive index, n_2 the nonlinear refractive index, α the total absorption coefficient, α_0 the linear absorption coefficient, α_2 the nonlinear absorption coefficient and I the irradiance.

The nonlinear refractive index and absorption coefficient are related to the OKE susceptibility $\chi^{(3)}(-\omega;\omega,-\omega,\omega)$ by the relations

$$\begin{cases} n_2 = \dfrac{3}{4\varepsilon_0 c n_0^2}\,\mathrm{Re}\left\{\chi^{(3)}(-\omega;\omega,-\omega,\omega)\right\} \\ \alpha_2 = \dfrac{3\omega}{2\varepsilon_0 n_0^2 c^2}\,\mathrm{Im}\left\{\chi^{(3)}(-\omega;\omega,-\omega,\omega)\right\} \end{cases} \qquad \text{(A.5.23)}$$

However, this description of OKE is true only if the associated physical mechanisms are instantaneous, that is, purely electronic. The energy diagram for purely electronic OKE is shown in figure 13.

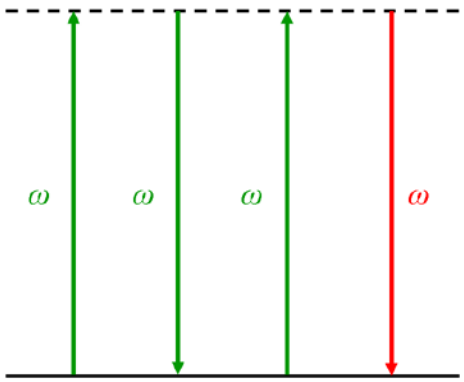

Figure 13: Energy diagram of the purely electronic OKE process. The full lines represent real energy levels whereas the dashed lines represent virtual energy levels.

5.2.1.2. OKE in an orthogonally-polarized pump-probe configuration

Our experiment to measure the OKE susceptibility is a pump-probe-type experiment with the pump and the probe pulses orthogonally polarized (*cf.* figure 14). The coupling between the pump and the probe pulses through the diagonal tensor elements of the third-

order susceptibility ($\chi^{(3)}_{xyxy} = \chi^{(3)}_{xyyx} = \chi^{(3)}_{xxyy}$) yields to nonlinear interferences in the probe irradiance. A careful analysis of the probe signal gives information on:

- The nonlinear absorption (imaginary part of the third-order susceptibility) through the average variation of the probe irradiance.

- The nonlinear refraction (real part of the third-order susceptibility) through the fast variations of the probe irradiance.

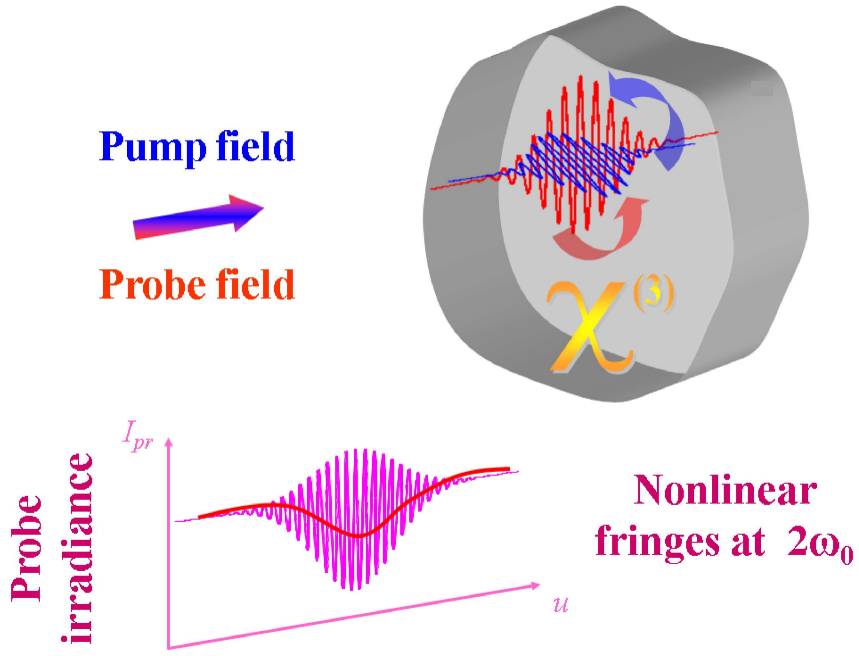

Figure 14: Principle of a pump-probe experiment with the pump and the probe pulses orthogonally polarized.

In this particular experiment, the third-order nonlinear polarization along the probe axis is developed as

$$\begin{aligned}\vec{p}_x^{(3)}(\vec{r};t) = &\frac{9}{4}\varepsilon_0\sigma^{(3)}_{xyxy}\vec{A}_x(\vec{r};t)\vec{A}_y^2(\vec{r};t)\\ &+\frac{1}{2}\varepsilon_0\vec{A}_x(\vec{r};t)\int_{-\infty}^{t} d^{(3)}_{xxyy}(t-\tau)\vec{A}_y^2(\vec{r};\tau)d\tau\\ &+\varepsilon_0\vec{A}_y(\vec{r};t)\int_{-\infty}^{t} d^{(3)}_{xyxy}(t-\tau)\vec{A}_x(\vec{r};\tau)\vec{A}_y(\vec{r};\tau)d\tau\end{aligned} \qquad \text{(A.5.24)}$$

The electric field envelope is assumed to be spatially Gaussian and temporally arbitrary and is given by

$$A(\rho;z;t)=\frac{A_0}{1+i\xi}\exp\left[\frac{-\rho^2}{w_0^2(1+i\xi)}\right]s(t) \tag{A.5.25}$$

where s is the temporal shape (dimensionless) of the pump or probe pulse.

The paraxial equation has no analytical solution. To be able to solve it, a perturbation development has to be performed. In this case, the general propagation equation for the probe beam with a nonlinear coupling with the pump beam is written as [San04]

$$\nabla_{\perp}^2 A_{pr}+2ik\frac{\partial A_{pr}}{\partial z}=-\frac{3}{4}k_0^2\left(\beta_1 A_{pr}\left|A_{pu}\right|^2+\beta_2 A_{pr}^* A_{pu}^2\right) \tag{A.5.26}$$

where k is the wave vector in the medium, $k_0=\frac{\omega}{c}$ the wave vector in the vacuum and β_1 and β_2 two perturbation variables given by [San04]

$$\beta_1=2\sigma_{xyxy}^{(3)}s(t)s^2(t-u)+\frac{1}{3}s(t)\int_{-\infty}^{t}d_{xxyy}^{(3)}(t-\tau)s^2(t-\tau)d\tau+\frac{1}{6}s(t-u)\int_{-\infty}^{t}d_{xyxy}^{(3)}(t-\tau)s(t-\tau)s(t-\tau-u)d\tau \tag{A.5.27}$$

$$\beta_2=\exp(-i2\omega u)\left[\sigma_{xyxy}^{(3)}s(t)s^2(t-u)+\frac{1}{6}s(t-u)\int_{-\infty}^{t}d_{xyxy}^{(3)}(t-\tau)s(t-\tau)s(t-\tau-u)d\tau\right] \tag{A.5.28}$$

such as $A_{pr}=X_0+(\beta_1+\beta_2)X_1$ with X_0 and X_1 the unperturbed and perturbed envelopes, respectively, and u the variable delay between the pump and the probe pulses.

The equation describing the probe irradiance variations is given by

$$I_{pr}\propto A_{pr}A_{pr}^*=I_{pr\_0}\left[1-\frac{k_0^2}{4\sqrt{2}}\frac{P_{av}}{c\varepsilon_0 R}F(w_0;k_0;L)\Lambda(u)G(u)\sin(2\omega u)\right] \tag{A.5.27}$$

where I_{pr_0} is the incident probe irradiance, P_{av} the average power, R the repetition rate of the laser, $F(w_0;k_0;L)$ a dimensionless numerical factor depending on the spatial properties of the laser beam, w_0 the beam waist and L the thickness of the sample.

Since our experiment utilizes 100 fs pulses, the probe signal is sensitive both to the electronic and the nuclear contributions. Thus, the global OKE susceptibility Λ includes both electronic and nuclear phenomena, and is given by

$$\Lambda(u) = \sigma^{(3)}_{xxxx} + \frac{H\left(d^{(3)}_{xyxy};u\right)}{G(u)} \tag{A.5.28}$$

The first term of the equation (A.5.28) is labeled as the electronic susceptibility and the second one as the nuclear susceptibility.

The function $G(u)$ is a temporal term, delay dependent, which represent the electronic contribution to the signal and it is defined as

$$G(u) = \frac{\int_{-\infty}^{+\infty} s(t)s(t-u)dt}{\left[\int_{-\infty}^{+\infty} s(t)dt\right]^2} \tag{A.5.29}$$

At zero delay, this function is equal to the ratio between the second-order momentum of $s(t)$ and the squared first-order momentum of $s(t)$.

The function $H\left(d^{(3)}_{xyxy};u\right)$ is a more complicated term owing to the non-instantaneous response of the Raman phenomena which represents the nuclear contribution to the signal. It is defined as

$$H\left(d^{(3)}_{xyxy};u\right) = \frac{\int_{-\infty}^{+\infty}\left[s(t)s(t-u)\int_{0}^{+\infty} d^{(3)}_{xyxy}(t-t_1)s(t_1)s(t_1-u)dt_1\right]dt}{\left[\int_{-\infty}^{+\infty} s^2(t)dt\right]^2} \tag{A.5.30}$$

This function includes the correlation of a classical convolution of the nuclear response function of the material with the temporal shape $s(t)$ of the laser pulse.

As shown before, it is possible to calculate the nuclear response function $d^{(3)}_{xyxy}$ from Raman spectra. Knowing this last, one can then determine the nuclear susceptibility by computing the ratio $\frac{H\left(d^{(3)}_{xyxy};u=0\right)}{G(u=0)}$.

5.2.2. Experiment

The experimental setup is shown in figure 15. The light source is a Ti:Sa laser (Spectra-Physics, Tsunami system) which delivers 150 fs pulses at the wavelength of 810 nm at the repetition rate of 80 MHz. The laser beam is unevenly balanced in a strong TM-polarized pump beam and a weak TE-polarized probe beam by using a half-wave plate combined to a polarizing beam-splitter cube. These two beams are further mixed with another polarizing cube, precisely adjusted to be exactly collinear, and are focused into the sample. The pump beam is then ejected by a Glan prism and the irradiance of the probe beam is recorded as a function of the delay between the pump and the probe pulses [San04].

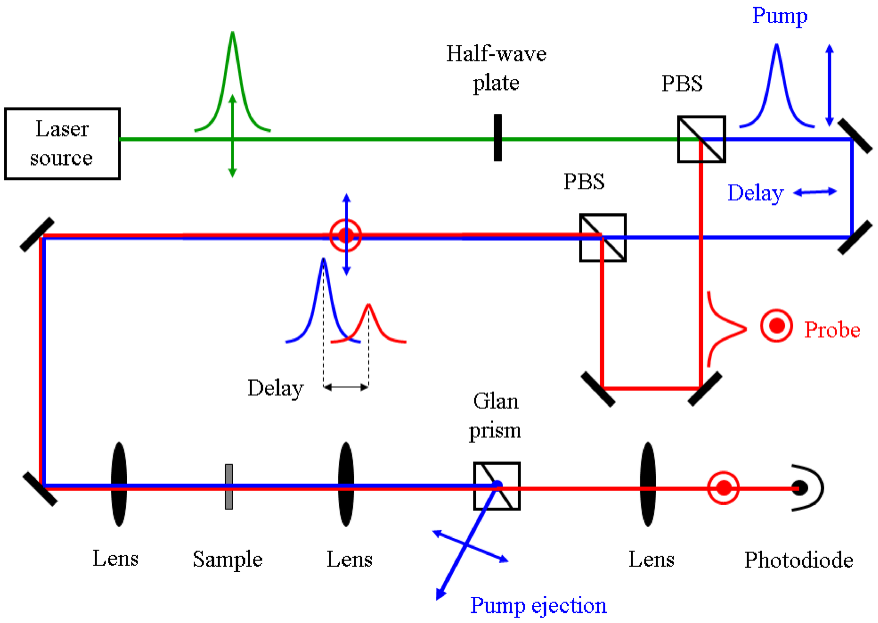

Figure 15: Generic OKE pump-probe experimental setup.

This technique is appropriate to characterize bulk materials. However, it is difficult to implement on structured materials for different reasons. First, the polarization of the pump and the probe pulses must perfectly be maintained after the focusing element, which is rarely

the case. Second, the nonlinear interaction length makes on the order of a few micrometers makes the signal too low to be detected.

CHAPTER SIX: APPLICATION TO DIFFERENT GLASS FAMILIES

Based upon Hellwarth's model, several measurements of the nuclear contribution in glasses have been performed in the femtosecond regime, either using time-resolved techniques [Tho85] [Kan96] [Mon98] [Smo99] [Abe00] [Mon08] or not [Pan95] [San04]. Smolorz *et al.* have, for instance, demonstrated that the relative nuclear contribution to the nonlinear refractive index increases upon addition of GeO_2 in a SiO_2 optical fiber [Smo99]. However, these results did not include the effect of the duration of the optical pulse, despite previous work by Stolen *et al.* [Sto92] which showed that the nuclear contribution is driven by the pulse duration. Hence, values of nuclear contributions are subject to change since they depend strongly on this important parameter.

In this chapter, Hellwarth's model is applied to two families of oxide glasses, namely fused silica and sodium-borophosphate-niobium glasses [Roy07]. The application of the model to fused silica aims to show its validity as a simple reference material. Both the electronic coefficient and the Raman cross-section used have been taken from the literature [Hel77]. The evolution of the nuclear contribution to the OKE is given. For the other glass family, THG and OKE susceptibility measurements have been performed with THG microscopy and pump-probe techniques, respectively. From these measurements, the nuclear contribution to the OKE has been deduced. Additionally, Raman scattering experiments have been carried out to evaluate theoretically the nuclear contribution to the OKE and compared to that measured by THG. The validity and the limitations of the model are also discussed.

6.1. Fused silica

The polarized (VV) and depolarized (VH) Raman experiments have been carried out from 90° spontaneous Raman scattering measurements at 514.5 nm (*cf.* figure 16) using an

experimental system allowing low frequency measurement. The reported value of silica [Hel75] $\{\frac{\partial^2\sigma_{//}}{\partial\Omega\partial\sigma_S} = 2.25.10^{-10}$ cm^{-1}.sr^{-1}.cm $\pm 10\,\%$ for the 440 cm^{-1} line at 514.5 nm, where $\sigma_S = \frac{\omega_S}{2\pi c}/\}$ has been considered.

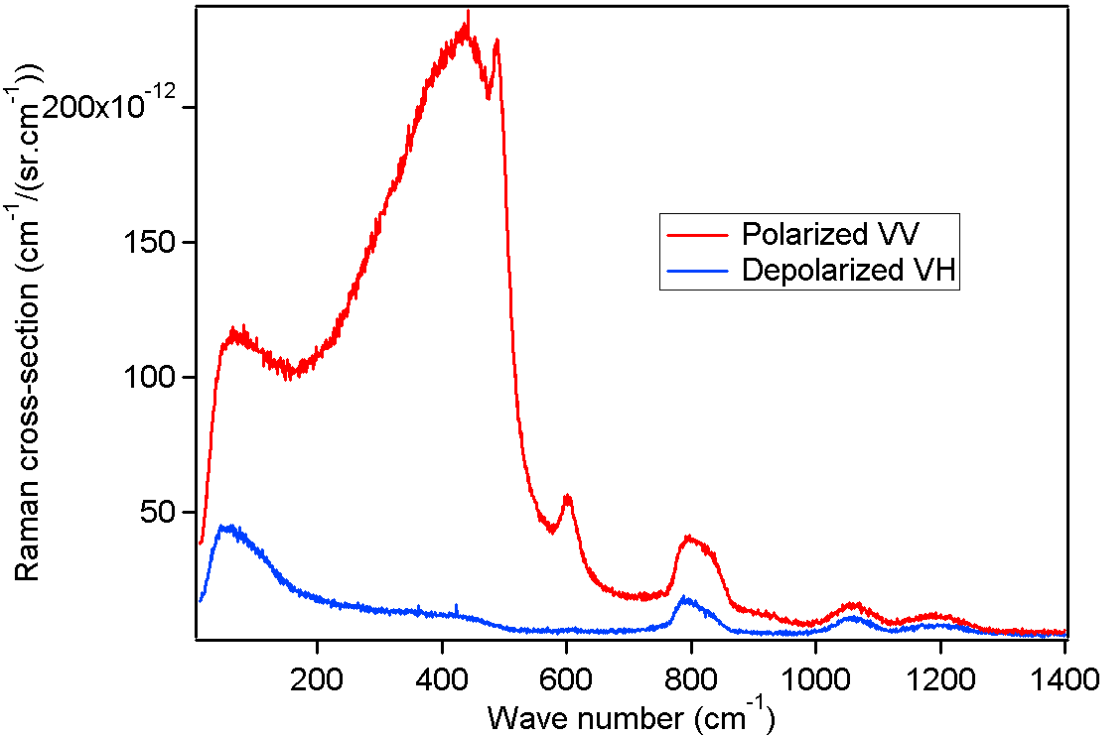

Figure 16: Absolute polarized (VV) and depolarized (VH) Raman spectra of fused silica at a 514.5 nm excitation wavelength.

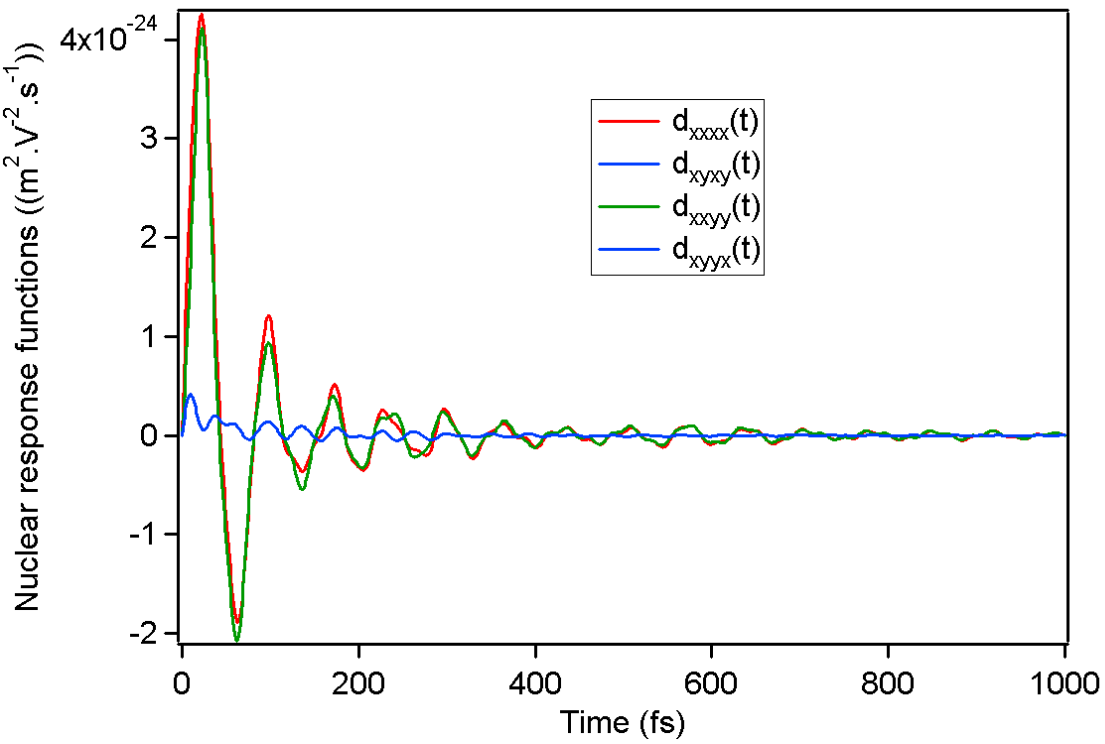

Figure 17: Relevant tensor elements of the nuclear response function of fused silica versus time.

Following Hellwarth's model, the nuclear response functions have been calculated (*cf.* figure 17) as well as the functions $G(u)$ and $H\left(d^{(3)}_{xyxy};u\right)$ (*cf.* figure 18).

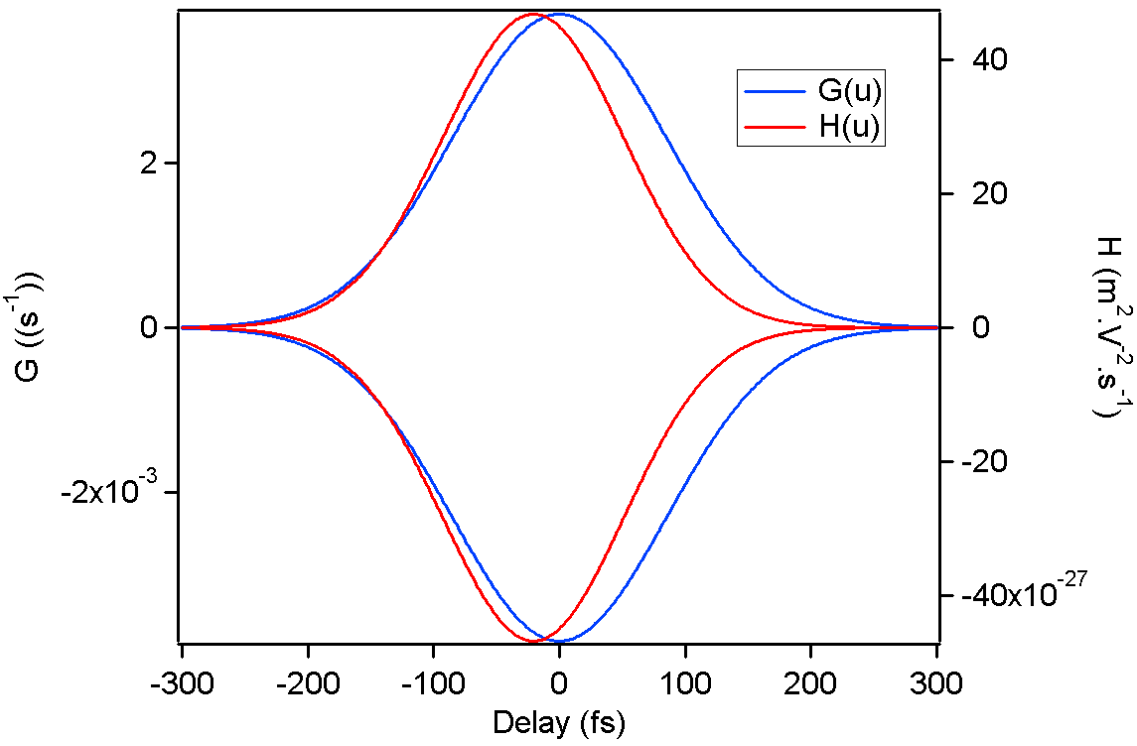

Figure 18: Functions $G(u)$ (dashed curve) and $H\left(d^{(3)}_{xyxy};u\right)$ (full curve) versus time delay between the pump and the probe pulses for a 100 fs pulse at 800 nm for fused silica.

The nuclear contribution to the total nonlinearity, $\frac{H\left(d^{(3)}_{xyxy};u=0\right)}{G(u=0)}$, has been computed and is shown in figure 19.

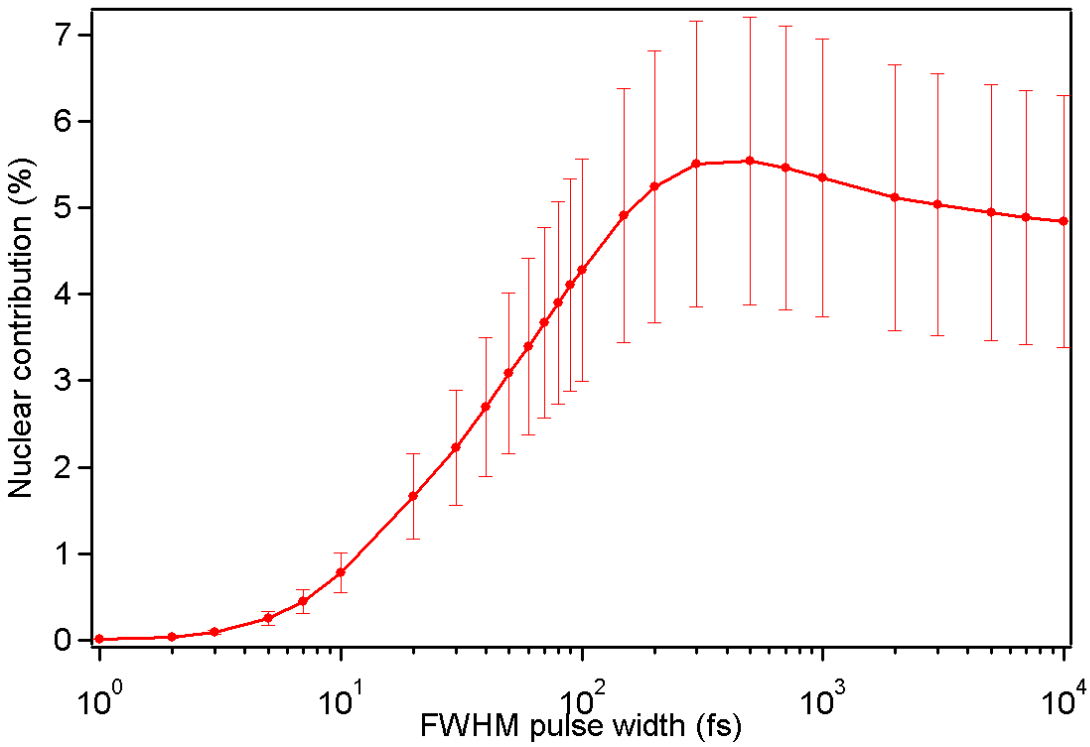

Figure 19: Evolution of the nuclear contribution to the OKE susceptibility in fused silica versus pulse width (FWHM).

The evolution of the nuclear contribution with the pulse width is similar to the electrostrictive one previously shown [Buc96], but with shorter pulses. For pulses shorter than 500 fs, the nuclear contribution increases until it reaches its maximal value at 500 fs. Afterwards, it decreases slightly to reach its long pulse limit. However, the maximum value of the nuclear contribution for fused silica (about 6%) is less than the reported values in the literature (21±3% [Hel75], 26% [Hei79], 18% [Sto92], 13±4% [Smo99]). This is due to the configuration of our OKE experiment which deals with cross-polarized pump and probe pulses. The involved tensor element of the nuclear response function in the OKE signal is $d^{(3)}_{xyxy}$, which comes directly from the depolarized Raman spectrum. Our lower value for the nuclear contribution can be explained by the fact that the depolarized Raman spectrum is much less intense than the polarized one. To date, all the measurements listed above probed the $d^{(3)}_{xxxx}$ tensor element.

6.2. Sodium-borophosphate niobium glasses

Glasses containing niobium oxide (Nb_2O_5) have been widely studied and are currently reported to exhibit high nonlinearity in sodium-borophosphate matrices containing a large amount of Nb_2O_5 [Car96] [Car97]. In particular, the increase of the third-order nonlinear optical response has been related to the atomic density of niobium in the glass. In addition, a nonlinear behavior of the nonlinear refractive index has been shown where a clear enhancement of the optical response occurs as the niobium ions are introduced in large quantities [Car96] [Car97]. The optical nonlinear response has been related to the specific three-dimensional (3D) corner-shared arrangements of NbO_6 octahedra which enables the formation of a tungsten bronze-like local structure, at high niobium oxide concentration. Lipovskii *et al.* [Lip03] have observed similar behavior of the electro-optical Kerr effect, with the successive addition of Nb_2O_5 into silicate-based glasses. This work clearly illustrates a correlation between the increase of both the Raman spectral density and the Kerr response of the materials with an increase of NbO_6 tungsten bronze "crystal motifs" within the glass structure. In this section, a sodium-borophosphate matrix, with varying Nb_2O_5 molar concentration in the glass system $(100\text{-}x)(95NaPO_3\text{-}5Na_2B_4O_7)\text{–}xNb_2O_5$, has been investigated. Table 2 lists the optical properties of these glasses.

Sodium-borophosphate glass (mol% Nb_2O_5)	9.55	19.19	28.93	38.78
λ_c (nm)	308	322	337	351
$n(\omega)$ (± 0.02)	1.53	1.59	1.73	1.81
$n(3\omega)$ (± 0.02)	1.55	1.63	1.77	1.89
THG susceptibility $\sigma^{(3)}_{xxxx}$ ($m^2.V^{-2}$) (± 30%)	6.78×10^{-22}	8.42×10^{-22}	11.63×10^{-22}	15.31×10^{-22}
OKE susceptibility $\Lambda(u=0)$ ($m^2.V^{-2}$) (± 10%)	8.68×10^{-22}	13.15×10^{-22}	17.67×10^{-22}	37.83×10^{-22}
Measured nuclear susceptibility $\Lambda(u=0)-\sigma^{(3)}_{xxxx}$ ($m^2.V^{-2}$) (± 35%)	1.90×10^{-22}	4.73×10^{-22}	6.04×10^{-22}	22.52×10^{-22}
Calculated nuclear susceptibility $\frac{H(d^{(3)}_{xyxy};u=0)}{G(u=0)}$ ($m^2.V^{-2}$) (± 10%)	1.27×10^{-22}	3.20×10^{-22}	3.53×10^{-22}	5.20×10^{-22}

Table 2: Cutoff wavelength, linear refractive indices at ω and 3ω, THG susceptibility, OKE susceptibility (from [Car97]), measured nuclear susceptibility and calculated nuclear susceptibility for different Nb_2O_5 concentrations.

The polarized (VV) and depolarized (VH) Raman experiments have been carried out from 90° spontaneous Raman scattering measurements at 514.5 nm using an experimental system allowing low frequency measurement. Raman spectra have also been measured with

longer excitation wavelengths at 632.8 nm, 752 nm and 1064 nm using a notch filter which does not allow measurement below 145 cm^{-1}. To be able to compare the Raman nuclear contributions with that obtained from THG and pump-probe experiments, the dispersion of the differential Raman scattering cross section must be taken into account. A similar evolution to that reported by Rivero *et al.* [Riv05bisbis] for glasses having an absorption edge around 350 nm, have been observed showing that no significant dispersion in the 750 nm - 1064 nm range could be measured. Moreover, no distortion of the spectra for different excitation wavelength has been observed. To obtain the Raman spectra of the studied glasses, the measured data at 514.5 nm have been rescaled to the spectra obtained at 1064 nm and compared to the reported value of silica [Hel75] after reflection, refraction and wavelength corrections [Sto73] by using a fused silica reference sample. The absolute polarized (VV) and depolarized (VH) Raman spectra are shown in figures 20 and 21, respectively.

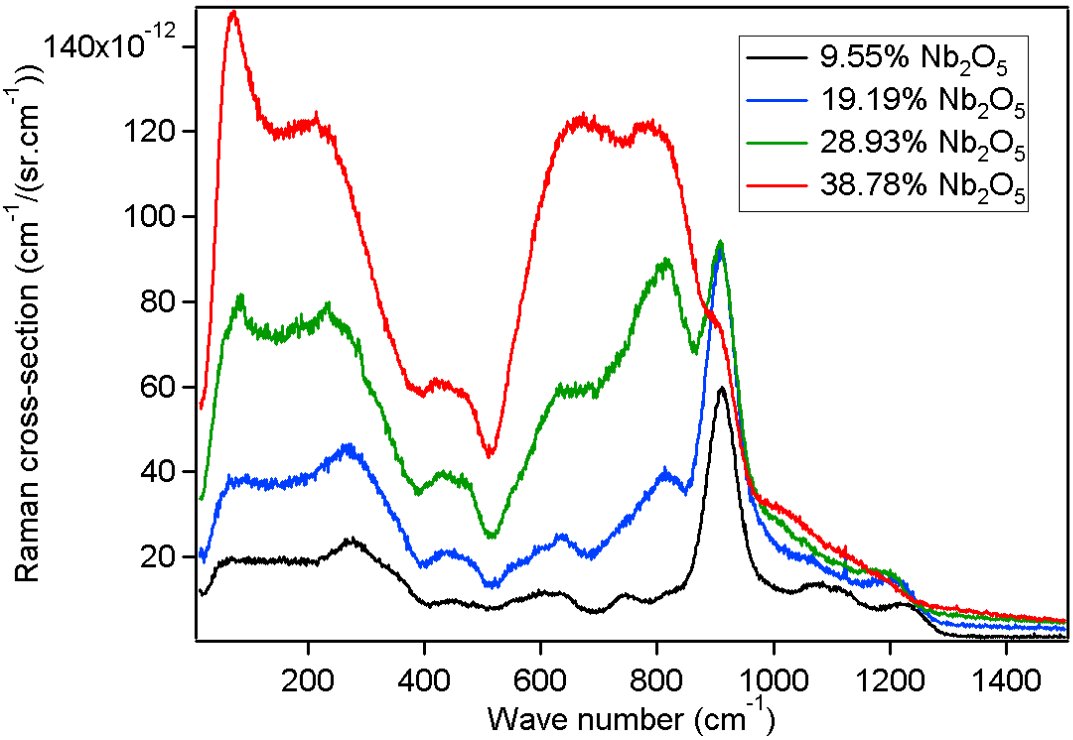

Figure 20: Absolute polarized (VV) Raman spectra of the borophosphate matrix glasses with different Nb_2O_5 concentrations at a 1064 nm excitation wavelength.

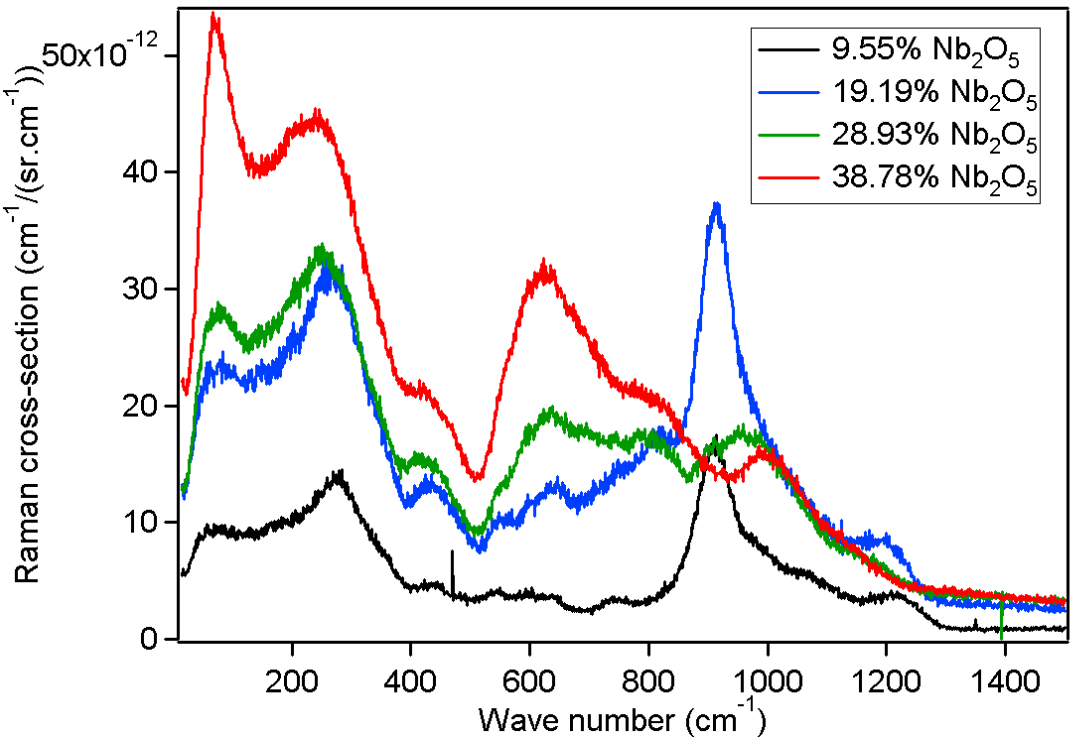

Figure 21: Absolute depolarized (VH) Raman spectra of the borophosphate matrix glasses with different Nb_2O_5 concentrations at a 1064 nm excitation wavelength.

The values of $\sigma^{(3)}_{xxxx}$ for all samples, measured with a THG microscopy setup relative to a fused silica sample, are gathered in table 2 and reported in figure 23.

The values of Λ for all samples, measured in reference [Car97], are gathered in table 2 and reported in figure 23. Since Nb_2O_5 concentrations of the glasses studied in this previous paper [Car97] were slightly different from ours, extrapolated values of the OKE susceptibility have been considered using a linear regression method.

Knowing the experimental values of Λ and $\sigma^{(3)}_{xxxx}$, one can deduce the measured nuclear susceptibility, that is $\Lambda(u=0)-\sigma^{(3)}_{xxxx}$, and thus the nuclear contribution to the OKE susceptibility. These two quantities are shown in table 2.

Finally, from the Raman spectra and following Hellwarth's model, the functions $G(u)$ and $H\left(d^{(3)}_{xyxy};u\right)$ are computed (*cf.* figure 22) and the calculated nuclear susceptibility $\frac{H\left(d^{(3)}_{xyxy};u=0\right)}{G(u=0)}$ is determined and shown in table 2.

Nevertheless, one has to consider that THG and pump-probe experiments have been carried out at different wavelengths (*i.e.* 1500 nm and 800 nm). In the transparency region of these glasses, in the visible/near IR range, the THG susceptibility follows a normal dispersion, and decreases with increasing wavelength, meaning that the susceptibility value is smaller at 800 nm than at 500 nm. A possible resonance effect might occur as the third-harmonic (at 500 nm) which is close to the electronic gap-wavelength of these glasses, leading to an over-estimation based on this measurement. This effect implies that the measured nuclear contribution might be slightly larger than shown in table 2.

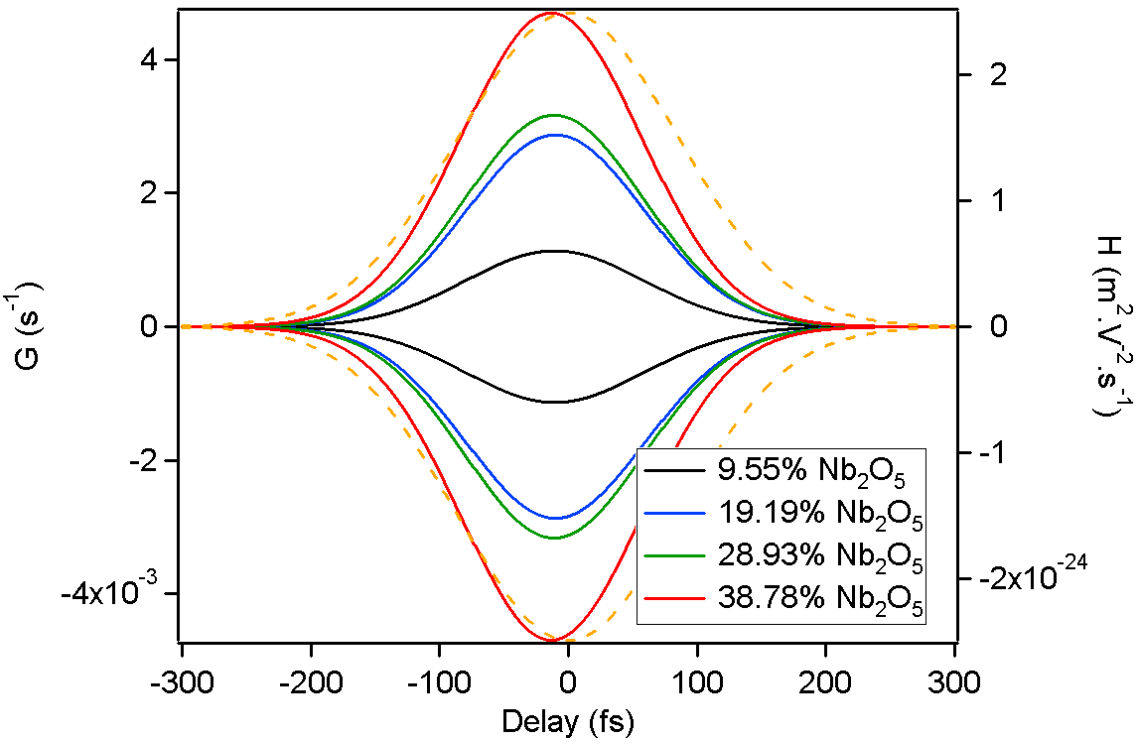

Figure 22: Functions $G(u)$ (dashed curve) and $H\left(d^{(3)}_{xyxy};u\right)$ (full curves) versus time delay between the pump and the probe pulses for a 100 fs pulse at 800 nm for different Nb_2O_5 concentrations.

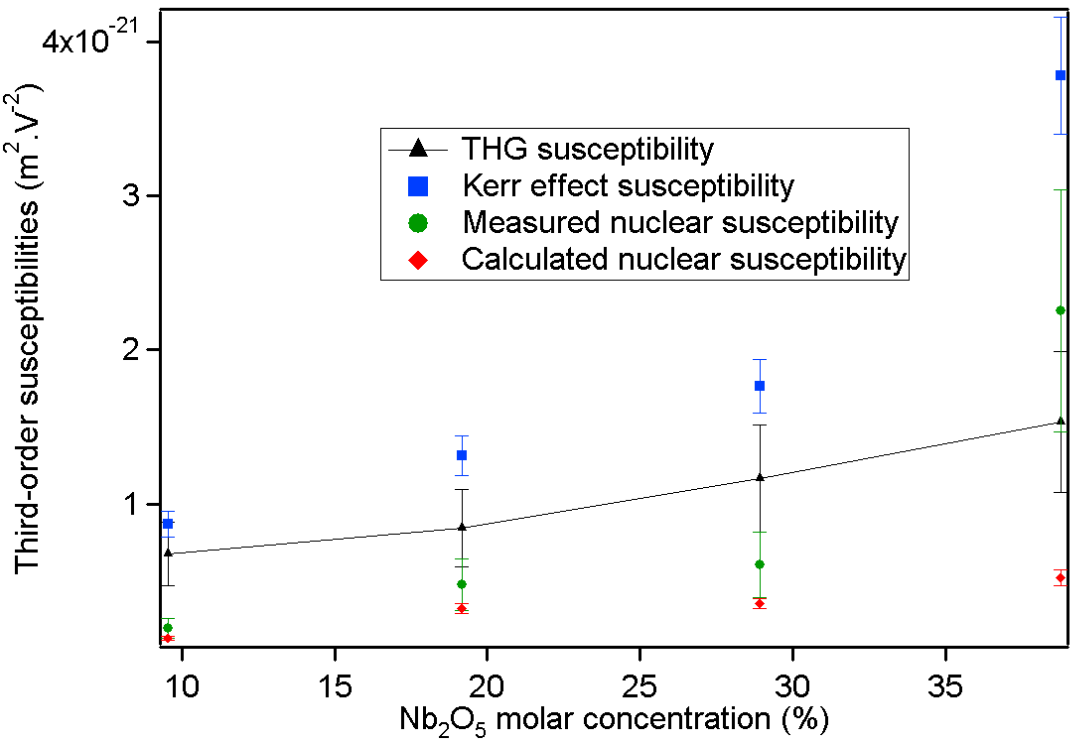

Figure 23: THG susceptibility $\{\sigma^{(3)}_{xxxx}\}$, OKE susceptibility $\{\Lambda(u=0)\}$ and measured nuclear susceptibility $\{\Lambda(u=0)-\sigma^{(3)}_{xxxx}\}$ versus Nb_2O_5 molar concentration.

For a 100 fs optical pulse at 800 nm (*i.e.* 140 cm^{-1} bandwidth), it appears that the mode at 230 cm^{-1} contributes mostly to the nuclear susceptibility (about 75% of the total nuclear susceptibility) whereas the modes above 500 cm^{-1} have a negligible influence. To participate in the nuclear nonlinearity, the vibrational modes must present both a low wave number and a large bandwidth, *i.e.* a low oscillation frequency and a high damping in the time domain, so that the convolution of the nuclear response function with the optical pulse is maximal.

Calculation and experimental results are in agreement to within uncertainties of the measurements as long as the Nb_2O_5 concentration is less than 28.93 mol%. For the 38.78 mol% Nb_2O_5 concentration, a significant nuclear fraction to the nonlinear refractive index has been measured (~ 60%). The results (~ 22-36%) obtained for low niobium oxide content are in accordance with data previously reported for silicate based materials by Hellwarth *et al.* [Hel75]. The evolution of the nonlinearity for low niobium oxide content is driven by the

electronic contribution. The results obtained validate the model proposed for summation of Nb-O bond electronic contribution to the nonlinearity previously proposed [Car97]. For high Nb^{5+} ions concentration, the measured nuclear fraction to the nonlinear refractive index is the highest reported to date in inorganic glasses. Moreover, discrepancies between calculated and measured nuclear contributions deduced from THG and OKE measurements seem to indicate that the present Raman measurements do not entirely take into account the true nuclear contribution.

The evolution of the glass structure with increasing Nb_2O_5 concentration in borophosphate glasses has been investigated [Car96] [Car97]. The introduction of Nb_2O_5 in small quantities gives rise to the formation of hyperpolarizable "isolated" distorted NbO_6 octahedra with a characteristic Raman signature around 900 cm^{-1}. As the Nb_2O_5 concentration increases, corner shared NbO_6 octahedra are formed and progressively, a one-dimensional Nb-O-Nb framework corresponding to chains of octahedral can be distinguished with a Raman band around 830 cm^{-1}. For high Nb_2O_5 concentration, a two dimensional and finally three-dimensional framework is created. This local structure has a strong similarity with crystalline structures such as $Ba_2NaNb_5O_{15}$, $NaNb_3O_8$ or $NaNbO_3$ involving NbO_6 octahedra sharing a common corner unit.

The formation of the 3D octahedral structure within the glass is correlated to the Raman band around 250-300 cm^{-1} in the low frequency domain increasing in intensity and a new sharp vibration at 70 cm^{-1}. These vibrations are strongly related to the vibration around 650 cm^{-1}. Recently, Malakho *et al.* [Mal05] have shown that in this glass system, the first crystallization phase observed is $NaNb_3O_8$, which can be compared to $NaNbO_3$ or $Ba_2NaNb_5O_{15}$ crystalline structures. In these crystalline phases ($KNbO_3$, $NaNbO_3$ or $Ba_2NaNb_5O_{15}$), vibrations around 650 cm^{-1}, 250-300 cm^{-1} and 50-70 cm^{-1} are also present [Bou80] [She95] [Bou03]. Numerous articles have mentioned correlations between the

intensity of the low phonon bands and the phase transition observed in niobate crystals leading to ferroelectricity [Bou80] [She95]. In glasses, such effects cannot occur due to their disordered structure but nevertheless, the presence of similar vibrations to those observed in the crystalline phases, and particularly the band around 250 cm^{-1}, could be related to collective motion of 3D associated NbO_6 octahedra. Significant nuclear contribution to the nonlinear refractive index appears for Nb_2O_5 molar concentration above 28.93%, which corresponds to the existence of NbO_6 tungsten bronze structure (TBS) and to the largest intensities of the vibrations around 650 cm^{-1}, 250-300 cm^{-1} and 50-70 cm^{-1}. The calculation of the nuclear contribution thus indicates (for a pulse of 100 fs), that the major contribution to the nonlinear refractive index is associated to the vibration located around 250-300 cm^{-1}. Clear assignment of NbO_6 collective motion in the glass leading to such vibration would be of importance to understand how local structure can significantly affect the nonlinear response.

The reason why Hellwarth's model no longer stands in these glasses for Nb_2O_5 concentrations higher than 28.93% is still under investigation. Further experiments will be performed to understand why the entire nuclear information is not contained in the Raman spectra and to identify other eventual vibrational modes unrevealed by Raman spectroscopy.

PART B: LASER STRUCTURING

CHAPTER SEVEN: LASER-MATERIAL INTERACTION

Laser-material interaction is a field that has been extensively studied during the past decade. The understanding of the involved physical phenomena and their associated characteristic times is of particular importance [Sch01] [Stu96] [Mao04] [Ams08] [Gat08]. Even though the picture is far to be clear, it is admitted in the community that, when a high irradiance laser pulse is incident onto a material, some of the following events occur (*cf.* figure 24):

- After 1 femtosecond, the electrons absorb the laser photons by photo-ionization.
- After 50 femtoseconds, if the generated photoelectrons are sufficient in number and in energy, avalanche ionization is initiated.
- After 100 femtoseconds, the electrons get thermalized. They reach a Fermi-Dirac energy distribution after having absorbed the laser energy.
- After 1 picosecond, the electrons cool and they transfer their energy to the surrounding neutral atoms and ions (lattice).
- After 10 picoseconds, the heat diffuses inside the material. The phonons reach a Bose-Einstein energy distribution.
- After 100 picoseconds, the material melts if the thermal energy is sufficiently higher than the bond strength.
- After 1 nanosecond, resolidification and structural changes occur.

The first three processes correspond to the absorption of the laser energy by the material. The three following effects translate the transformation of the absorbed laser energy into thermodynamic processes (thermal diffusion, melting) at the macroscopic scale. The last event involves photo-chemical processes leading to structural changes (explosion,

resolidification, chemical bond breakings) at the microscopic scale, or even at the nanoscopic scale, as it will be shown later.

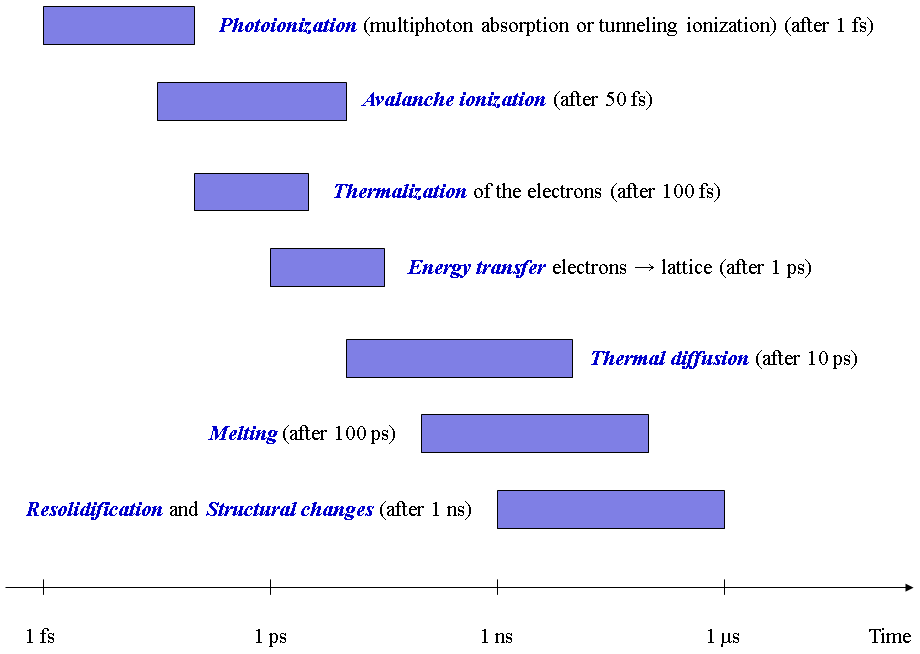

Figure 24: Timescale of the physical phenomena involved in laser-material interaction.

Thus, the picosecond, corresponding to the electrons-network relaxation, gives an order of magnitude of the limit between the thermal and non-thermal phenomena. For this particular reason, structuring materials with femtosecond pulses has been preferred to longer pulse regimes to prevent thermal effects to occur. Moreover, the energy deposited by a femtosecond pulse is confined inside the focal volume because of nonlinear absorption and absence of linear absorption and thermal diffusion. This results in high spatial precision for local modification as illustrated in figure 25.

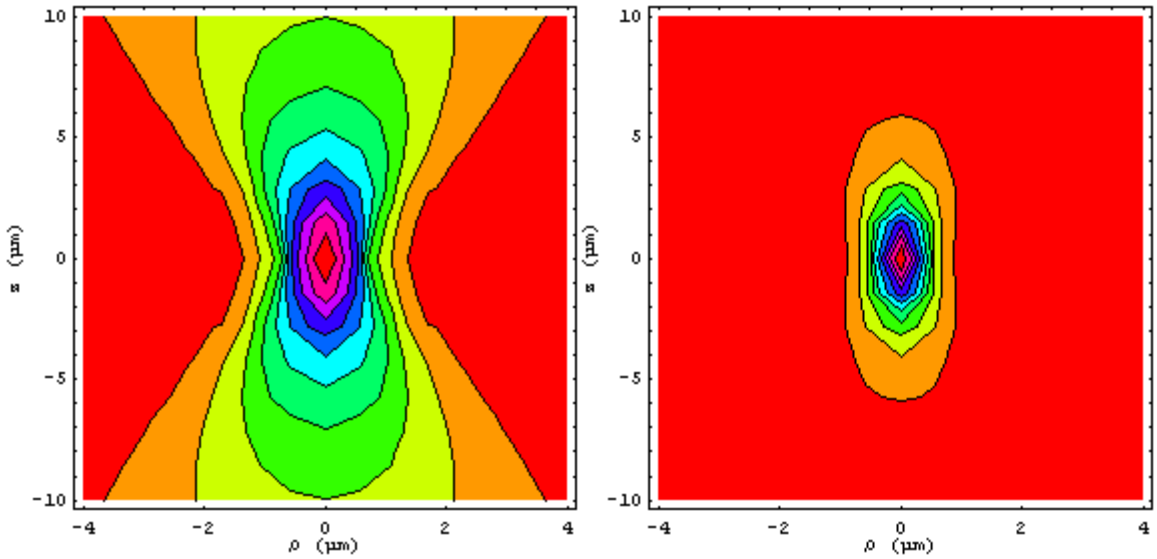

Figure 25: Linear absorption (on the left) and three-photon absorption (on the right) of a Gaussian beam focused with a 0.55-NA microscope objective inside a random material.

Traditionally, the dynamic of laser-material interaction is divided into three steps. First, photo-ionization generates a population of free electrons in the conduction band. Second, these free electrons increase their kinetic energy by absorbing new laser photons (free carrier absorption). Third, when the electron energy exceeds the band gap energy, it can promote another electron initially in the valence band into the conduction band by collision (impact ionization) leading to avalanche ionization. However, for short pulses (less than 50 fs), avalanche ionization does not stand and another process has been proposed to participate in the laser-material interaction, namely multiphoton “forest fires” ionization. An overview of each of the ionization phenomena is given in this chapter, as well as the different response regimes experienced by the material, depending on the irradiation conditions.

7.1. Multiphoton and tunneling ionizations

Multiphoton and tunneling ionizations have been theoretically described by Keldysh in his well-known paper [Kel65]. Multiphoton ionization of an atom corresponds to the simultaneous absorption of several photons which cumulated energy exceeds the ionization

potential of the electron energy level. It is more probable if the number of required photons is low; consequently, it is favored for the short wavelengths which necessitate less photons to reach a given energy. The number of generated free electrons is given by

$$\frac{dN}{dt} = \sigma_n I^n \tag{B.7.1}$$

where n is the number of photons involved in multiphoton absorption, σ_n the n^{th}-photon absorption coefficient and I the laser irradiance.

Tunneling ionization takes place when the incident electric field is sufficiently important to distort the potential barriers which maintain the electron in the field of the nucleus of an atom. The electron is then ejected. Because of the high required irradiance, tunneling ionization can only occur in the femtosecond regime.

The interaction between multiphoton and tunneling ionizations is complex and is generally quantified through the Keldysh parameter, given by [Kel65]

$$\gamma = \frac{\omega}{e}\sqrt{\frac{m_e c n_0 \varepsilon_0 E_g}{I}} \tag{B.7.2}$$

where ω is the laser angular frequency, m_e and e the mass and the charge of the electron, c the speed of light in vacuum, n_0 and E_g the refractive index and the band gap energy of the material and ε_0 the dielectric permittivity of vacuum. Figure 26 illustrates the competition between the two types of photo-ionization. For $\gamma < 1.5$ (*i.e.* for high irradiances), tunneling ionization dominates whereas for $\gamma > 1.5$ (*i.e.* for low irradiances), multiphoton ionization dominates.

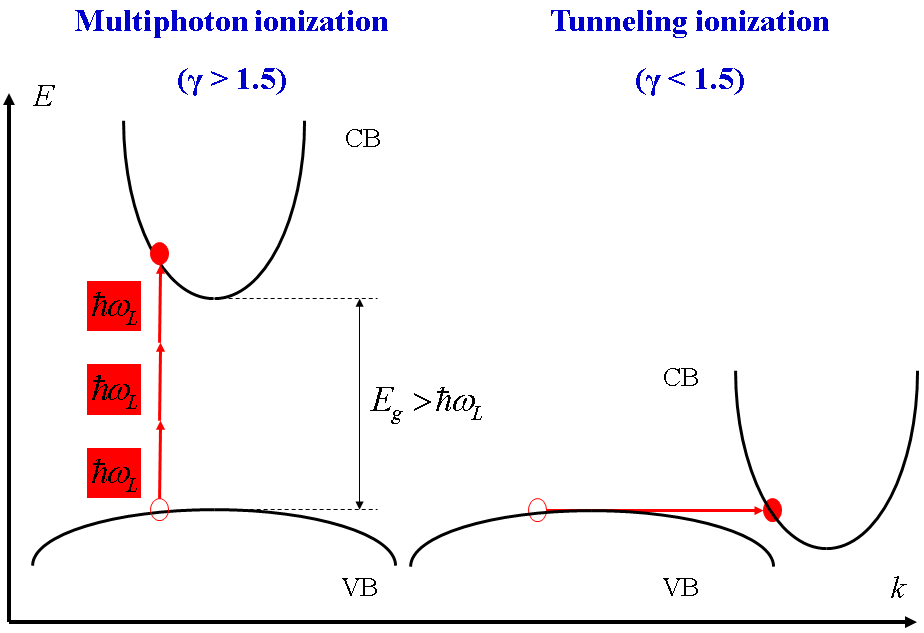

Figure 26: Schematic band diagram of multiphoton and tunneling ionizations of an electron originally in the valence band. CB and VB stand for conduction band and valence band, respectively.

7.2. Avalanche ionization

Avalanche ionization is initiated by an electron which kinetic energy is sufficient to ionize by collision a neighboring atom. By inverse Bremsstrahlung, the new free electron will consecutively gain kinetic energy and can ionize similarly a neighboring atom (*cf.* figure 27). The number of generated free electrons is given by

$$\frac{dN}{dt} = \alpha I N \qquad \text{(B.7.3)}$$

where α is the avalanche ionization coefficient, I the irradiance of the laser and N the free electron density.

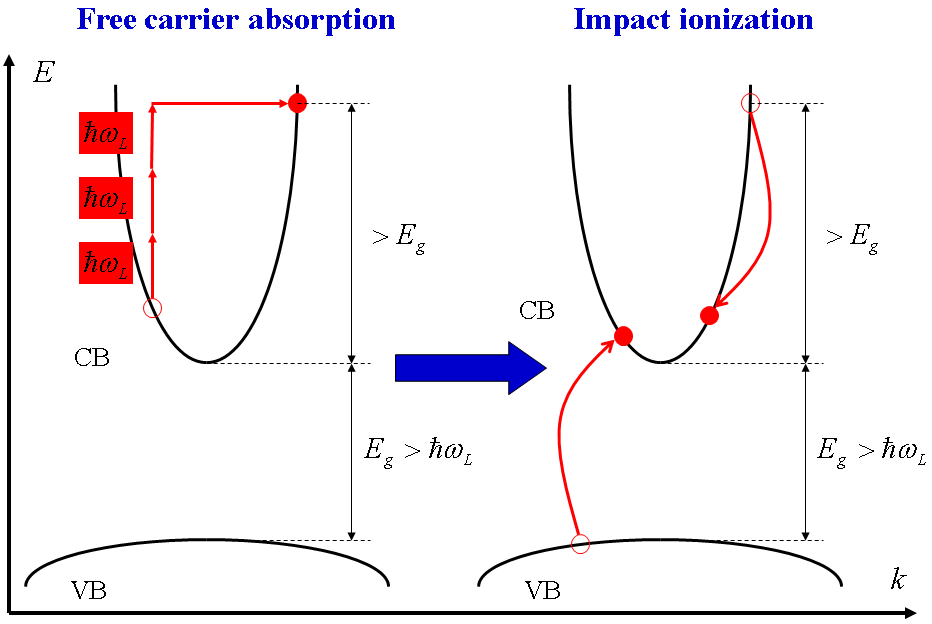

Figure 27: Schematic band diagram of free carrier absorption and impact ionization processes leading to avalanche ionization. CB and VB stand for conduction band and valence band, respectively.

The characteristic time for avalanche ionization to occur is on the order of 30-50 fs [Gai05]. Therefore, for avalanche ionization to participate in laser-induced modifications, the pulse duration must be longer than 50 fs. A question then comes: what replaces avalanche ionization when pulses are shorter than 50 fs?

7.3. Multiphoton "forest fires" ionization

Mutiphoton "forest fires" ionization has been proposed as a substitute to avalanche ionization when short pulses are involved. This process takes place for intermediate values of the Keldysh parameter ($\gamma \approx 1.5$). When an electron is localized on a nucleus, the fast removal of this electron leaves an uncompensated positive charge behind, namely a hole. The creation of a hole enhances the creation of new holes at the adjacent sites, igniting an avalanche-like ("forest fires") ionization in clusters or molecules. These latter are the starting point for the

creation of nanoscale droplets of singly ionized plasma. These nanostructures expand similar to forest fires and can have fractal dimension (*cf.* figure 28) [Gai04] [Gai05] [Ray05].

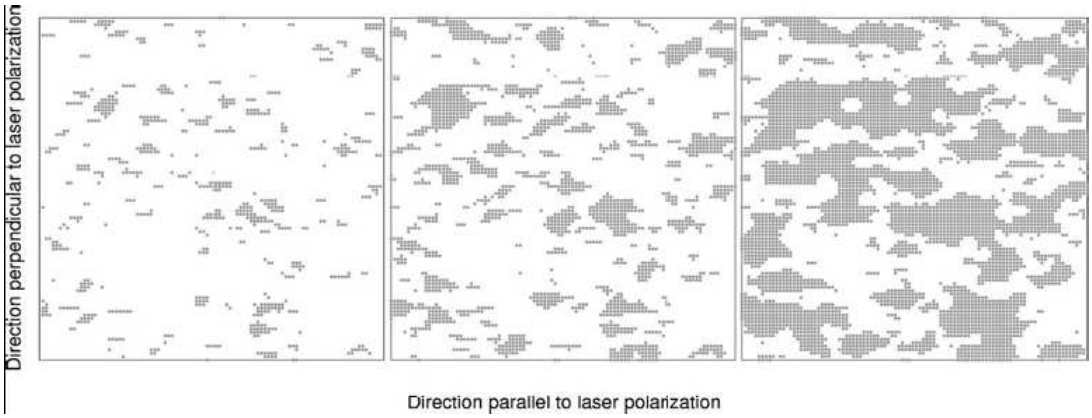

Figure 28: Two-dimensional "forest fire" simulation of Argon cluster surface. Plots from left to right correspond to times at which ionized regions make up 10%, 25% and 50% of the lattice area [Gai04].

7.4. Material response mechanisms

In the previous section, it was shown that the absorption of the laser energy by the electrons and its transfer to the lattice result in modifications of chemical bonds or, if the energy is high enough, to their breaking. Depending on the irradiation conditions, the material response to a femtosecond pulse train can be decomposed into three regimes determined by increasing the pulse energy, namely *isotropic refractive index change*, *anisotropic refractive index change* and *void formation*. The transition threshold between the isotropic and anisotropic regimes is difficult to determine since it depends a lot on the irradiation conditions (pulse energy, repetition rate, numerical aperture, exposure time or translation speed). For example, Sudrie et al. found the transition threshold for fused silica at an irradiance of about 100 $TW.cm^{-2}$ and 4×10^{3} pulses [Sud01].

7.4.1. Type I: Isotropic refractive index change

In this regime, the material response consists in an isotropic refractive index change, which can be either positive (like in fused silica [Hir98]) or negative (like in phosphate glasses [Cha03]). The refractive index change increases with the pulse energy. The structural changes are caused by fusion and non-uniform solidification. This regime is typically used for waveguides and couplers fabrication.

7.4.2. Type II: Anisotropic refractive index change

In this regime, the material response consists in a "nanograting" structure with a periodic modulation of the refractive index [Shi03]. The refractive index change alternates between positive and negative values [Bri04]. The explanation of this phenomenon is not well established in the community [Shi03] [Bha06]. This regime is typically used for polarization control devices and microreflectors. More details about this regime will be given in the next chapter.

7.4.3. Type III: Void formation

In this regime, a void is created close to the focus of the beam, due to the explosive expansion of the hot electrons and ions. The void presents a low-density with a negative refractive index change, embedded by a denser shell with a positive refractive index [Gle96]. This regime is typically used for optical data storage devices and photonic crystals fabrication.

CHAPTER EIGHT: STRUCTURING OF FUSED SILICA

8.1. At the wavelength scale

In 2005, Zoubir *et al.* wrote waveguide structures inside fused silica and measured their linear and nonlinear optical properties [Zou05]. The authors reported an increase in the linear refractive index $\Delta n/n$ on the order of 0.3% (from numerical aperture measurements of the exiting guided beam) and a decrease in the nonlinear cubic susceptibility $\Delta\chi^{(3)}/\chi^{(3)}$ on the order of 60% [from THG microscopy and self-phase modulation measurements]. This contradicting evolution of the linear and nonlinear optical properties, *i.e.* increasing the linear refractive index while decreasing the nonlinear one, is unexpected and difficult to understand. The fact that the light is guided inside the waveguide imposes a positive refractive index change; so the increasing trend of this property is not questionable. On the other hand, Szameit et *al.* [Sza05] and Blömer *et al.* [Blo06] measured the changes in the nonlinear refractive index by analyzing the self-phase modulation of the propagating beam inside femtosecond laser-written waveguides. They found too a decrease of the nonlinear refractive index between 15% and 75%, depending on the irradiation conditions, confirming thus the decreasing evolution of this property.

In 2006, a comparative study on three commercially available fused silica samples possessing different levels of initial impurities content, showed a correlation between the laser-induced structural modifications and the different spectroscopic signatures [Zou06]. Nevertheless, the link between the changes in the refractive index and the third-order susceptibility and the spectroscopic signatures was not investigated.

In this section, three fused silica samples possessing different impurity levels and exposed to a femtosecond laser have been studied. The laser-induced defects have been

identified from absorption, luminescence and Raman spectroscopy. The changes in the linear and the nonlinear optical properties have been measured from Kramers-Krönig calculations and THG microscopy experiments. In parallel, discussions about the link between the measurements and the structural modifications have been conducted. Several hypotheses are discussed to explain the contradicting evolution of the linear and nonlinear optical properties.

8.1.1. Sample description and irradiation conditions

One mm-thick fused silica samples commercially available from Heraeus (Herasil 2, Suprasil 312 and Infrasil 302) were used in this study. Their corresponding absorption spectra are presented in figure 29. Herasil and Suprasil possess a low concentration in oxygen vacancies (Al), which confers good transparency in the ultraviolet (UV), but a high OH^--content responsible for the high absorption band around 2700 nm. By contrast, Infrasil shows no such band in the infrared (IR), but presents high absorption in the UV. Table 3 lists the linear and nonlinear optical properties and impurity (OH^- and Al) levels of the samples under investigation, prior irradiation.

Fused silica sample	Herasil 2	Suprasil 312	Infrasil 302
Density ($g.cm^{-3}$)	2.203	2.201	2.203
Al impurity level (ppm)	10	≤ 0.01	20
OH^- impurity level (ppm)	150	200	≤ 8
λ_c (nm)	211	170	209
n (656.3 nm)	1.45646	1.45637	1.45646
n (587.6 nm)	1.45856	1.45846	1.45856
$\chi^{(3)}/\chi^{(3)}_{Herasil}$ (%)	100	98 ± 4	96 ± 4
$\Delta\chi^{(3)}/\chi^{(3)}$ (%)	-23 ± 4	-17 ± 4	-24 ± 4

Table 3: Density, Al and OH^- impurity levels, cutoff wavelength, refractive indices at 656.3 and 587.6 nm and third-order susceptibility relative to Herasil for the unexposed samples and relative change in the third-order susceptibility for the 5 µJ-exposed samples.

The three bulk glass samples have been exposed to a NIR Ti:Sapphire regenerative amplifier (Spitfire system from Spectra Physics) which delivers 1 mJ, 1 kHz, 100 fs pulses at a wavelength of 800 nm. The beam was focused with a 10 cm focal length lens. The translation speed was 1 $mm.s^{-1}$, the number of pulses in a given spot area was about 25 and the pulse energies were 5 and 20 µJ. The irradiated areas consist in 1 mm × 1 mm square structures. They are approximately 400 µm below the surface and 200-µm-thick.

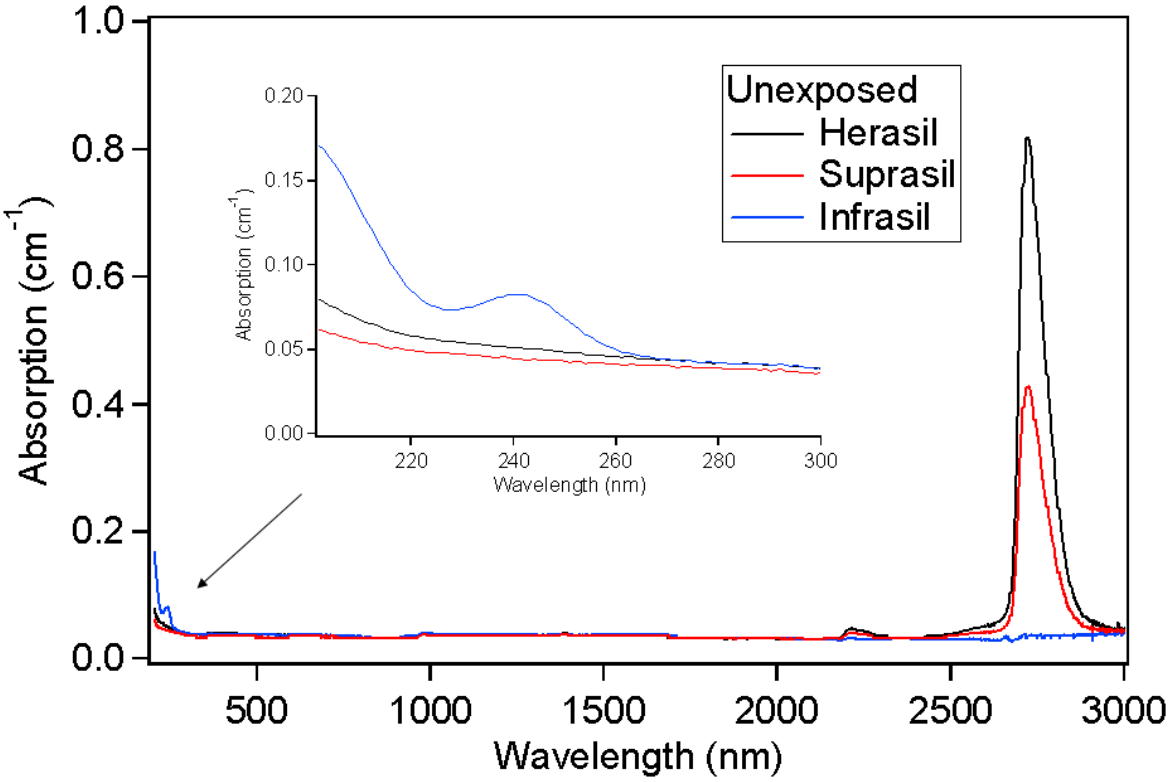

Figure 29: Absorption spectra and UV region expanded (inset) for the three unexposed fused silica samples.

8.1.2. Spectroscopic investigations

8.1.2.1. Absorption spectroscopy

The visible-UV change in the absorption coefficient was determined by measuring the absorption spectrum through the irradiated region and subtracting it from the absorption

spectrum measured on the unexposed region, using a Cary 500 spectrophotometer (Varian). The absorption change spectra are shown in figure 30. No significant absorption bands are observed for Suprasil and Herasil samples. Only for Infrasil, two bands appear at around 200 nm and at 240 nm. These absorption bands are related to impurities such as germanium, which are present in the raw materials used for fabrication of Infrasil. In all samples, two absorption bands are observably induced by the irradiation process. The peak centered at around 215 nm is attributed to Si *E'* centers, an unpaired electron spin in a silicon atom bound to three oxygen atoms (≡Si •) related to an oxygen vacancy in the fused silica network. The peak at around 250 nm can be attributed to non-bridging oxygen hole centers (NBOHCs) or oxygen-deficient centers (ODCs) associated generally to two fold coordinated silicon diamagnetic centers [Sku98] [Zou06] (=Si••). The absorption change spectra also show the presence of peaks below 190 nm, which can be assigned to ODCs [Sku98].

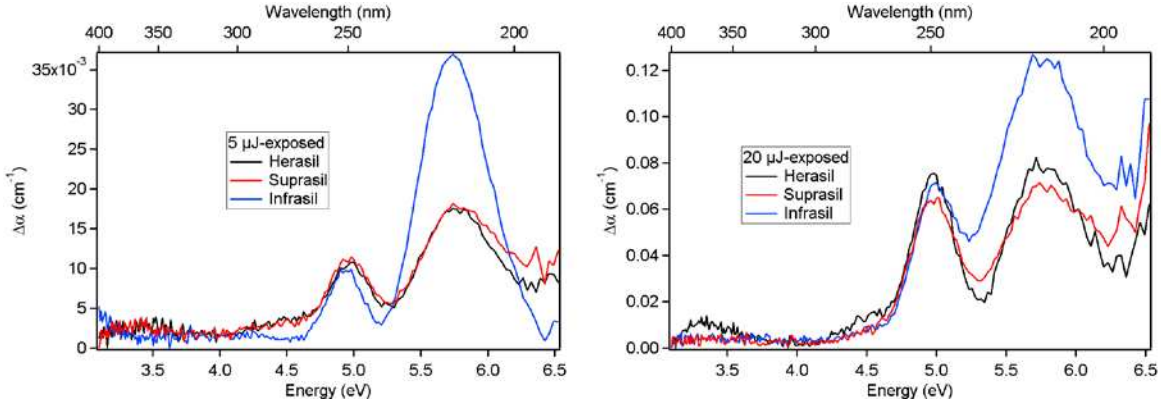

Figure 30: Absorption change spectra for the three 5 µJ- and 20 µJ-exposed fused silica samples.

8.1.2.2. Luminescence spectroscopy

Because of the 185 nm detection limit of the Cary 500 spectrophotometer due to air-contained oxygen absorption, all the color center signatures could not be identified. To overcome this problem, luminescence spectroscopy has been performed in complement to absorption spectroscopy. The instrument is from Edinburgh Instruments Ltd. and is equipped

with a 450 W Xenon lamp, and a double monochromator in both the excitation and detection arms. The luminescence spectra (*cf.* figure 31), obtained with a 248 nm excitation, show for Suprasil and Herasil emission bands at 360 nm and at 460 nm prior laser exposure. The band at around 360 nm could not be clearly identified. Only few publications have reported such emission band in Si-SiO_2 nanoclusters [Mov95]. The band at 460 nm corresponds to well known ODCs (II) [Sak06] [Sku98]. For Infrasil, the emission band at around 390 nm is assigned to impurity centers. After laser exposure, modifications are visible for the samples exposed at 5 µJ and at 20 µJ. For 5 µJ exposure, the band at 650 nm attributed to the presence of NBOHCs is visible for Herasil and Suprasil. For 20 µJ exposure, this last emission band is visible for all the samples and the band at 460 nm, attributed to the ODCs (II), is rising as compared to the other emission features [Zou06] [Rei06] [Sku98].

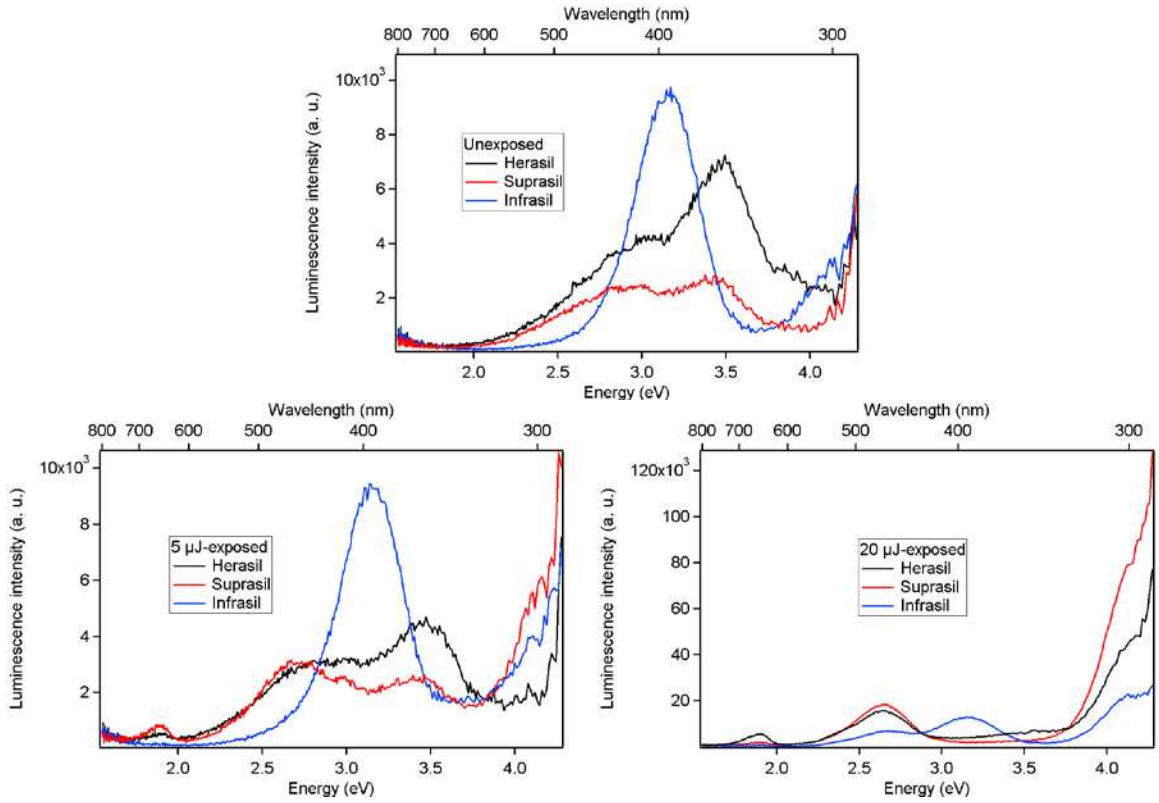

Figure 31: Luminescence spectra for the three unexposed, 5 µJ- and 20 µJ-exposed fused silica samples at a 248 nm excitation wavelength.

8.1.2.3. Raman spectroscopy

The spontaneous Raman spectra of the unexposed and exposed samples (*cf.* figure 32) were obtained using a confocal micro-Raman system (LabRAM HR from HORIBA Jobin Yvon). The incoming 514.5 nm laser excitation was focused inside the bulk of the sample, at the unexposed and exposed defect areas, respectively, via a 100× microscope objective, with a spatial resolution of about 2 µm. The backscattered light was collected and spectrally analyzed with a spectrometer and a CCD detector, with a typical resolution of about 6 cm^{-1}. The Rayleigh line was suppressed with a holographic notch filter. All Raman spectra have been normalized to the intensity of the band at 440 cm^{-1}.

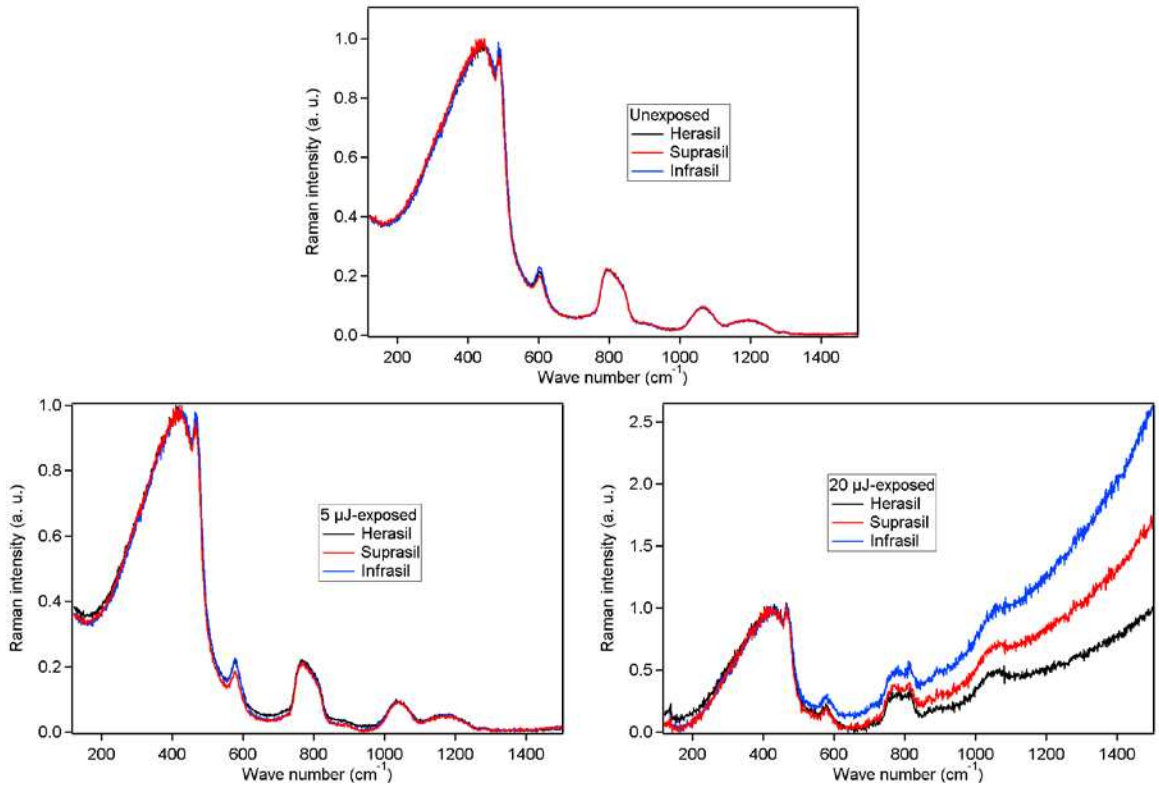

Figure 32: Raman spectra for the three unexposed, 5 µJ- and 20 µJ-exposed fused silica samples at a 514.5 nm excitation wavelength.

The main feature of the spectrum of fused silica is the broad band centered at around 440 cm^{-1}, attributed to the Si-O-Si bond rocking and bending in SiO_4 tetrahedra [Gal83]. The two smaller bands at 490 cm^{-1} (*D*1) and 606 cm^{-1} (*D*2) have been attributed to three- and

four-member siloxane rings, respectively, in the silica network [Pas98]. The increase of the Raman intensity with the wave numbers for the 20 µJ-exposed samples is due to the fluorescence scattered by the defects, superimposed in the Raman signal. The comparison of the spectra between pristine and exposed samples reveals two principle trends:

- The amplitude of both defect lines $D1$ and $D2$ increases slightly, which is related to the disruption of the continuous random network of SiO_4 tetrahedra and to a densification of the material [Zou06] [Rei06] [Sal06].

- The width of the main band at 440 cm^{-1} decreases, which is related to a decrease in the Si-O-Si bond angle and width of their angular dispersion [Zou06] [Rei06] [Sal06].

8.1.3. Calculation of the refractive index change

From the absorption change spectra, the refractive index change can be predicted from the Kramers-Krönig relation

$$\Delta n(\omega) = \frac{c}{\pi} \int_0^{+\infty} \frac{\Delta\alpha(s)}{s^2 - \omega^2} ds \qquad \text{(B.8.1)}$$

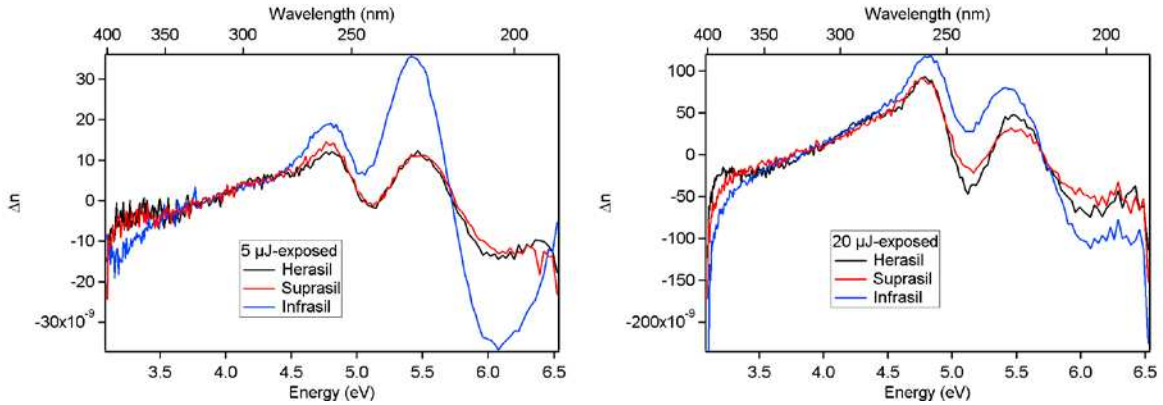

Figure 33: Refractive index change spectra obtained from the absorption spectra with a Kramers-Krönig transform for the three 5 µJ- and 20 µJ-exposed fused silica samples.

The numerical calculation shows that the color centers created after irradiation have very little contribution to the change in the refractive index (*cf.* figure 33). Indeed, the maximum computed change in the refractive index is on the order of 10^{-8}, a value that is

insufficient to explain the guiding of the light at 633 nm effectively observed by Zoubir *et al.* [Zou05]. Nevertheless, these results have to be put into perspective. The absorption spectra change calculations have been carried out on a narrow spectral range (from 190 to 400 nm). The numerical computation takes only into account this spectral range so that other probable absorption bands as well as an eventual red-shift of the cutoff wavelengths are ignored. Thus, this calculation gives a qualitative but not quantitative idea about the influence of the color centers generated after irradiation. Other absorption bands due to color centers would appear deeper in the UV region, at wavelengths lower than 190 nm, and could explain, if they are sufficiently intense, the increase of the refractive index in the visible region. However, simulations reveal that the intensity of these bands must be too strong for this too occur. This finding allows us to conclude that the color centers are not responsible for refractive index modifications and confirms previous work performed by Will *et al.* [Wil02] and Streltsov and Borrelli [Str02] who showed that the refractive index change remains, even after having annealed the color centers by a thermal treatment. Hence, it is more likely that the refractive index change is mainly due to a densification of the material, as revealed by the increasing of the amplitude of both lines *D*1 and *D*2 in the Raman spectra [Zou06] [Rei06] [Sal06].

8.1.4. Measurement of the third-order susceptibility change

The third-order susceptibility change has been measured by THG microscopy. This technique is based on the analysis of the third-harmonic beam generated at an interface between two media presenting different optical properties. It is sensitive both to Δn and $\Delta\chi^{(3)}$, but in a much more important manner to the latter quantity. A complete theoretical and experimental description of this technique is given in [Roy06].

The experiment was carried out with a Yb:KGW laser source (t-Pulse from Amplitude Systemes) which delivers 20 nJ, 50 MHz, 200 fs pulses at a wavelength of 1030 nm. The laser

beam was focused with a microscope objective (*NA* = 0.75, *working distance* = 500 µm). The third-harmonic beam was collected with a condenser (*NA* = 0.4, *working distance* = 3 cm), filtered from the fundamental wavelength using an interference filter ($\lambda_0 = 343\,\text{nm}$, $\Delta\lambda = 40\,\text{nm}$) and measured with a photomultiplier tube (PMT, Hamamatsu R5700). The photocurrent from the PMT is amplified, digitized and sent to a computer for acquisition. A typical z-scan of the third-harmonic signal emitted by the samples is shown in figure 34. The first peak corresponds to the air/bulk interface and the second peak corresponds to the bulk/defect interface. The other interfaces could not be reached because of the limited working distance of the microscope objective (500 µm). No THG data could be obtained for the 20 µJ-exposure. This high dose corresponds to the regime of visible optical damage in the form of scattering centers in the volume of the samples, and hence most of the third-harmonic light was scattered in all directions.

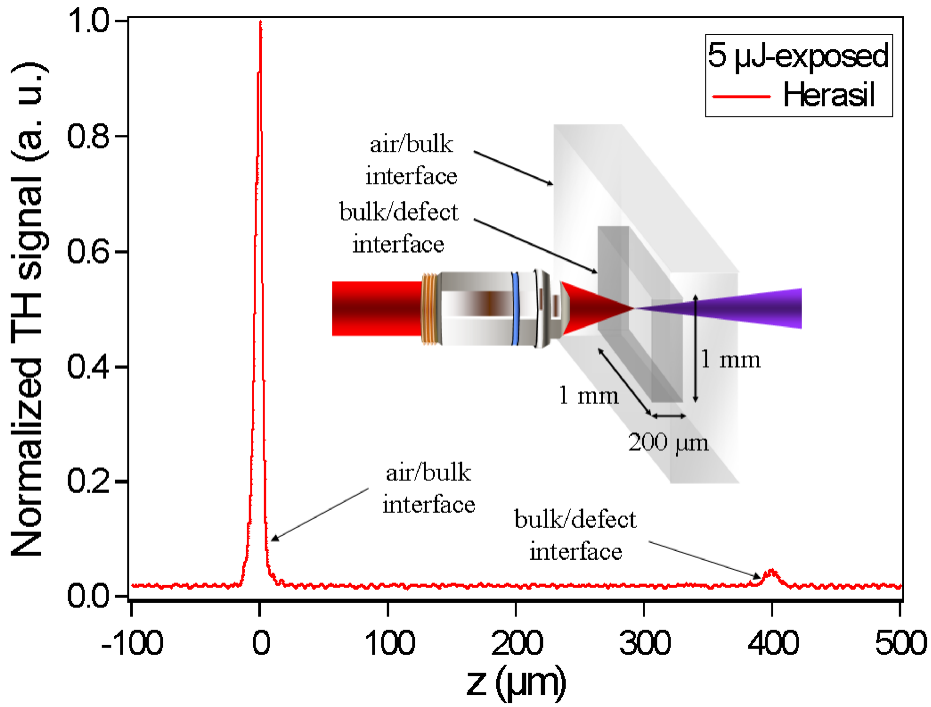

Figure 34: Evolution of the normalized third-harmonic signal versus the z-position for the 5 µJ-exposed Herasil sample. The first peak corresponds to the air/ silica interface and the second peak corresponds to the bulk/defect interface. The other interfaces could not be reached because of the limited working distance of the microscope objective (500 µm).

$\Delta\chi^{(3)}$ cannot directly be read from this z-scan. The procedure to obtain the measurement is the following. The third-harmonic irradiances generated at the interfaces air/bulk and bulk/defect, respectively, are given by [Roy06]

$$I_{3\omega,air/bulk} \approx \left(\frac{3\omega}{4\varepsilon_0 c^2}\right)^2 I_\omega^3 \frac{n_{\omega,SiO_2}^3}{n_{3\omega,SiO_2}} \times \left| J_{SiO_2}\left(\Delta k_{SiO_2};0;400\right)\chi_{SiO_2}^{(3)} + J_{def}\left(\Delta k_{def};400;600\right)\chi_{def}^{(3)} + J_{SiO_2}\left(\Delta k_{SiO_2};600;1000\right)\chi_{SiO_2}^{(3)} \right|^2$$

(B.8.2)

$$I_{3\omega,bulk/def} \approx \left(\frac{3\omega}{4\varepsilon_0 c^2}\right)^2 I_\omega^3 \frac{n_{\omega,def}^3}{n_{3\omega,def}} \times \left| J_{SiO_2}\left(\Delta k_{SiO_2};-400;0\right)\chi_{SiO_2}^{(3)} + J_{def}\left(\Delta k_{def};0;200\right)\chi_{def}^{(3)} + J_{SiO_2}\left(\Delta k_{SiO_2};200;600\right)\chi_{SiO_2}^{(3)} \right|^2$$

(B.8.3)

where the *SiO2* subscript refers to bulk fused silica and the *def* subscript alludes to the defect. I_ω is the fundamental irradiance and n_ω and $n_{3\omega}$ the refractive indices at the angular frequencies ω and 3ω.

The function $J(\Delta k;z_0;z) = \int_{z_0}^{z_1} \frac{\exp(i\Delta k u)}{(1+2iu/b)^2} du$ is the third-harmonic interaction length, $\Delta k = 3k_\omega - k_{3\omega}$ the phase mismatch between the fundamental and the third-harmonic waves, $b = 2\pi w_0^2/\lambda$ the confocal parameter, w_0 the beam waist of the fundamental wave, λ the wavelength in the medium and z_0 and z_1 the positions of interfaces.

No absorption loss corrections have been performed. Indeed the bulk samples and the laser induced defects are transparent at both the fundamental (1030 nm) and third-harmonic (343 nm) wavelengths (*cf.* figures 29 and 30, respectively). The refractive indices of the defect at ω and 3ω have been set to a value higher of an amount of 10^{-3} relative to the refractive indices of unexposed fused silica. This assumption is based on refractive index variation measurement of waveguides written in fused silica, at 633 nm. This variation has

been measured to be about 10^{-3} [Zou05]. Figure 35 is an abacus showing the theoretical ratio $R = I_{3\omega,bulk/def} \big/ I_{3\omega,air/bulk}$ (from equations B.8.2 and B.8.3) versus the ratio of the third-order susceptibilities $a = \chi^{(3)}_{def} \big/ \chi^{(3)}_{SiO_2}$. By reporting in figure 35 the experimental ratio R actually measured in figure 34, one can deduce the variation of the third-order susceptibility of the defect relative to the bulk. Nevertheless, by reporting one value of R, two values of a can be determined, one lower and one higher than unity. A previous experiment on the same defect, but at the surface of the material, permitted observation of a third-harmonic signal less important at the interface air/defect than at the interface air/bulk and to conclude to a third-order susceptibility lower for the defect than for the bulk [Zou05].

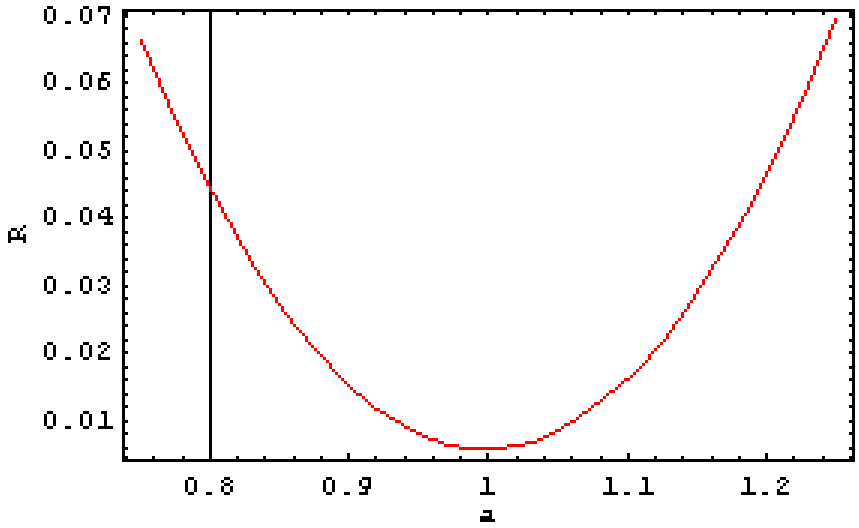

Figure 35: Evolution of the ratio of the third-harmonic irradiances $R = I_{3\omega,bulk/def} \big/ I_{3\omega,air/bulk}$ versus the ratio of the third-order susceptibilities $a = \chi^{(3)}_{def} \big/ \chi^{(3)}_{SiO_2}$ for the 5 µJ-exposed Herasil sample.

For a measured ratio $R \approx 0.053$, two values of a are found: 0.77 and 1.23. The value lower than 1 is retained, *i.e.* 0.77, and the variation of the third-order susceptibility of the defect relative to the bulk is

$$\frac{\Delta\chi^{(3)}}{\chi^{(3)}} = \frac{\chi^{(3)}_{def} - \chi^{(3)}_{SiO_2}}{\chi^{(3)}_{SiO_2}} \qquad \text{(B.8.4)}$$

Table 3 recapitulates the third-order susceptibility data for all the samples. Note that both $\chi^{(3)}$ and $\Delta\chi^{(3)}$ are the same, within the measurement uncertainties (~20%), for each sample. Moreover, no correlation was established between $\Delta\chi^{(3)}$ and the intensity of the absorption and luminescence bands attributed to the laser-induced color centers.

It is well known that THG is a process due to the electronic part of $\chi^{(3)}$, since only the electronic polarization is able to quickly respond to a high-frequency all-optical field excitation [Hel77]. Thus, the $\Delta\chi^{(3)}$ measured by THG microscopy is uniquely due to electronic motions. On the other hand, the Raman spectral density is related to the non-instantaneous nuclear contribution of $\chi^{(3)}$ [Hel75]. In other words, it is possible to compute the nuclear contribution of $\chi^{(3)}$ from the Raman spectra of the exposed samples. However, calculations show that the increase of the *D1* and *D2* lines and the decrease of the width of the main band at 440 cm^{-1} are clearly insufficient to participate in an additional nuclear $\Delta\chi^{(3)}$.

8.2. At the sub-wavelength scale

At a sub-wavelength scale, it appears that the response of fused silica to femtosecond laser irradiation consists in a “nanograting” structure with a periodic modulation of the refractive index. So far, three groups of scientists have observed this phenomenon: one group gathering people from the University of Kyoto and the University of Southampton [Shi03], one group from the University of Ottawa [Bha06], and one group from the University of Paris Sud [Pou08]. With only a few differences in their experimental results, the two first groups disagree about the mechanisms responsible for the formation of this structure. They have both a different approach: one based on an interference model and the other based on nanoplasmonics. In this section, we give an overview of the results obtained by the two groups as well as a description of the proposed models. Moreover, we present our preliminary

results in this field and we propose an explanation for the contradicting evolution of the changes in the linear and nonlinear optical properties by eliminating the one after the others all the hypotheses, included the form birefringence exhibited by the “nanogratings”.

8.2.1. State of the art

8.2.1.1. Interference approach

The first observation of the “nanograting” structure was achieved by Shimotsuma *et al.* [Shi03]. They used the beam from a regenerative amplified mode-locked Ti:Sa laser (λ_0 = 800 nm, τ_P = 150 fs, R = 200 kHz) focused with a microscope objective (100×, NA = 0.95) 100 µm below the surface. The point of focus was kept at the same position (stationary focus) and the beam diameter was estimated to be ~ 1 µm. The pulse energy was varied between 1 µJ and 3 µJ and the number of pulses between 50×10^3 and 80×10^3. The sample was then polished to the depth of the beam waist location. The surface of the polished sample was analyzed by scanning electron microscopy (SEM) and Auger electron spectroscopy.

Scanning electron microscopy was performed in two configurations, secondary and backscattering, which are sensitive to the surface morphology and the atomic weight of the elements constituting the observation surface, respectively. Figure 36 shows the pictures obtained by SEM.

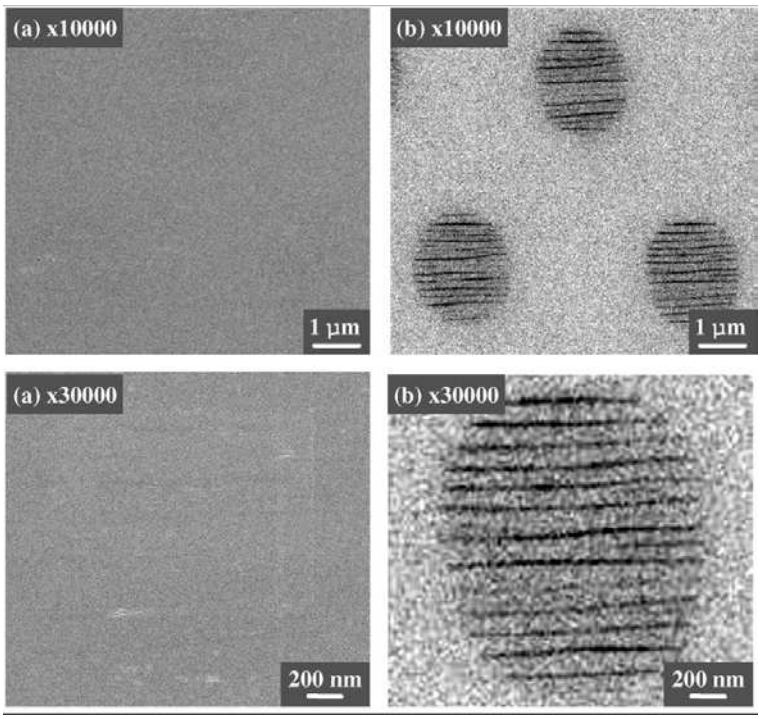

Figure 36: Secondary (on the left) and backscattering (on the right) electron images obtained with 10000× and 30000× magnifications [Shi03].

The observed structures in the backscattering configuration are periodic self-organized stripes, looking like "nanogratings". The stripes are aligned perpendicular to the laser polarization direction. The period of the structure is about 250 nm (roughly $\lambda_0/2n$, with $n = 1.46$ for fused silica) and the width of the stripes is about 20 nm. The period has been found to increase with the pulse energy and to decrease with the number of pulses.

In addition, Auger electron spectroscopy, which is sensitive to the molecular weight of atoms, has been performed, examining the sample for oxygen and silicon. Auger analysis revealed that the oxygen distribution is modulated whereas the silicon distribution remains constant. The stripes present a lower oxygen concentration than their neighboring, which show a higher oxygen concentration. This periodic modulation of the oxygen distribution leads to a modulation of the refractive index. The refractive index change in the high oxygen concentration regions is positive and on the order of 0.03 whereas in the low oxygen

concentration regions, it is negative and on the order of -0.3 [Bri04]. All the features of these "nanograting" structures are gathered in figure 37.

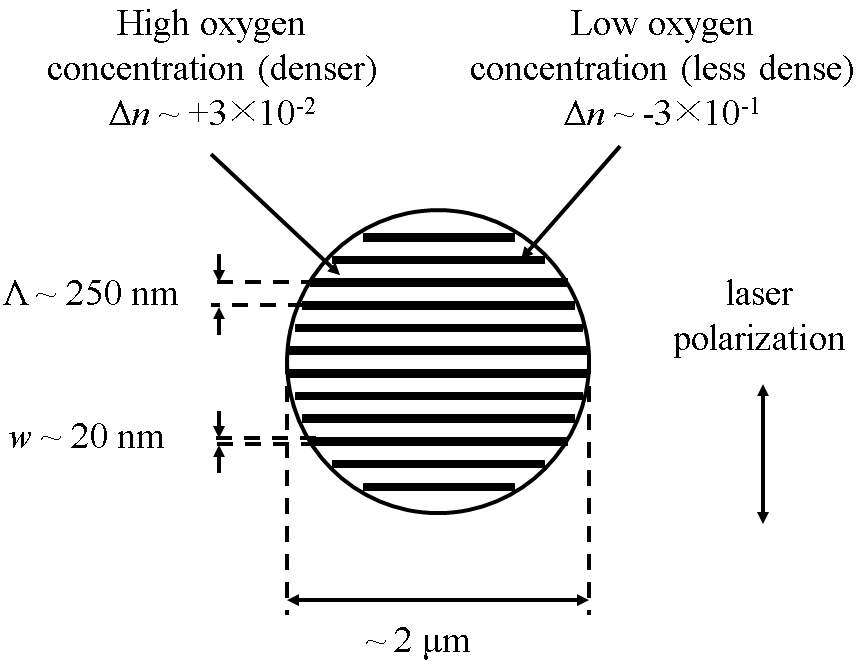

Figure 37: Recapitulation of the "nanograting" features. Λ is the period of the "nanograting" and w the width of the stripes.

The following model has been proposed to explain this phenomenon [Shi03] [Shi05]. Since the photons energy of the laser is much lower than the band gap energy of fused silica, multiphoton ionization takes place, leading to the production of a high free electron density. Therefore, the material has the properties of a plasma. The produced free electrons oscillate in the laser electric field, according to the following equation of motion

$$\frac{\partial v_e}{\partial t} + f_{ei} v_e = -\frac{e}{m_e} E \qquad \text{(B.8.5)}$$

where v_e is the electron velocity, f_{ei} the electron-ion collision frequency, e the electron charge, m_e the electron mass and E the electric field.

The kinetic energy of the free electrons is converted into thermal energy through electron-ion collisions (inverse Bremsstrahlung heating). The temperature of the plasma

increases, enabling the plasma to absorb the photons energy by one-photon absorption. This absorption in the electron plasma will excite electron plasma density waves, which are actually longitudinal acoustic waves (or Langmuir waves). The light can propagate through the plasma only at angular frequencies $\omega > \omega_P$, where ω is the laser angular frequency and ω_P the plasma angular frequency defined as

$$\omega_P = \sqrt{\frac{N_e e^2}{\varepsilon_0 m_e}} \tag{B.8.6}$$

The electron plasma density wave can couple via a Cherenkov-type phase-matching (*cf.* figure 38) with the laser wave only if it propagates in the plane of the laser polarization. In this type of phase matching, the plasma propagation constant is given by

$$k_{pl} = \sqrt{k_{ph}^2 + k_{gr}^2} = \sqrt{\left(\frac{2\pi}{\lambda}\right)^2 + \left(\frac{2\pi}{\Lambda}\right)^2} \tag{B.8.7}$$

where k_{ph}, k_{gr}, λ and Λ are the propagation constants and the wavelengths in the medium of the photon and the grating, respectively.

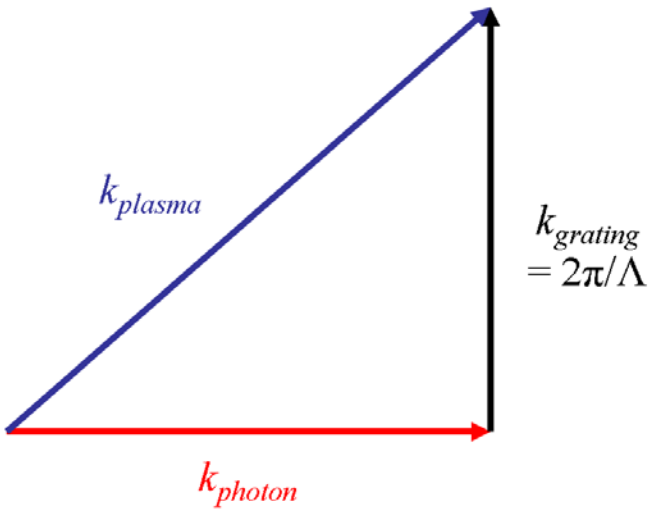

Figure 38: Coupling between the electron plasma density wave and the laser wave via a Cherenkov-type phase-matching.

The initial coupling is produced by inhomogeneities induced by electrons moving in the plane of the laser polarization. The interference of these two waves results in a periodic modulation of the electron plasma concentration and structural changes in the glass. The breaking of Si-O-Si bonds via multiphoton absorption is accompanied by the generation of color centers.

For a grating period of $\Lambda = 150\,\text{nm}$, the properties of the plasma have been evaluated [Shi03]:

- The electron plasma density, $N_C \approx 1.5\times10^{21}\ \text{cm}^{-3}$, which has to be compared to the critical electron density, $N_{cr} = \dfrac{\varepsilon_0 m_e \omega^2}{e^2} = 1.75\times10^{21}\ \text{cm}^{-3}$.

- The electron plasma temperature, $T_e = \dfrac{m_e\omega^2}{3k_B k_{pl}^2} \approx 1\times10^7\ \text{K}$.

8.2.1.2. Nanoplasmonics approach

These "nanograting" structures have also been observed by Bhardwaj *et al.* [Bha06]. A complete review paper about this research group's findings is given in [Tay08]. In this work, the authors used the fundamental and the frequency-doubled beams from a Ti:Sa laser (λ_0 = 800 and 400 nm, τ_P = 50 fs, R = 100 kHz) focused with two different microscope objectives (NA = 0.45 and 0.65) 100 µm below the surface while translating the sample perpendicular to the direction of propagation of the laser beam at a speed of 30 µm.s^{-1}. The beam diameter was estimated to be ~ 2 µm. The pulse energy was varied between 1 µJ and 3 µJ and the exposed regions were exposed to a few thousand of pulses. The sample was then cut, polished to the depth of the beam waist location and chemically etched (4 minutes in 1% HF). The surface of the polished and etched sample was analyzed by atomic force microscopy (AFM) and scanning electron microscopy (SEM).

The same “nanograting” structures seen by Shimotsuma *et al.* have been observed by the Bhardwaj team with a few differences. The first main difference is that the stripes are not simple lines but projections of planes (*cf.* figure 39), revealed by images of the cross-section of the stripes (**K**-**E** plane) and along the stripes (**E**-**S** plane). **K** is the direction of propagation of the laser beam, **E** the polarization direction and **S** the scan direction. The width of the arrays are about 10 nm and the grating spacing is about 240 nm (to be compared to $\lambda_0/2n = 276\,\text{nm}$). By turning the linear polarization of the laser, the “nanogratings” have been found to be always perpendicular to the polarization direction. However, no such structures have been observed with circular polarization. Moreover, the “nanogratings” can be erased and simultaneously be replaced with new ones. Here, the orientation of the resulting structure is determined by the polarization of the rewriting beam [Raj06].

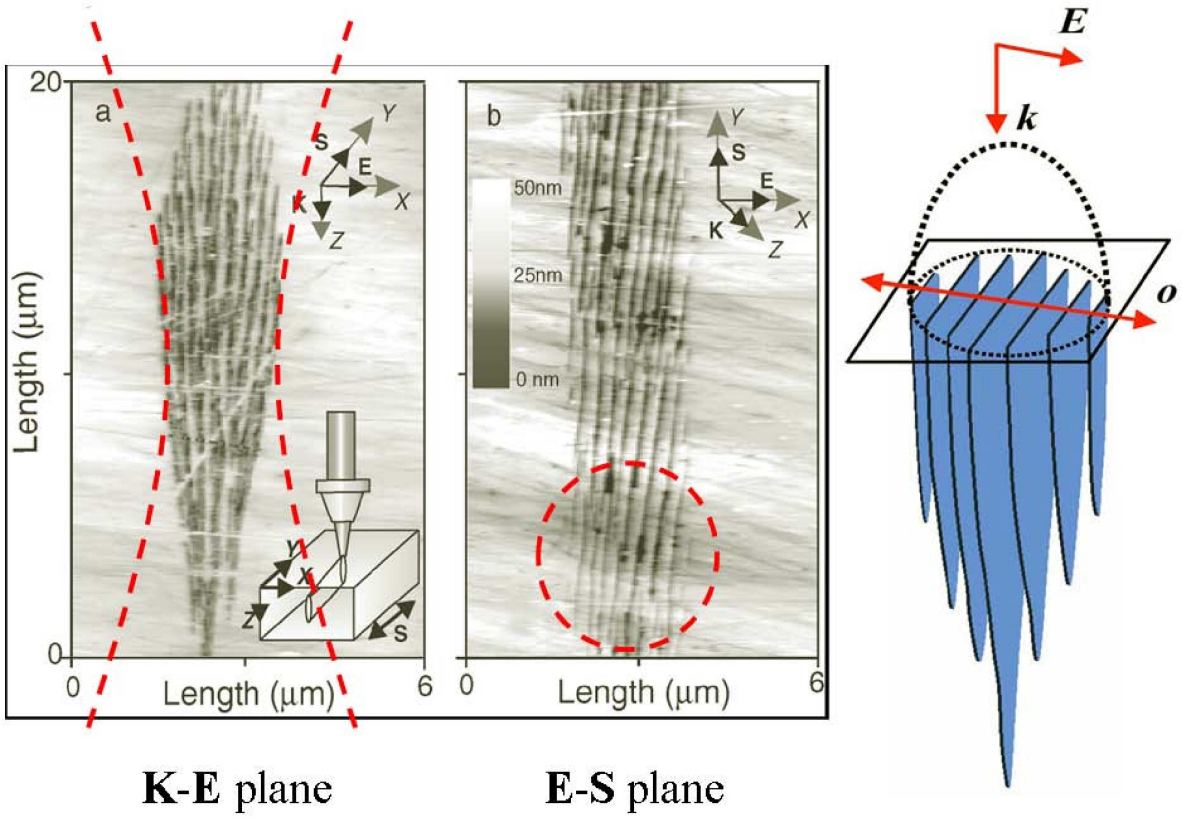

Figure 39: Atomic force microscope images of chemically etched laser-modified regions in the K-E plane (on the left) and in the E-S plane (in the middle) [Bha06]. Three-dimensional organization of the "nanogratings" (on the right) [Tay07]. o is the optical axis.

The second difference in the Bhardwaj study is that, unlike in the previous observations, the grating spacing does not depend on the pulse energy. This discrepancy has been explained by the fact that the Shimotsuma's 2D images were obtained mainly in the top of the laser-modified regions where non-systematic variation of the grating spacing with the pulse energy was observed by Bhardwaj *et al.* [Bha06]. This result is in contradiction with the interference model. Additionally, it was found that the grating spacing also does not depend on the pulse duration [Hna05].

In the interference approach, the grating spacing Λ depends on the electron plasma temperature T_e and density N_C; for $\Lambda = 150\,\text{nm}$, $T_e \approx 1\times10^7$ K and $N_C \approx 1.5\times10^{21}\,\text{cm}^{-3}$. However, to achieve these values, Bhardwaj *et al.* claim that a pulse energy of 11 µJ is

required, whereas the structures are formed with energies as low as 200 nJ [Bha06]. Moreover, the memory effect from one pulse to another which is implied by the nanoplanes formation, is not explained by this model. Because of these discrepancies, another model has been suggested, based on local field enhancement occurring during inhomogeneous breakdown (from the nanoplasmonics field) [Bha06].

Natural inhomogeneities in the dielectric (color centers or defects) can form nucleation centers for the creation of spherical nanoplasmas (*cf.* figure 40), following multiphoton ionization ("forest-fire" ionization and/or avalanche ionization). When $\varepsilon' = \frac{\varepsilon_{plasma}}{\varepsilon_{dielectric}} < 1$ (*i.e.* when $N_C < N_{cr}$), field enhancement occurs around the equator and the nanoplasmas expand to form oblate ellipsoids that evolve into a nanoplanes. These nanoplasmas naturally grow into nanoplanes when formed by linearly polarized electric fields. Since the plasmas are unconstrained, the growth will continue at the edges without limit.

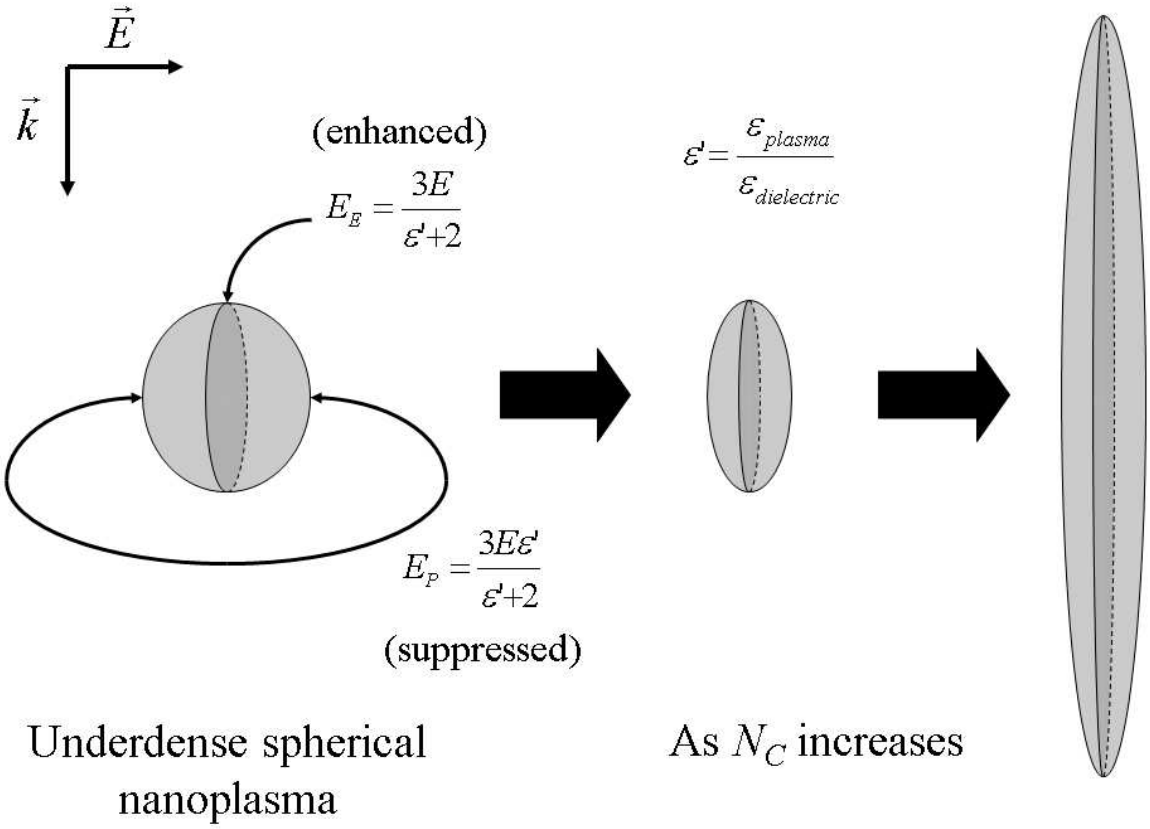

Figure 40: Schematic showing the local field enhancement of a spherical nanoplasma as the electron plasma density increases. E_E and E_P are the local fields found at the equator and poles of the sphere, respectively, for an overall field E.

The following statement has been proposed to explain the memory effect and the $\lambda_0/2n$ periodicity. First, it seems safe to assume that the critical density is exceeded. In this case, the sheets must affect light propagation; for a single sheet, surface plasmons will be excited and for multiple sheets, the light must adopt modes similar to those established in planar metallic waveguides. The order naturally evolves from a random distribution of nanoplasmas over many shots due to the memory mechanism and mode selection. Planes will be favored only if they support modes whose field distribution reinforces their own growth. Although a great deal of work is required to understand this in detail, the $\lambda_0/2n$ plane spacing is reminiscent of the minimum spacing required in a planar metal waveguide to support such modes having field maxima at the metal-dielectric interface. It is likely that

transient plasma based planar waveguides have similar properties favoring their development from an initially random nanoplasma distribution [Bha06].

8.2.2. "Nanogratings" observation

In order to get the know-how to observe the "nanograting" structures, we reproduced the irradiation conditions reported in the literature [Kaz07] on a fused silica sample (Infrasil). The beam from an Yb-doped glass fiber laser (μ-Jewel from IMRA, λ_0 = 1045 nm, τ_P = 350 fs, R = 200 kHz) was focused with a reflective microscope objective (NA = 0.5, *working distance* = 10 mm). A set of lines were written from one face of the material to the opposite one in a longitudinal configuration (*cf.* figure 41) at a speed of 200 μm.s^{-1}. The beam diameter was estimated to be ~ 2.6 μm. The pulse energy was 0.7 μJ and the number of pulses in a given spot area was about 3×10^3.

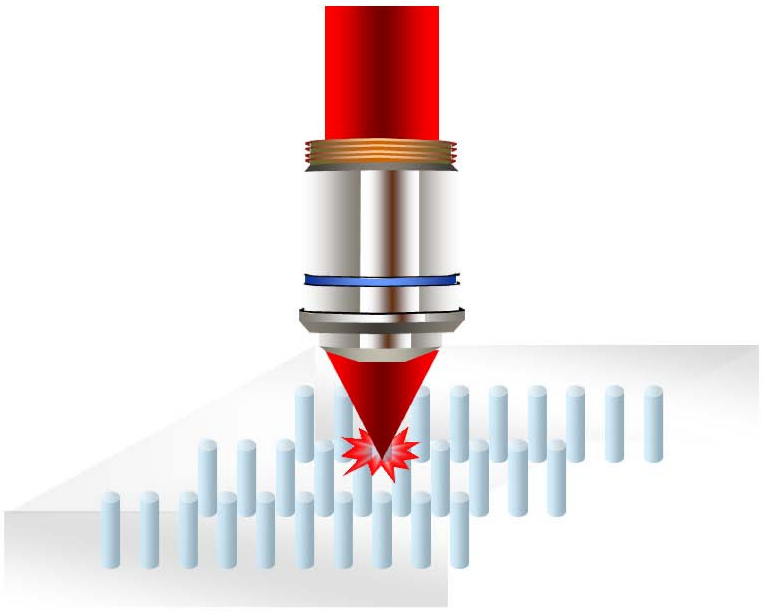

Figure 41: Longitudinal irradiation configuration.

The fused silica sample was then polished to remove the surface debris and chemically etched (20 minutes in 1% HF). The surface of the polished and etched sample was analyzed by SEM. The resulting SEM micrographs are given in figure 42. The grating period corresponds to the observations reported in the literature and is about $\lambda_0/2n = 360\,\text{nm}$.

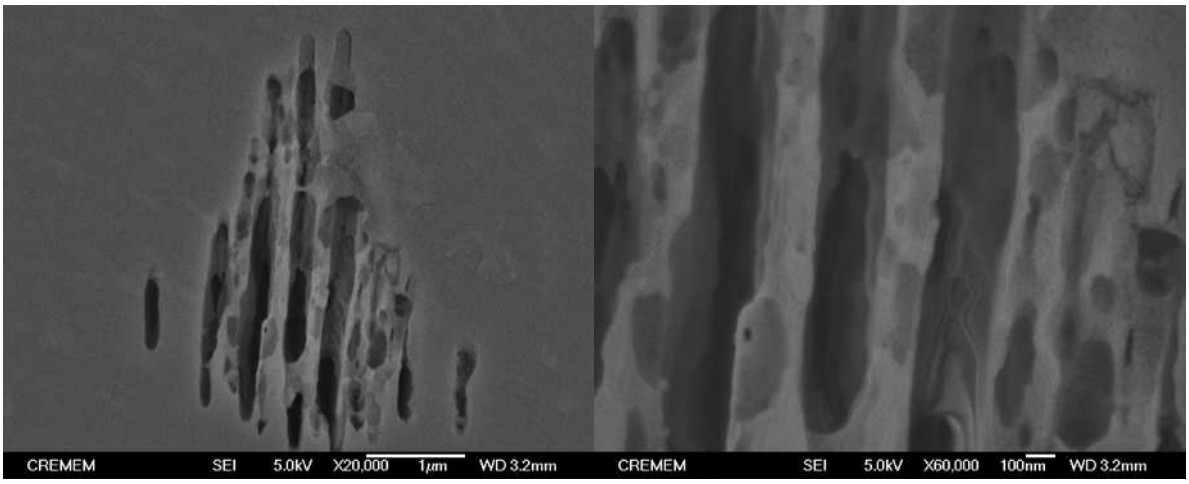

Figure 42: Secondary electron images of exposed fused silica obtained with 20000× (on the left) and 60000× (on the right) magnification.

8.2.3. Form birefringence

Since all the previous investigations did not give a conclusive correlation between the change in the optical properties, the initial impurity levels and the photo-induced structures, we must look for the explanation of the contradicting evolution somewhere else. It is now well known that fused silica does not respond in a homogeneous way to femtosecond laser irradiation. Indeed, submicron "nanograting" structures, consisting of a periodic modulation of the oxygen concentration and therefore of the refractive index, are created [Shi03]. It is important to note that the resolution of all the instruments used so far in this study is diffraction-limited and is not below 1 μm. Thus, all the performed characterizations are averaged, ignoring the "nanograting" behavior of the irradiated area.

These "nanogratings" were observed with lasers possessing intermediate repetition rates (200 kHz [Shi03] or 100 kHz [Bha06]) and relatively low energies (~ 1 μJ). Pulse after

pulse memory effects and pulse energy both play a role in their formation [Raj06]. Our irradiation conditions are different, *i.e.* low repetition rate (1 kHz) and high pulse energies (5 and 20 µJ), and we have not checked if the "nanogratings" are present in our case. However, we can discuss if these "nanogratings" are responsible for the contradicting evolution between Δn and $\Delta\chi^{(3)}$.

The "nanogratings" can be viewed as alternating layers of refractive index n_1, third-order susceptibility $\chi_1^{(3)}$ and thickness $t_1 = 10\,\text{nm}$ [Bha06] separated by layers of refractive index n_2, third-order susceptibility $\chi_2^{(3)}$ and thickness $t_2 = 240\,\text{nm}$ [Bha06] (*cf.* figure 43).

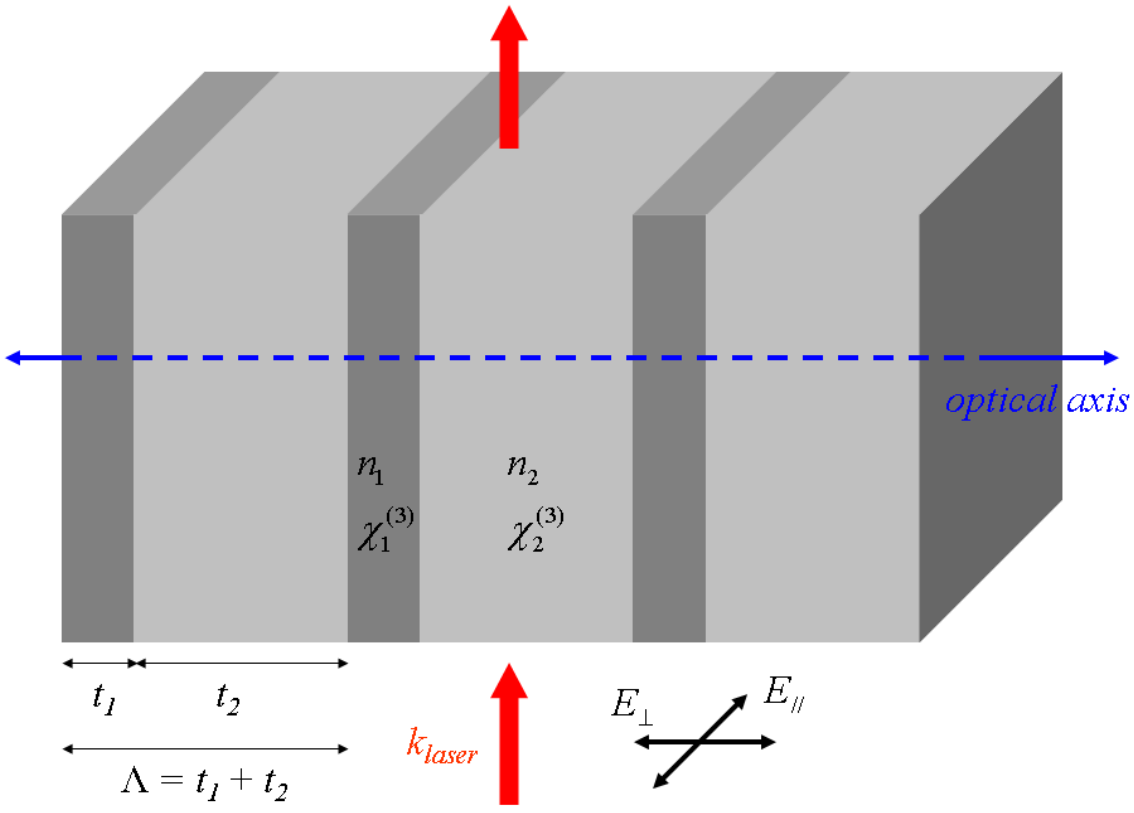

Figure 43: Schematic representation of a form birefringent "nanograting" with a period of $\Lambda = t_1 + t_2$. k_{laser}, $E_{//}$ and $E_\perp$ are the laser wave vector and the electric fields parallel and perpendicular to the plates, respectively.

Since t_1 and t_2 are small compared to the laser wavelength, these "nanogratings" exhibit form birefringence [Bri04]. They are optically homogeneous and behave like a

negative uniaxial crystal with the optical axis perpendicular to the plane of the plates [Bor99]. In such structures, the effective relative dielectric constants, with the electric field parallel or perpendicular to the plates, are respectively given by [Bor99]

$$\begin{cases} \varepsilon_{r//} = f_1\varepsilon_{r1} + f_2\varepsilon_{r2} \\ \varepsilon_{r\perp} = \dfrac{\varepsilon_{r1}\varepsilon_{r2}}{f_1\varepsilon_{r2} + f_2\varepsilon_{r1}} \end{cases} \tag{B.8.8}$$

where $f_1 = t_1/(t_1 + t_2)$ and $f_2 = t_2/(t_1 + t_2)$ are the fractions of the total volume occupied by the layers and by the plates, respectively.

The effective relative dielectric constant can be developed in terms of linear refractive index and third-order susceptibility, such as $\varepsilon_{rj} = n_i^2 + \chi_i^{(3)}E^2$ where $j = //$ or $\perp$, $i = 1$ or 2 and E the electric field. By grouping and identifying the terms without or with a quadratic dependence with the electric field, one can obtain the effective refractive index and third-order susceptibility for the "nanogratings"

$$\begin{cases} n_{//}^2 = f_1 n_1^2 + f_2 n_2^2 \\ n_{\perp}^2 = \dfrac{n_1^2 n_2^2}{f_1 n_2^2 + f_2 n_1^2} \end{cases} \tag{B.8.9}$$

$$\begin{cases} \chi_{//}^{(3)} = f_1\chi_1^{(3)} + f_2\chi_2^{(3)} \\ \chi_{\perp}^{(3)} = \dfrac{f_1 n_2^4 \chi_1^{(3)} + f_2 n_1^4 \chi_2^{(3)}}{\left(f_1 n_2^2 + f_2 n_1^2\right)^2} \end{cases} \tag{B.8.10}$$

Bricchi *et al.* measured the changes in the refractive index at 633 nm [Bri04]. Among various possibilities, they chose to retain negative values of the refractive index for the oxygen-deficient region, $\Delta n_1 \equiv n_1 - n_{SiO_2} = (-4 \text{ to } -2)\times 10^{-1}$, and positive values of the refractive index for the oxygen-abundant region, $\Delta n_2 \equiv n_2 - n_{SiO_2} = (2 \text{ to } 5)\times 10^{-2}$ [Bri04]. However, from a physical-chemical point of view, it is more than probable that the oxygen-deficient region, even if it is less dense than the bulk material, presents a positive Δn since its composition has become closer to silicon, which has a higher refractive index than fused

silica. Based on the same reasoning, the oxygen-abundant region should present a negative Δn.

For $\chi_1^{(3)}$ and $\chi_2^{(3)}$, no measurement is available in the literature. However, they can be estimated according to the semi-empirical Wang's rule, $\chi_i^{(3)} = A\left(n_i^2 - 1\right)^4$ [Boy07], with $A = \chi_{SiO_2}^{(3)} \Big/ \left(n_{SiO_2}^2 - 1\right)^4 = 1.66 \times 10^{-22}\ \mathrm{m}^2.\mathrm{V}^{-2}$, $\chi_{SiO_2}^{(3)} = 2.65 \times 10^{-22}\ \mathrm{m}^2.\mathrm{V}^{-2}$ [Hel77] and $n_{SiO_2} = 1.457$ at 633 nm.

For each electric field polarization (parallel or perpendicular to the plates), the changes in the refractive index $\left(n_j - n_{SiO_2}\right)/n_{SiO_2}$ and in the third-order susceptibility $\left(\chi_j^{(3)} - \chi_{SiO_2}^{(3)}\right)/\chi_{SiO_2}^{(3)}$ are computed, relative to the bulk material. Figure 44 shows the iso-curves for $0.1\% \le \Delta n/n \le 0.5\%$ and $-30\% \le \Delta\chi^{(3)}/\chi^{(3)} \le -10\%$ versus Δn_1 and Δn_2, for both parallel and perpendicular electric field configurations. It demonstrates that $\Delta n/n$ and $\Delta\chi^{(3)}/\chi^{(3)}$ can never follow contradicting evolutions, because their respective iso-curves never cross each other. Thus, the "nanogratings" form birefringence cannot explain the contradicting evolution of the linear and nonlinear optical properties of exposed fused silica.

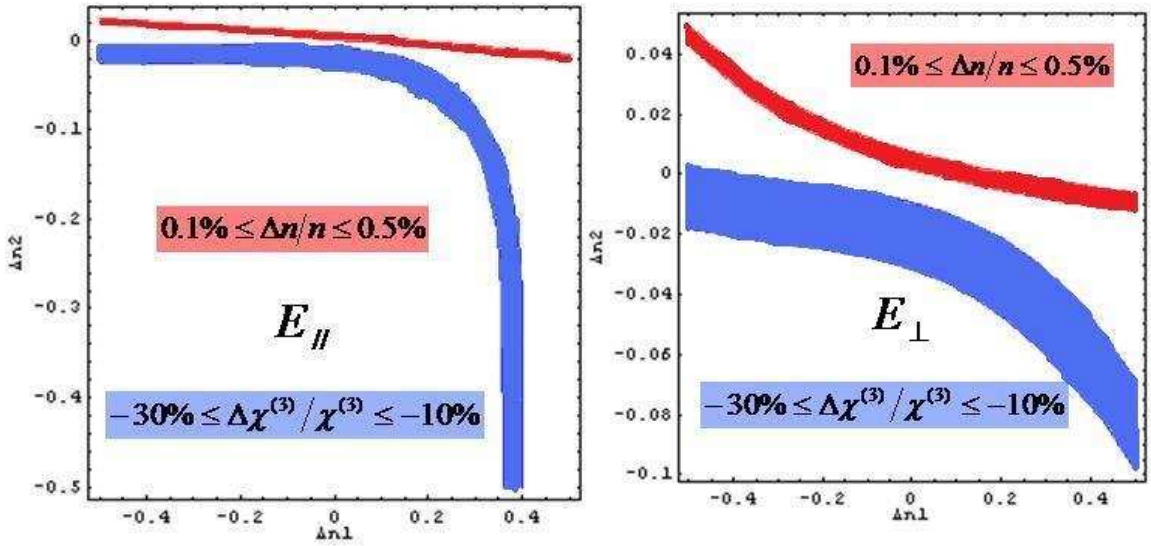

Figure 44: Iso-curves of $0.1\% \le \Delta n/n \le 0.5\%$ (in red) and $-30\% \le \Delta\chi^{(3)}/\chi^{(3)} \le -10\%$ (in blue) versus Δn_1 and Δn_2 for the electric field parallel (on the left) and perpendicular (on the right) to the plates.

Thus, in our assessment, the only possibility that remains to explain this discrepancy is due to a failure in the experimental data acquisition since, in our measurements, we did not take into account the scattering losses in the exposed fused silica samples. Within the context of Rayleigh's theory, the "nanograting" structures are ideal scattering centers since their characteristic size is much smaller than the wavelength [Hul81]. In THG microscopy measurements, the photo-induced defects, even at low energies, scatter the third-harmonic light. As a result, its collect by the PMT is less important and the third-harmonic signal is artificially decreased. In self-phase modulation measurements, guided photons are scattered. The irradiance decreases during the propagation inside the waveguide. As a consequence, the phase-shift is under-estimated, so is the nonlinear refractive index.

8.3. Summary

Three different femtosecond laser exposed fused silica samples were examined to tentatively correlate the changes in the linear and nonlinear optical properties with the photo-induced structures and to explain their contradicting evolution. The study gave the following results:

- Color centers (*E'* centers, ODCs (II) and NBOHCs) are created following exposure. No relation was established with the initial impurity levels of the samples.
- The initial impurity levels as well as the laser induced color centers play no significant role in the changes of the refractive index and the third-order susceptibility.
- The densification of the laser exposed regions, revealed by Raman spectroscopy, is probably the mechanism for the observed positive refractive index change.
- Form birefringence due to self-organized "nanograting" structures is not responsible for the contradicting evolution of the linear and nonlinear optical properties.

- An experimental artifact in the measurements of the nonlinear optical properties due to scattering centers is, according to us, the only possible explanation for this contradicting evolution.
- In addition, for photonic device applications based on either the linear or the nonlinear optical properties of the photo-induced structures, the choice of the fused silica basic material is not critical.

CHAPTER NINE: STRUCTURING OF OTHER OXIDE GLASSES

Fused silica has been, from far, the most studied of the glasses. Indeed, its relatively simple chemical composition makes easier the elaboration of theoretical models. It was shown in the previous chapter that formation of color centers, densification, refractive index and third-order susceptibility changes and creation of "nanogratings" can result from femtosecond laser irradiation. A question then comes to mind: Do all the oxide glasses respond the same way? To answer this interrogation, other oxide glasses, presenting different chemical compositions, are investigated in this chapter to get a global picture.

Post-exposure characterization of photo-induced structures does not supply information about the underlying processes occurring during the irradiation. To fully understand what happens from the early stages to the end of laser-material interaction, real time studies have to be performed. The problem can be summarized into one interrogation: What are the mechanisms responsible for the absorption and the dissipation of the pulse energy? A corollary is: is there formation of a plasma, *i.e.* an ionized gas, or an electron gas? The measurement of the free electron density is of importance since all the models rely on this parameter (see for example the proposed models for the "nanogratings" formation inside fused silica in section 8.2.1). The knowledge of both the magnitude and the temporal dynamic of this property is crucial for a model proposition.

In this chapter, three different oxide glass families (sodium-borophosphate niobium containing, silicate without and with silver and zinc phosphate silver containing) exposed to femtosecond pulses are investigated. For each family, SEM and/or confocal fluorescence microscopy have been performed to characterize the photo-induced structures. The case of the zinc phosphate silver containing glass is studied more in detail. To understand and identify the interaction processes, real time spectral interferometry, transient absorption and THG

microscopy experiments have been carried out on this glass. The free electron density has been measured from spectral interferometry and transient absorption experiments and the cumulative effects have been studied by THG microscopy.

9.1. Sodium-borophosphate-niobium

The sample under investigation is a sodium-borophosphate glass containing 9.55% of niobium oxide (*cf.* section 6.2). The optical properties of this glass can be found in table 2. The beam from a Ti:Sa regenerative amplifier (Spitfire system from Spectra Physics, λ_0 = 800 nm, τ_P = 100 fs, R = 1 kHz) was focused with a microscope objective (NA = 0.25, *working distance* = 5 mm). A set of 300 µm long lines was written 200 µm blow the surface in a transverse configuration (*cf.* figure 45) at a 5 µm.s^{-1} speed. The beam diameter was estimated to be ~ 4 µm. The pulse energy was 2 µJ and the number of pulses in a given spot area was about 10^3.

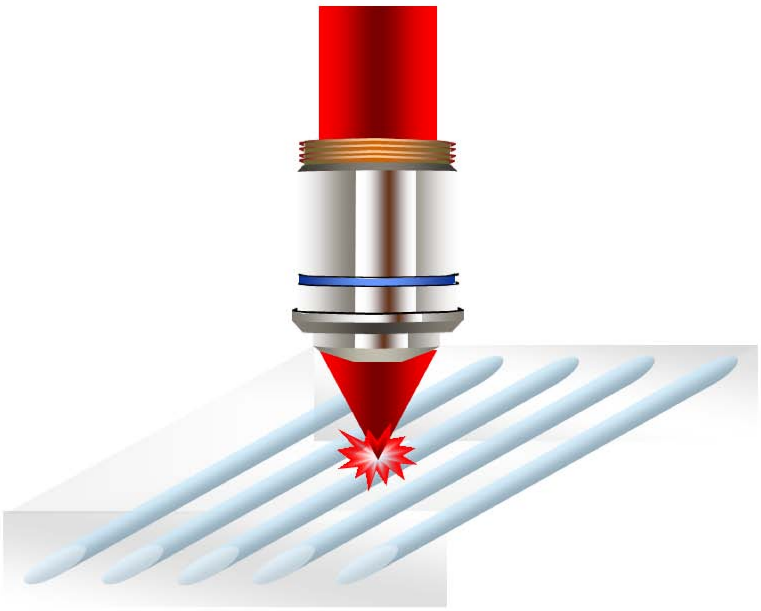

Figure 45: Transverse irradiation configuration.

The sample was polished to remove the surface debris and analyzed by secondary and backscattering SEM. The SEM pictures are given in figure 46. Both images show micro-cracks, also observed in fluoro-aluminate glasses [Ehr04]. These cracks could be due to a shock wave induced by the laser, followed by a compression of the material, leading to a breakdown. In addition, crystallites with sizes on the order of 200 nm can be observed in both images, with a best contrast on the backscattering electron picture, because of the different chemical composition of the nanocrystallites from the glass.

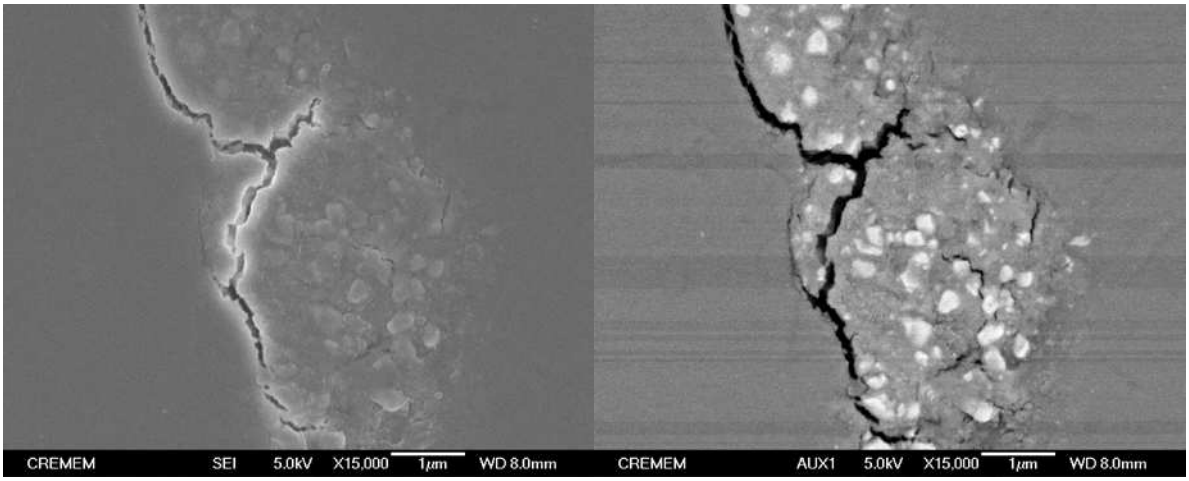

Figure 46: Secondary and backscattering electron microscopy images of exposed 9.55% Nb_2O_5 sodium-borophosphate glass.

9.2. Silicate

The sample under investigation is a silicate glass. Its chemical composition is $75SiO_2$-10CaO-$15Na_2O$ (mol. %) and its cutoff wavelength is about 300 nm. The linear and nonlinear refractive indices are $n_0 = 1.52$ and $n_2 = 3\times10^{-16}\,\mathrm{cm}^2.\mathrm{W}^{-1}$, respectively. The beam from an Yb-doped glass fiber laser (μ-Jewel from IMRA, λ_0 = 1045 nm, τ_P = 350 fs, R = 100 kHz) was focused with a reflective microscope objective (*NA* = 0.5, *working distance* = 15 mm). A set of lines was written from one face of the material to the opposite one in a longitudinal configuration (*cf.* figure 41) at a 100 μm.s^{-1} speed. The beam diameter was estimated to be ~

2.6 µm. The pulse energy was 0.7 µJ and the number of pulses in a given spot area was about 3×10^3.

The silicate sample was then polished to remove the surface debris and chemically etched (20 minutes in 1% HF). The surface of the polished and etched sample was analyzed by SEM. The SEM pictures are given in figure 47. Like in fused silica, "nanograting" structures are observed with a period on the order of $\lambda_0/2n = 345$ nm.

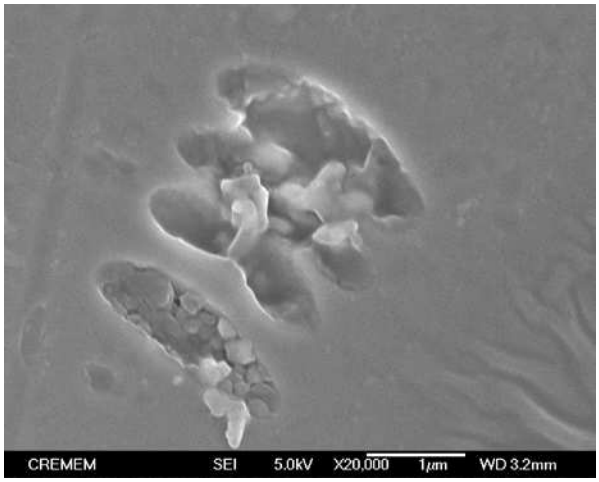

Figure 47: Secondary electron microscopy image of exposed silicate glass.

9.3. Silver silicate

A similar silicate glass containing 1.27% of silver has been studied. Its chemical composition is $69.98SiO_2$-$12.38CaO$-$16.37Na_2O$-$1.27Ag_2O$ (mol. %) and its cutoff wavelength is about 280 nm. This blue shift of the cutoff wavelength is due to the absorption band of the dopant silver ions Ag^+. The addition of silver is relevant because it can be used as a post-irradiation fluorescent probe for investigation of the silver photo-diffusion. The irradiation conditions were the same as for the silicate glass, but with different repetition rates R = 100 kHz and 1 MHz. The writing speeds were 0.1 and 1 mm.s^{-1}, so that the number of pulses in a given spot area was kept the same for each repetition rate, about 3×10^3. A set of lines was written from one face of the material to the opposite one in a longitudinal

configuration (*cf.* figure 41). The pulse energies were 100, 400, 700 and 1000 nJ at 100 kHz and 70, 100 and 140 nJ at 1 MHz.

Figures 48 and 49 show confocal fluorescence microscopy images of the photo-induced structures at 100 kHz and 1 MHz, respectively. At 100 kHz, fluorescent structures with no specific geometry have been created. The fluorescence intensity seems not to depend on the pulse energy. At 1 MHz, fluorescent ring structures are observed, with the fluorescence intensity increasing with the pulse energy.

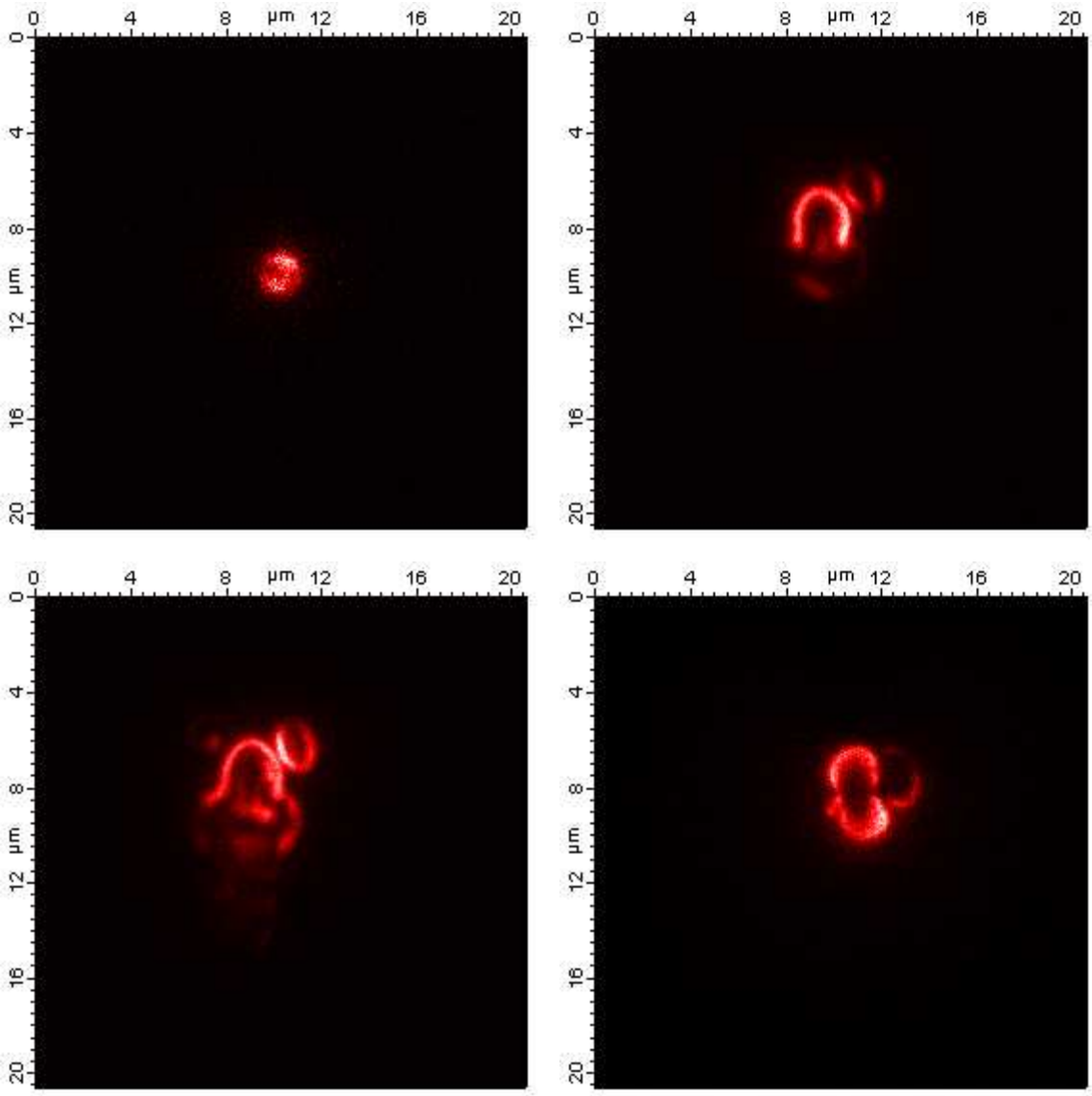

Figure 48: Fluorescence microscopy images of exposed silver silicate glass with 100, 400, 700 and 1000 nJ pulse energies at 100 kHz repetition rate. The excitation wavelength is 405 nm.

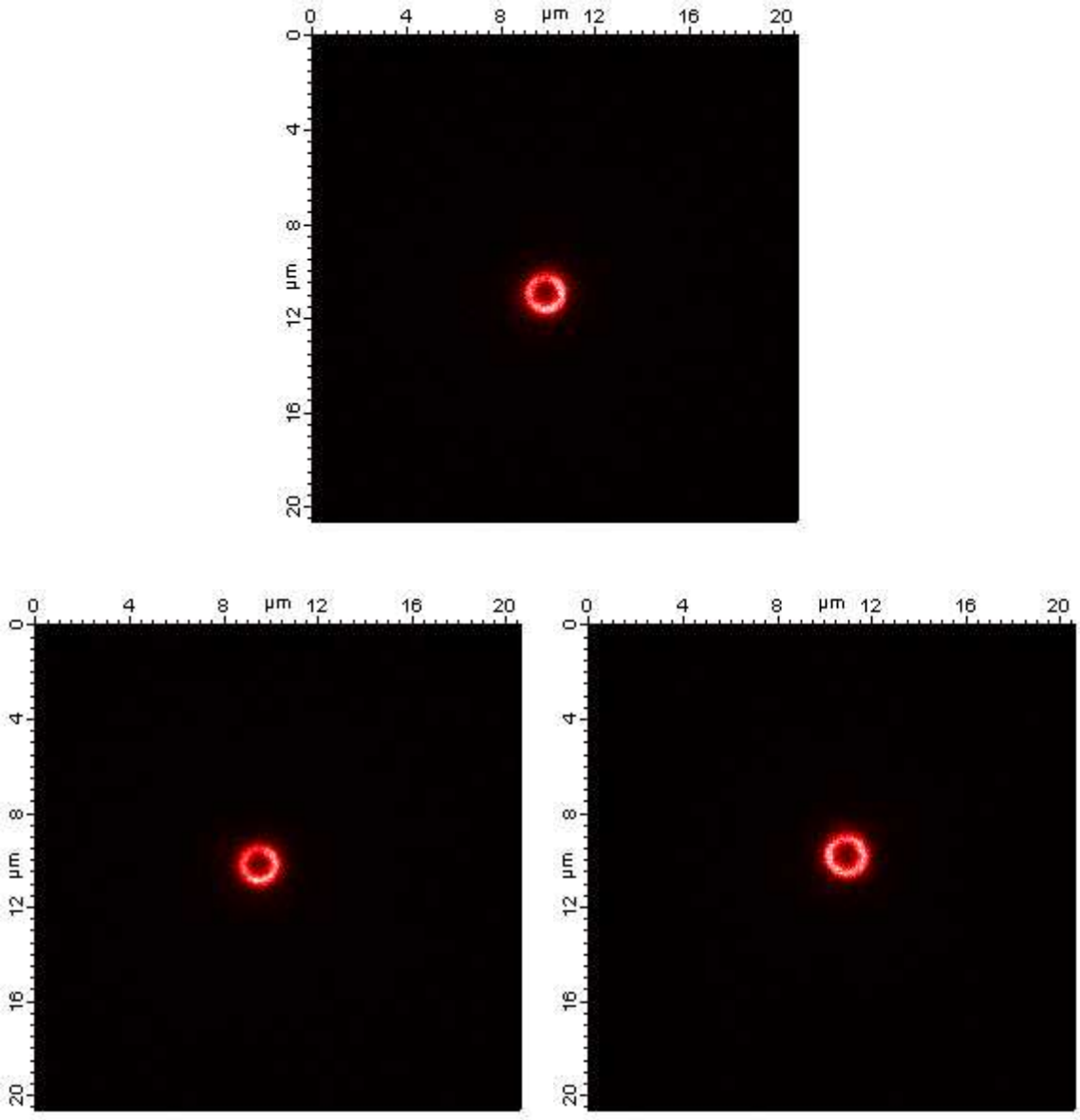

Figure 49: Fluorescence microscopy images of exposed silver silicate glass with 70, 100 and 140 nJ pulse energies at 1 MHz repetition rate. The excitation wavelength is 405 nm.

Clearly, from the confocal fluorescence microscopy images, the repetition rate of the laser plays a role in the formation of these ring structures, letting think that thermal effects are involved in this process. More details will be given in the next section with a zinc phosphate glass silver containing.

9.4. Silver zinc phosphate

The sample under investigation is a zinc phosphate glass containing 4% of silver. Its chemical composition is $55ZnO\text{-}40P_2O_5\text{-}4Ag_2O\text{-}1Ga_2O_3$ (mol. %) and its cutoff wavelength is about 270 nm. The linear refractive index is $n_0 = 1.58$. The beam from an Yb:KGW diode pumped oscillator (t-Pulse 500 from Amplitude Systemes, λ_0 = 1030 nm, τ_P = 470 fs, R = 9.45 MHz) was focused with a reflective microscope objective (*NA* = 0.52, *working distance* = 15 mm). A set of lines was written from one face of the material to the opposite one in a longitudinal configuration (*cf.* figure 41) at a 1 $mm.s^{-1}$ speed. The beam diameter was estimated to be ~ 2.4 µm. The pulse energy was 60 nJ and the number of pulses in a given spot area was about 11×10^3. The refractive index modification threshold of this glass was previously determined and is about 9 $TW.cm^{-2}$ [Can08].

Figure 50 shows a confocal fluorescence microscopy image of the photo-induced structures. Like for the silver silicate glass, a fluorescent ring in 2D is observed, a pipe in 3D. The thickness of the ring structure measured by fluorescence confocal microscopy is limited by the resolution at 350 nm. Thus, even if the thickness of the ring structure is lower than this value, this technique cannot reveal the real size.

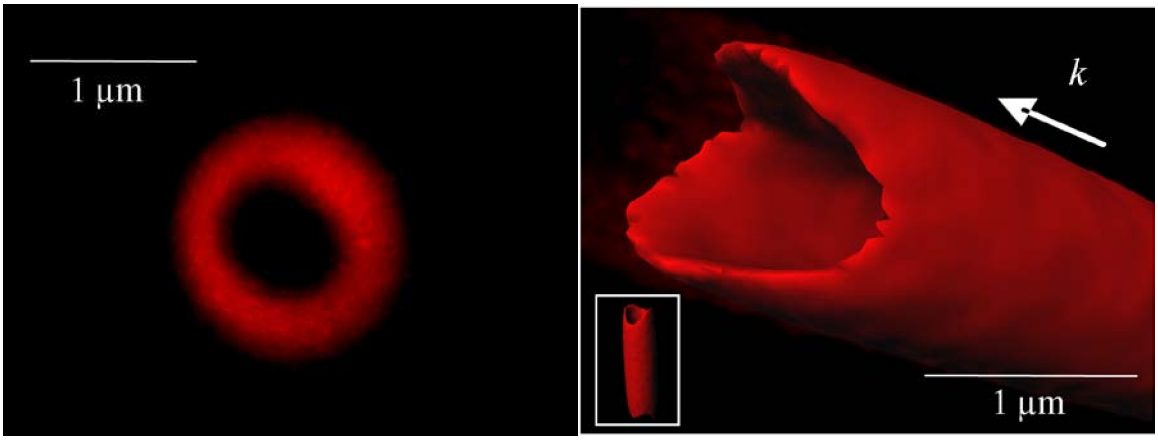

Figure 50: 2D (on the left) and 3D reconstruction (on the right) confocal fluorescence microscopy images of exposed silver zinc phosphate glass. The excitation wavelength is 405 nm.

To overcome this problem, SEM was used. The silver zinc phosphate sample was polished to remove the surface debris and chemically etched (20 seconds in 0.5% HNO_3). The surface of the polished and etched sample was analyzed by SEM. The SEM picture is given in figure 51; it reveals an 80 nm-thick ring structure.

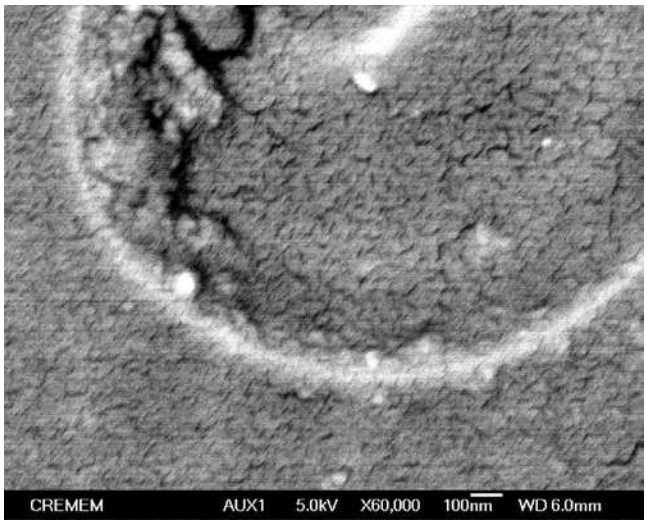

Figure 51: Backscattering SEM image of exposed silver zinc phosphate glass.

Previous work showed that the photo-induced fluorescent species are silver clusters Ag_m^{x+} (Ag_2^{+}, Ag_3^{2+}, Ag_8^{2+}, etc…), where m is the number of atoms (m<10) and x the ionization degree [Can08]. They are formed according to the following steps:

- Photo-ionization releases electrons from the valence band to the conduction band.
- Released photoelectrons are trapped by Ag^+ ions to form silver atoms Ag^0.
- Pulse after pulse cumulative effects increase locally the temperature, enabling thermal diffusion to occur. Ag^0 and Ag^+ interact then to give rise to silver clusters Ag_m^{x+}.
- Subsequent laser pulses photo-dissociate the newly formed Ag_m^{x+} except on the edges of the interaction area (where the threshold to photo-dissociate the clusters is not reached), leaving a ring structure composed of silver clusters.

In summary, confocal fluorescence microscopy, SEM and previous work [Can08], reveal that, even below the refractive index modification threshold (9 $TW.cm^{-2}$), fluorescent silver clusters, arranged in an 80 nm-thick ring structure, are created following exposure.

9.5. Free electron density measurement

When a femtosecond pulse is focused into a material, a gas of electrons in the conduction band of the glass is generated. This free electron density can be measured with pump-probe experiments. The change in the optical properties (the complex refractive index) associated to this electron gas and induced by the pump pulse is measured by the probe pulse.

Several measurements of free electron densities have been performed by different research groups. Most of them were carried out on fused silica with intense amplified femtosecond lasers and all the measured values were about 10^{19} cm^{-3}, even though the irradiance on the sample was very different, from 10 $TW.cm^{-2}$ [Tem06] to 100 $PW.cm^{-2}$ [Pap07], passing through 30 $TW.cm^{-2}$ [Aud94].

The electron gas behaves like a metal, and then its optical properties can be described by the Drude model. In order to measure this free electron density, two pump-probe experiments have been carried out: spectral interferometry and transient absorption experiments. In this section, the Drude model is first described. Then, for both experiments, the experimental setups, the results and the analysis are given. It will be seen that the transient absorption experiment is much more sensitive than the spectral interferometry one. This latter will allow us to give a superior limit to the free electron density whereas the first one will supply a precise measurement.

9.5.1. Drude model of the optical properties of an electron gas

An electron gas behaves like a metal. It is then appropriate to apply the Drude model to describe its optical properties. The band diagram of this electron gas is described in figure 52. The reasonable following assumptions will be done to simplify the theory:

- The sample is transparent in the absence of the pump, so that the refractive index of the glass without the pump is real.

- The mass of the electrons in the conduction band is the same as the one of the electrons in the valence band (no effective mass).

- Only the electrons absorb the light and not the color centers or other defects appearing in the band gap.

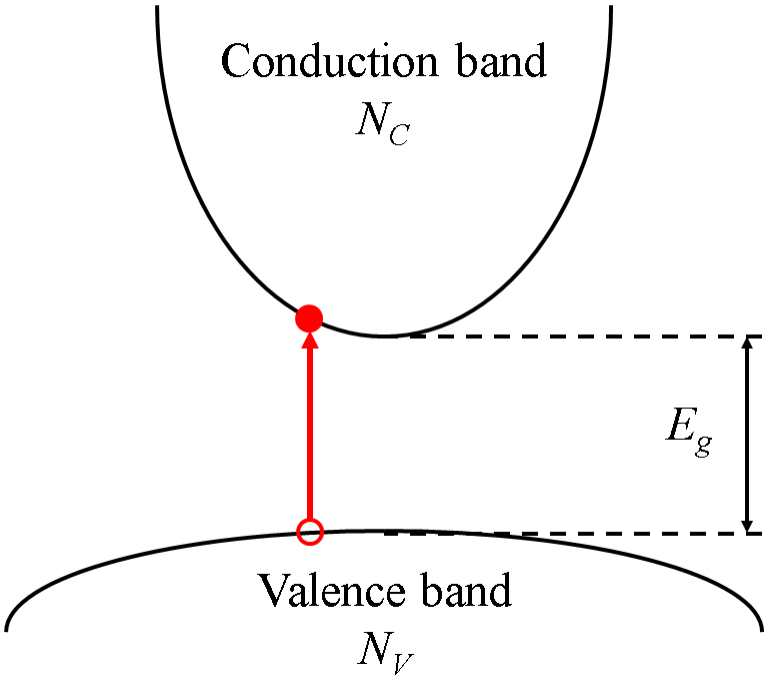

Figure 52: Band diagram of the electron gas. N_C is the electron density in the conduction band, N_V the electron density in the valence band and E_g the band gap energy.

The real refractive index in the absence of the pump pulse is given by the following well known expression

$$n_{without\ pump} = n_0 = \sqrt{1 + \frac{N_V e^2}{\varepsilon_0 m_e \left(\omega_0^2 - \omega^2\right)}} \tag{B.9.1}$$

where ω_0 is the band gap resonance angular frequency and N_V the electron density in the valence band.

In the presence of the pump pulse, two contributions have to be taken into account: Kerr self-focusing and free electron defocusing. The complex refractive index is then given by

$$\eta_{with\ pump} = \eta + n_2 I_{pump} = \sqrt{1 + \frac{\left(N_V - N_C\right)e^2}{\varepsilon_0 m_e \left(\omega_0^2 - \omega^2\right)} - \left[\frac{N_C e^2 \tau_c^2}{\varepsilon_0 m_e \left(1 + \omega^2 \tau_c^2\right)} + i \frac{N_C e^2 \tau_c}{\varepsilon_0 m_e \omega \left(1 + \omega^2 \tau_c^2\right)}\right]} + n_2 I_{pump} \tag{B.9.2}$$

where N_C is the electron density in the conduction band (or free electron density), τ_c the electron collision time, n_2 the nonlinear refractive index and I_{pump} the pump irradiance.

By performing a Taylor expansion of equation (B.9.2)

$$\sqrt{a - x} = \sqrt{a\left(1 - \frac{x}{a}\right)} = \sqrt{a}\sqrt{\left(1 - \frac{x}{a}\right)} \approx \sqrt{a}\left(1 - \frac{x}{2a}\right) \approx \sqrt{a} - \frac{x}{2\sqrt{a}} \text{ with } x << a$$

$$a \equiv 1 + \frac{\left(N_V - N_C\right)e^2}{\varepsilon_0 m_e \left(\omega_0^2 - \omega^2\right)} \text{ and } x \equiv \frac{N_C e^2 \tau_c^2}{\varepsilon_0 m_e \left(1 + \omega^2 \tau_c^2\right)} + i \frac{N_C e^2 \tau_c}{\varepsilon_0 m_e \omega \left(1 + \omega^2 \tau_c^2\right)}$$

(B.9.3)

the complex refractive index in the presence of the pump becomes

$$\eta_{with\ pump} \approx \sqrt{1 + \frac{\left(N_V - N_C\right)e^2}{\varepsilon_0 m_e \left(\omega_0^2 - \omega^2\right)}} - \left[\frac{N_C e^2 \tau_c^2}{\varepsilon_0 m_e \left(1 + \omega^2 \tau_c^2\right)} + i \frac{N_C e^2 \tau_c}{\varepsilon_0 m_e \omega \left(1 + \omega^2 \tau_c^2\right)}\right] \frac{1}{2\sqrt{1 + \frac{\left(N_V - N_C\right)e^2}{\varepsilon_0 m_e \left(\omega_0^2 - \omega^2\right)}}} + n_2 I_{pump}$$

(B.9.4)

$$\eta_{with\ pump} \approx n_0 + n_2 I_{pump} - \frac{1}{2n_0}\left[\frac{\omega_P^2 \tau_c^2}{1 + \omega^2 \tau_c^2} + i \frac{\omega_P^2 \tau_c}{\omega\left(1 + \omega^2 \tau_c^2\right)}\right] \tag{B.9.5}$$

with $N_C << N_V \Rightarrow (N_V - N_C) \approx N_V$ and $\omega_P = \sqrt{\frac{N_C e^2}{\varepsilon_0 m_e}}$ the plasma angular frequency. The complex refractive index contains a positive contribution due to Kerr self-focusing and a negative one due to free electron defocusing.

The real and imaginary parts of the complex refractive index in the presence of the pump become

$$\begin{cases} \eta_{with\ pump} = n_{with\ pump} - i\kappa_{with\ pump} \\ n_{with\ pump} \approx n_0 + n_2 I_{pump} - \frac{1}{2n_0}\frac{\omega_P^2 \tau_c^2}{1+\omega^2\tau_c^2} \\ \kappa_{with\ pump} \approx \frac{1}{2n_0}\frac{\omega_P^2 \tau_c}{\omega(1+\omega^2\tau_c^2)} \end{cases} \quad \text{(B.9.6)}$$

9.5.2. Spectral interferometry experiment

This experiment is based on the real part of the complex refractive index given by equation (B.9.6). It consists in mixing in a spectrometer two pulses (a reference and a probe) separated by a fixed delay τ_1 and a pump pulse focused inside the sample at some time between the two probe pulses (*cf.* figure 53). The probe pulse experiences therefore a different phase than the reference one [Mar97].

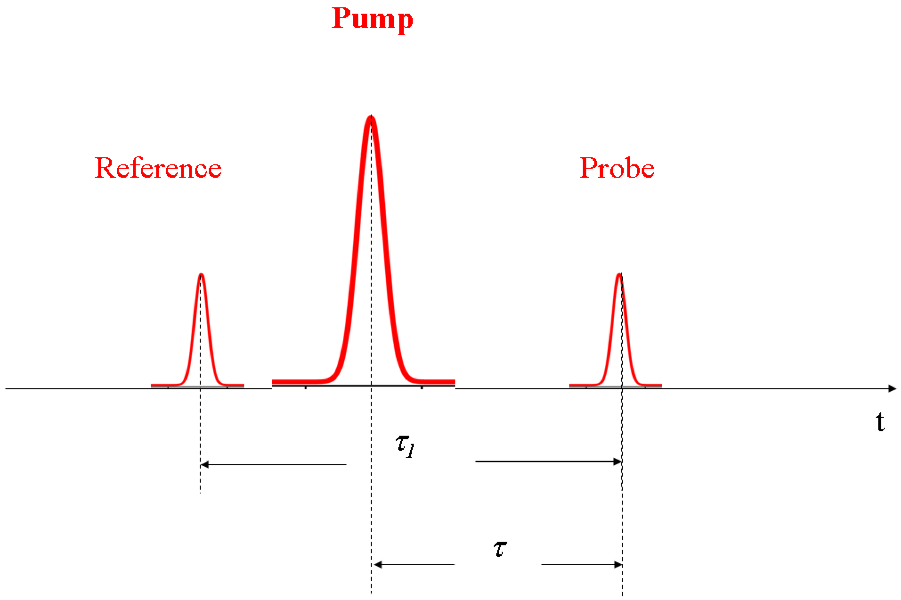

Figure 53: Time sequence of the reference, pump and probe pulses sent into the sample.

In the absence of the pump pulse, the spectral intensity is given by

$$I(\omega) = 2I_0(\omega)\left[1+\cos(\omega\tau_1)\right] \tag{B.9.7}$$

The spectrum exhibits fringes with a period inversely proportional to the time delay τ_1 (*cf.* figure 54).

In the presence of the pump pulse, the spectral intensity becomes

$$I(\omega) = I_0(\omega)\left[1+T+2\sqrt{T}\cos(\omega\tau_1+\Delta\phi)\right] = I_0(\omega)\left[1+T+2\sqrt{T}\cos(\omega\tau_2)\right] \tag{B.9.8}$$

where T is the Fresnel transmission and $\Delta\phi$ the phase shift. The fringes of the spectrum shift because of the laser-induced phase shift (*cf.* figure 54). Everything occurs like if the delay between the reference and the probe pulses has changed, being $\tau_2 = \tau_1 + \dfrac{\Delta\phi}{\omega}$.

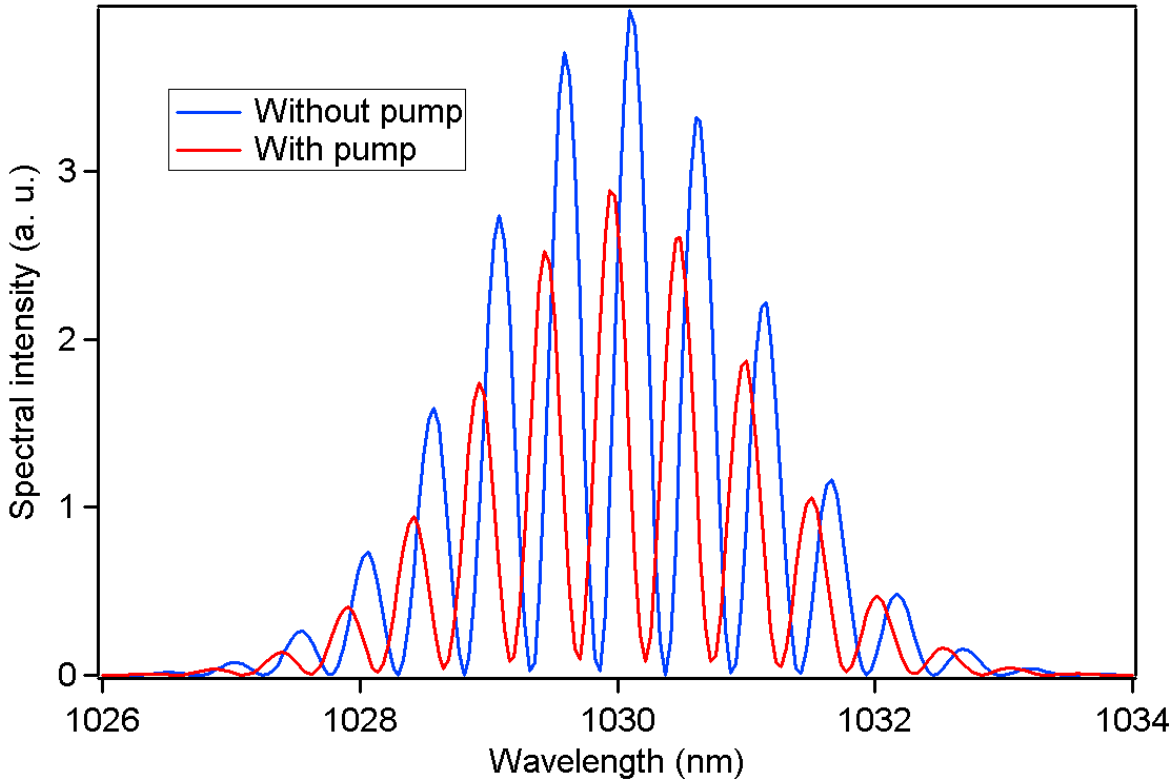

Figure 54: Simulation of the spectral interferences without and with the pump pulse. The simulation was performed with the following parameters: λ_0 = 1030 nm, τ_I = 6.8 ps, T = 0.5, $\Delta\phi$ = -2.7 rad.

The refractive index change and the laser-induced phase shift are respectively given by

$$\Delta n = n_{with\ pump} - n_{without\ pump} \approx n_2 I_{pump} - \frac{1}{2n_0}\frac{\omega_P^2 \tau_c^2}{1+\omega^2\tau_c^2} \tag{B.9.9}$$

$$\Delta\phi = \frac{2\pi L}{\lambda_0}\Delta n \approx \frac{2\pi L}{\lambda_0}\left(n_2 I_{pump} - \frac{1}{2n_0}\frac{\omega_P^2 \tau_c^2}{1+\omega^2\tau_c^2}\right) \tag{B.9.10}$$

where L is the interaction length.

Thus, by measuring the laser-induced phase shift, one can extract the free electron density as follow

$$N_C = 2n_0 N_{cr}\left(n_2 I_{pump} - \frac{\lambda_0}{2\pi L}\Delta\phi\right) \tag{B.9.11}$$

The phase shift is measured from a channeled spectrum with the following formula

$$\left.\begin{aligned} \omega\tau_2 &= \omega\tau_1 + \Delta\phi \\ \tau_1 &\approx \frac{\overline{\lambda_0}^2}{c\Delta\lambda_1} \\ \tau_2 &\approx \frac{\overline{\lambda_0}^2}{c\Delta\lambda_2} \end{aligned}\right\} \Rightarrow \Delta\phi \approx 2\pi\overline{\lambda_0}\left(\frac{1}{\Delta\lambda_2} - \frac{1}{\Delta\lambda_1}\right) \qquad \text{(B.9.12)}$$

where $\overline{\lambda_0}$ is the central wavelength of the spectrum, $\Delta\lambda_1$ the period of the spectral fringes (without pump) and $\Delta\lambda_2$ the period of the spectral fringes (with pump). Since $\Delta\lambda_1$ and $\Delta\lambda_2$ have too close values to be measured, the fringe shift $\Delta\lambda$ will be measured instead

$$\left.\begin{aligned} \Delta\lambda_1 &\rightarrow 2\pi \; rad \\ \Delta\lambda &\rightarrow \Delta\phi = \frac{2\pi\Delta\lambda}{\Delta\lambda_1} \end{aligned}\right\} \Rightarrow \Delta\lambda = \frac{\Delta\phi\Delta\lambda_1}{2\pi} \qquad \text{(B.9.13)}$$

The spectral interferometry experimental setup is described in figure 55. The t-Pulse 500 laser is used in this experiment. The energy and the repetition rate are adjusted with an acousto-optic modulator at 0.1 µJ and 200 Hz, respectively. A pump pulse and a probe pulse orthogonally polarized are generated via an interferometer containing two polarizing beam splitter cubes. A KDP crystal is inserted in the probe arm, with its slow and fast axes oriented at 45° from the probe polarization. Thus, two pulses are generated with a fixed delay $\tau_1 = \frac{l(n_E - n_O)}{c}$, where l is the length of the crystal, n_O and n_E the ordinary and extraordinary refractive indices, respectively. At the output of the interferometer, the sequence of the three pulses is focused into the sample 200 µm below the surface with a reflection microscope objective (*NA* = 0.52, *working distance* = 1.5 mm) and recollimated with another identical objective. The pump pulse is then ejected with a Glan polarizer and the reference and probe pulses are analyzed via a spectrometer (Triax 550 from HORIBA Jobin Yvon). The pump energy is about 0.1 µJ and the reference and probe energy is about 10 nJ. The sample is moved at 1 mm.s^{-1} during the irradiation to present a new spot for each laser

shot. Thus, it is a real time measurement, as opposed to a post-mortem measurement. The time separation τ_1 between the reference and the probe pulses is about 6.8 ps and the pump delay τ is changed from 0 to 1.2 ps by 100 fs steps.

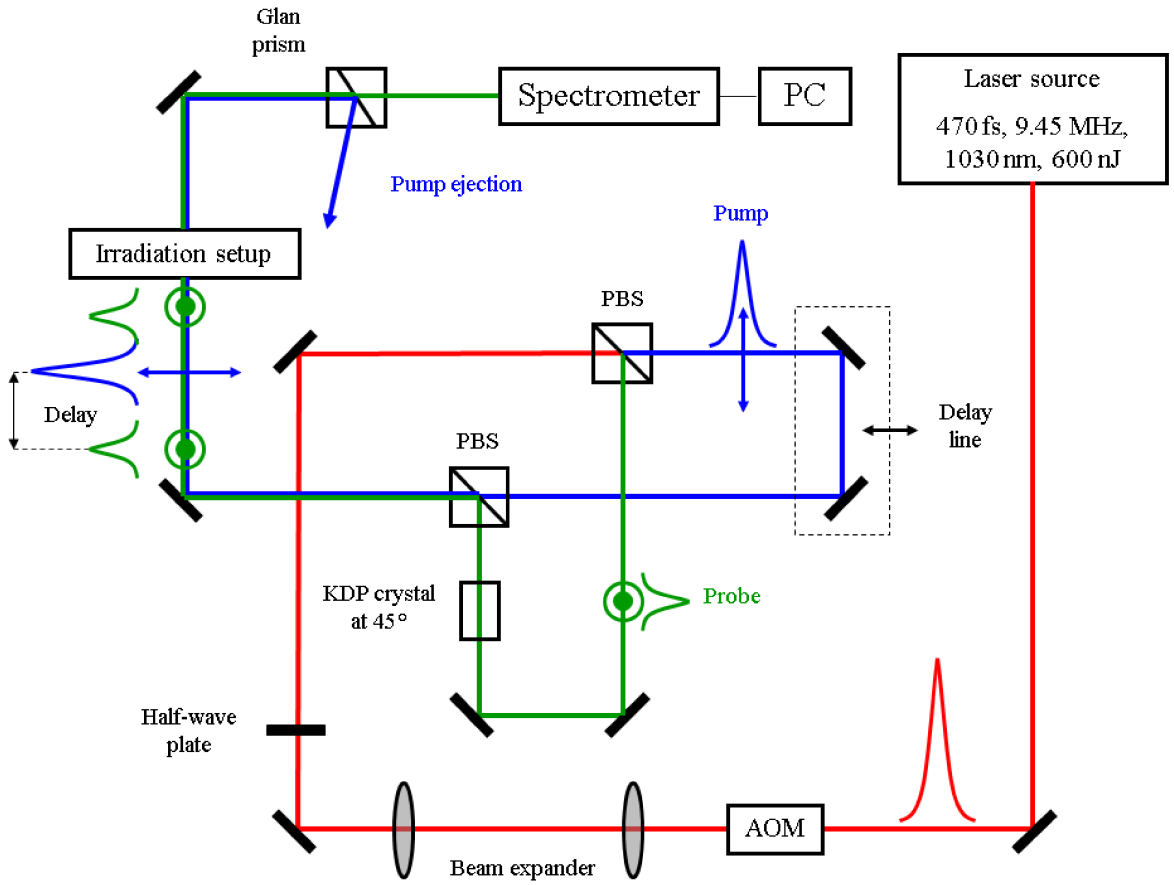

Figure 55: Spectral interferometry experimental setup. AOM: Acousto-optic modulator, PBS: Polarizing beam splitter, PC: Personal computer.

For each delay, the channeled spectrum has been acquired and the fringe shift compared to the reference spectrum has been measured. Figure 56 shows the reference (without pump) and the zero delay (with pump) channeled spectra and figure 57 the measured fringe shift for each delay. The fringe shift is between 0.027 and 0.110 nm, from which a free electron density of about 10^{19} cm^{-3} has been estimated, two orders of magnitude below the critical electron density $N_{cr} = 1.05 \times 10^{21}$ cm^{-3}. The evolution of the fringe shift versus the pump-probe delay looks constant (within the uncertainty of the measurements), contrasting

with similar works reported in the literature [Aud94] [Mar97], in which the phase shift is positive at zero delay, decreases to become negative at about 200 fs, and finally increases to be null at about 600 fs.

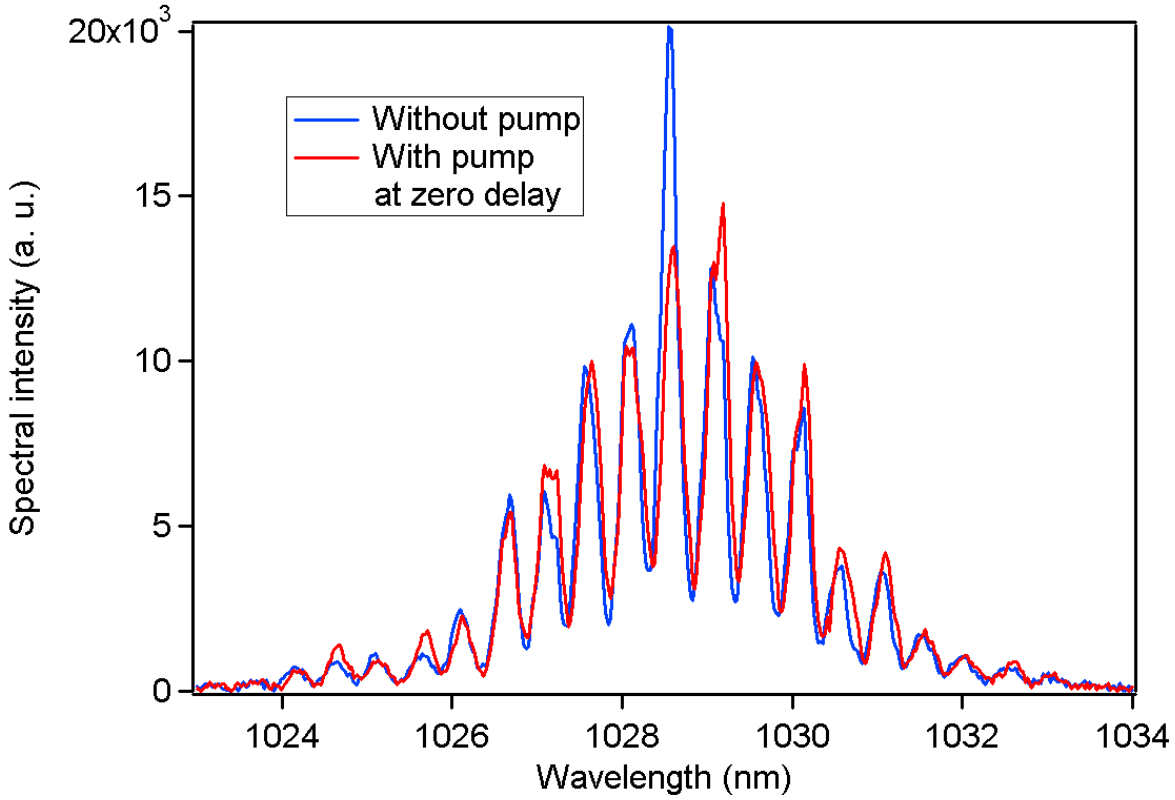

Figure 56: Channeled spectra without and with at zero delay the pump pulse.

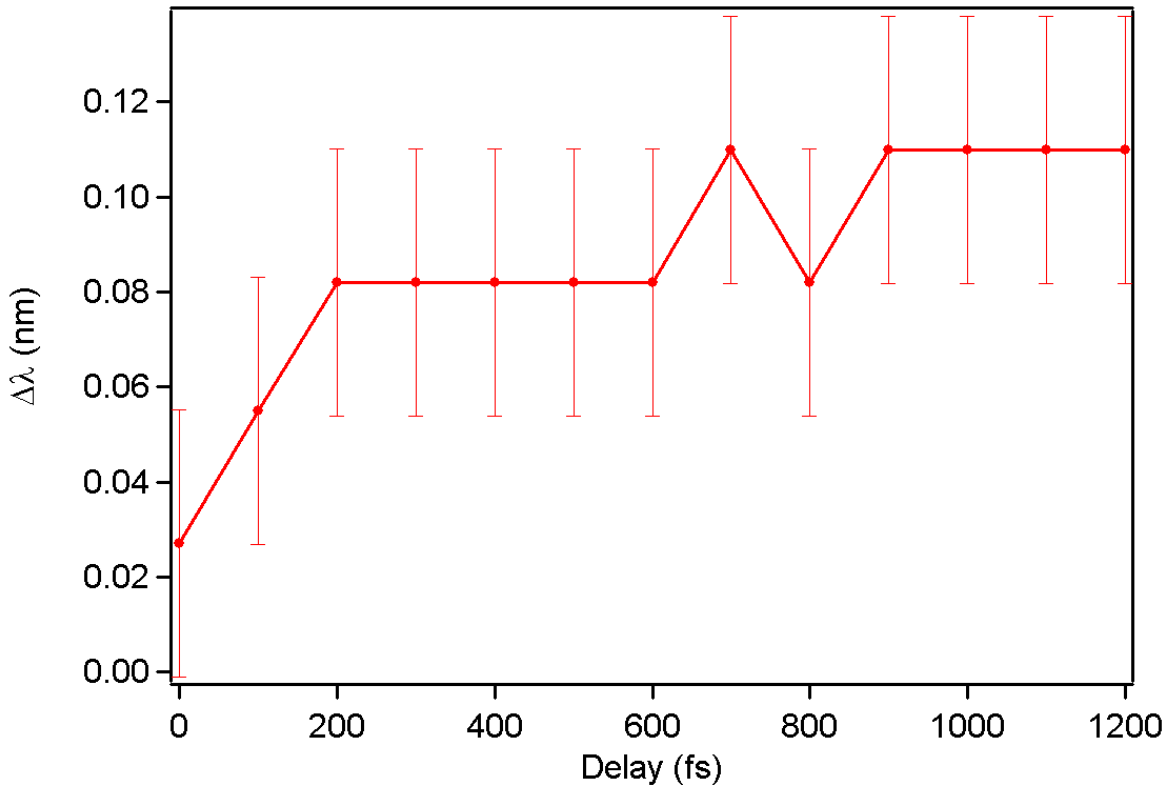

Figure 57: Evolution of the fringe shift versus the delay between the pump and the probe pulses.

This experiment allows us to get an estimated rather than accurate value of the free electron density for different reasons. Indeed, the high uncertainty related to the number of pixels of the CCD camera and the resolution of the spectrometer limits the sensitivity of the measurement to $\lambda_0/18$. The small interaction length (~ 10 µm) leads to a small phase shift and then to a small fringe shift, comparable to the uncertainty of the measurement.

9.5.3. Transient absorption experiment

Another way to measure the free electron density is by exploiting the imaginary part of the complex refractive index given by equation (B.9.6). The change in the absorption coefficient is given by

$$\Delta\alpha = \frac{2\omega}{c}\left(\kappa_{with\ pump} - \kappa_{without\ pump}\right) \approx \frac{\omega_P^2 \tau_c}{c n_0 \left(1+\omega^2\tau_c^2\right)} \tag{B.9.14}$$

From the previous equation, one can deduce the Fresnel transmission coefficient, given by

$$T = \frac{I(L)}{I_0} = \exp(-\Delta\alpha L) = \exp\left(-\frac{\omega_P^2 \tau_c}{c n_0 \left(1+\omega^2\tau_c^2\right)} L\right) \tag{B.9.15}$$

Thus, by measuring the Fresnel transmission coefficient, one can extract the free electron density as follow

$$N_C = \frac{c n_0 \varepsilon_0 m_e}{e^2 \tau_c L}\left(1 + \frac{4\pi^2 c^2 \tau_c^2}{\lambda_0^2}\right)\ln\left(\frac{1}{T}\right) \tag{B.9.16}$$

The transient absorption experimental setup is described in figure 58. The t-Pulse 500 laser is used in this experiment. An acousto-optic modulator is used to adjust the number and/or the energy of the pulses. A pump pulse and a probe pulse orthogonally polarized are generated via an interferometer containing two polarizing beam splitters. A mechanical chopper modulates the pump beam at 1.5 kHz. A BBO crystal is inserted in the probe arm to generate the second harmonic of the laser (*i.e.* 515 nm). At the output of the interferometer, the sequence of the two pulses is focused into a fixed sample, 200 µm below the surface, with a reflection microscope objective (*NA* = 0.52, *working distance* = 15 mm) and recollimated with another identical objective. The beam waist is estimated to be 1 µm. The pump pulse is blocked with a pinhole combined to a prism and a green colored filter. The probe pulse is analyzed via a photodiode and a lock-in amplifier connected to the chopper. The data are collected with a computer. The delay line was moved over a distance corresponding to a 14 ps pump-probe delay during 1 s. Thus, the number of pulses on the sample for each acquisition was about 5×10^6. The pump irradiance was varied from 2 to 11 TW.cm^{-2} and the probe irradiance was about 10 GW.cm^{-2}. The temporal resolution of our experiment, defined as the

cross-correlation of the pump and probe pulses, is about 700 fs. The irradiance is computed assuming a Gaussian spatial profile and a rectangular temporal profile of the laser beam.

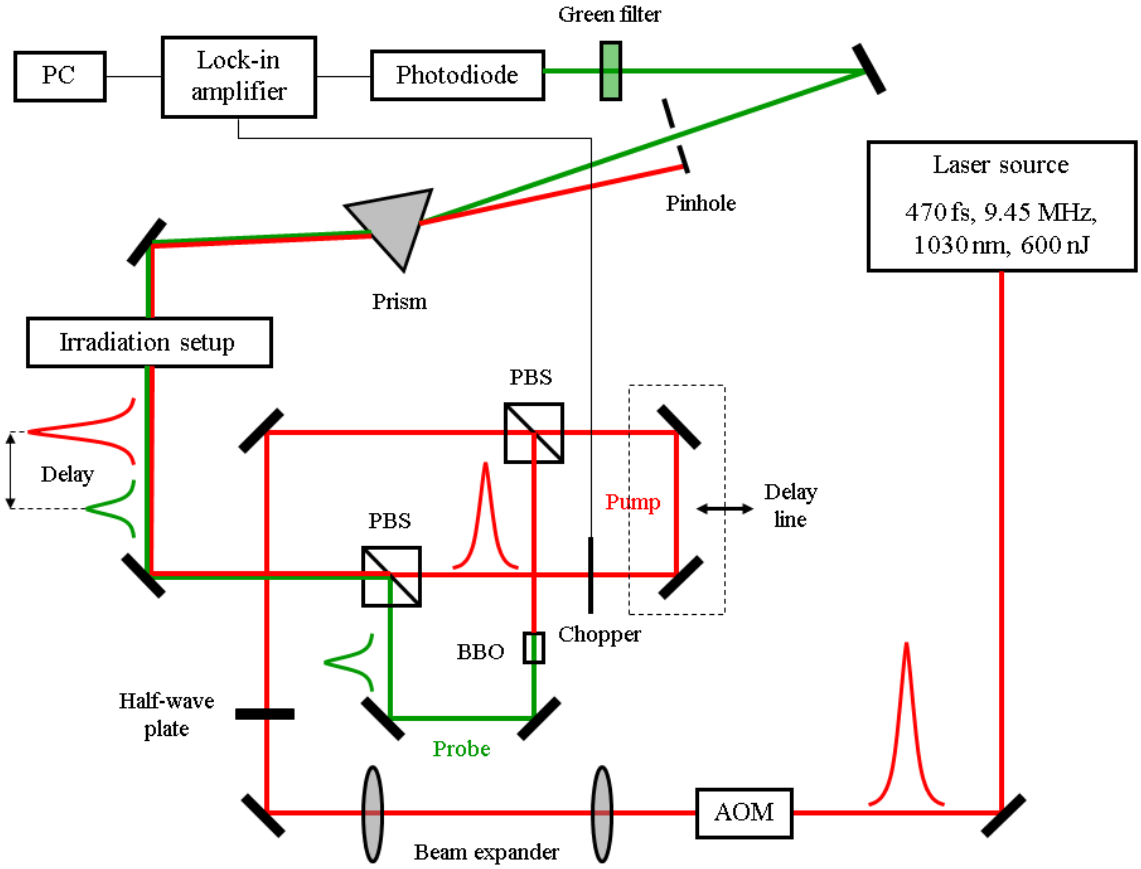

Figure 58: Transient absorption experimental setup. AOM: Acousto-optic modulator, PBS: Polarizing beam splitter, BBO: β-barium borate doubling crystal, PC: Personal computer.

A typical temporal dynamic of the induced absorption for a pump irradiance of 7.3 $TW.cm^{-2}$ is shown in figure 59. No absorption is present after 1.8 ps. Nevertheless, the temporal resolution of our experiment does not permit to reveal details below 700 fs. The absorption offset, which is about 0.05% at 7.3 $TW.cm^{-2}$, is probably due to thermal cumulative effects associated to the high repetition rate of the laser.

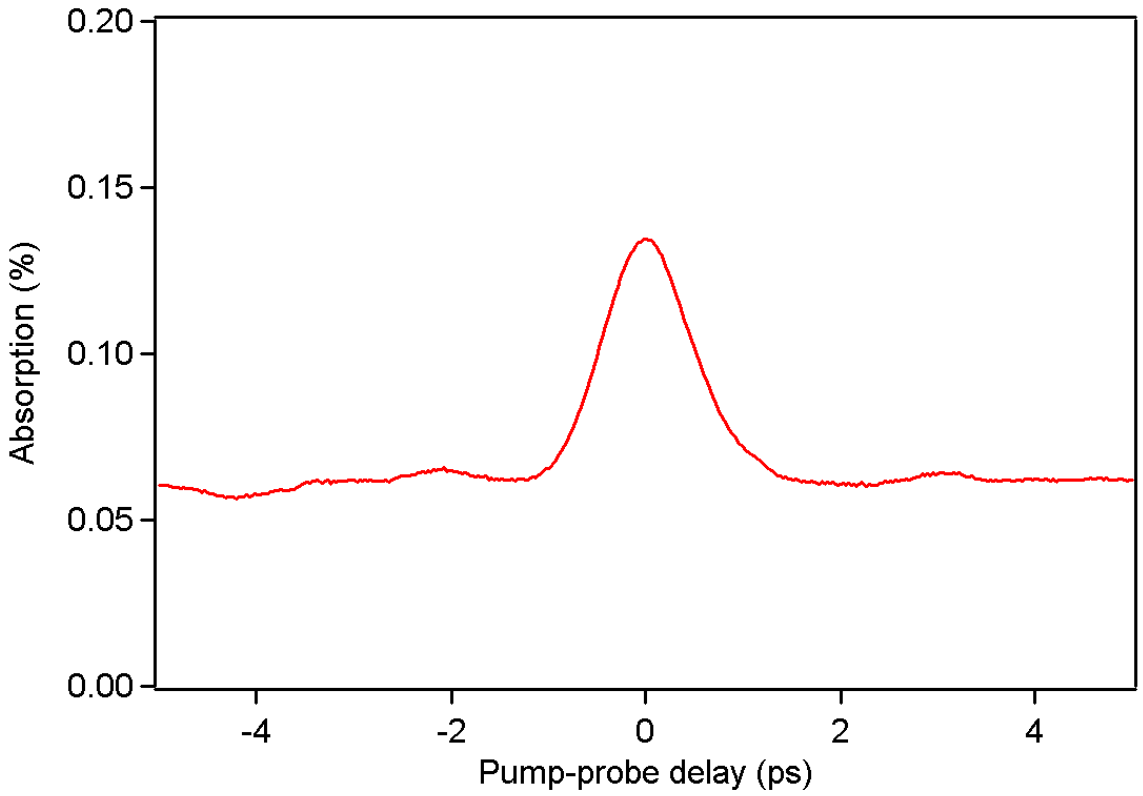

Figure 59: Evolution of the induced absorption versus the pump-probe delay for a pump irradiance of 7.3 TW.cm^{-2}. The curve is an average of 30 acquisitions. The standard deviation of these acquisitions gives an uncertainty of the measurements of 40%.

The maximum absorption measured at zero delay as a function of the pump irradiance is given in figure 60. In a multiphoton absorption regime, the absorption should scale as $Abs(I) \propto I^k$, where k is the order of the multiphoton process and I the irradiance. A fit with $k = 4$ gives a good agreement with the experimental data and provides a clear evidence of four-photon absorption as the photo-ionization mechanism involved in the nanostructuring of the silver zinc phosphate glass.

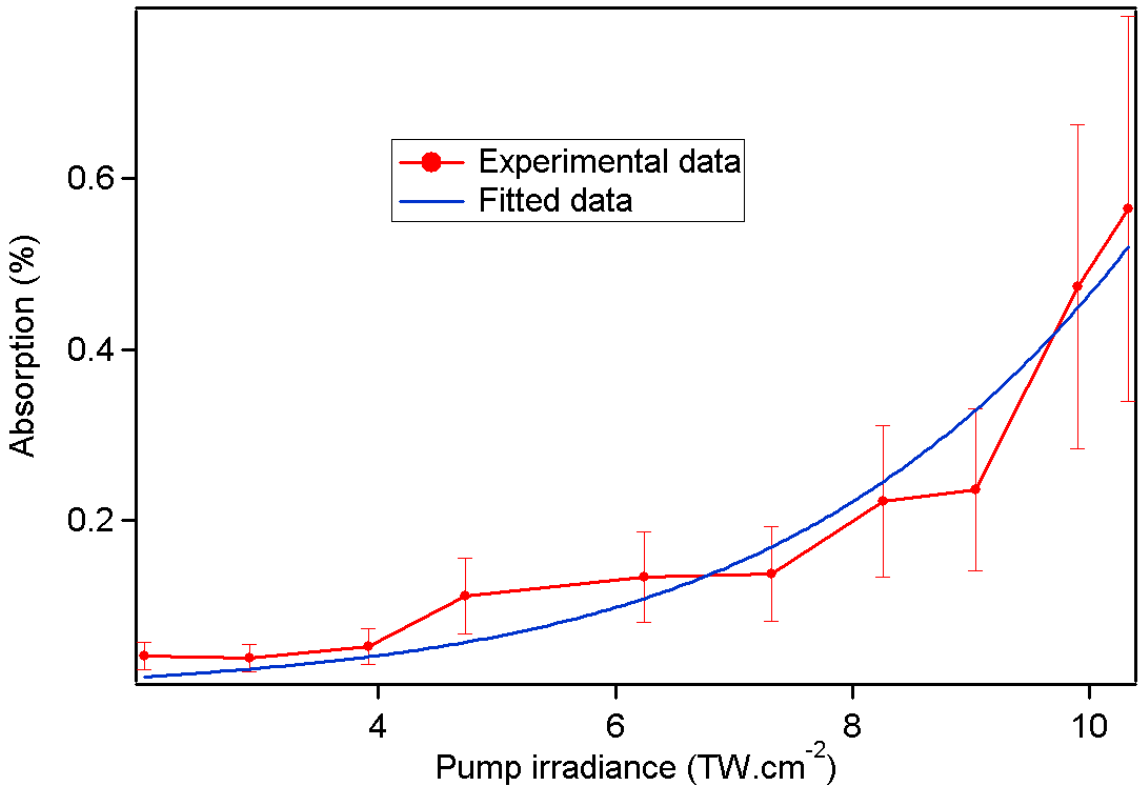

Figure 60: Evolution of the induced absorption versus the pump irradiance at the sample. The error bars are 40% of the experimental values.

Using equation (B.9.16) with $n_0 = 1.58$, $\tau_c = 0.4\,\text{fs}$ [Tem06], $L = 10\,\mu\text{m}$, $\lambda_0 = 1030\,\text{nm}$ and $T = 1 - Abs$, the free electron density has been computed (*cf.* figure 61). It ranges from 0.2 to 3 × 10^{17} cm^{-3}, and is four orders of magnitude below the critical electron density, which is about 10^{21} cm^{-3} at the laser wavelength. It is also two orders of magnitude below the free electron density reported in the literature for fused silica, *i.e.* 10^{19} cm^{-3}, for almost the same irradiance [Tem06].

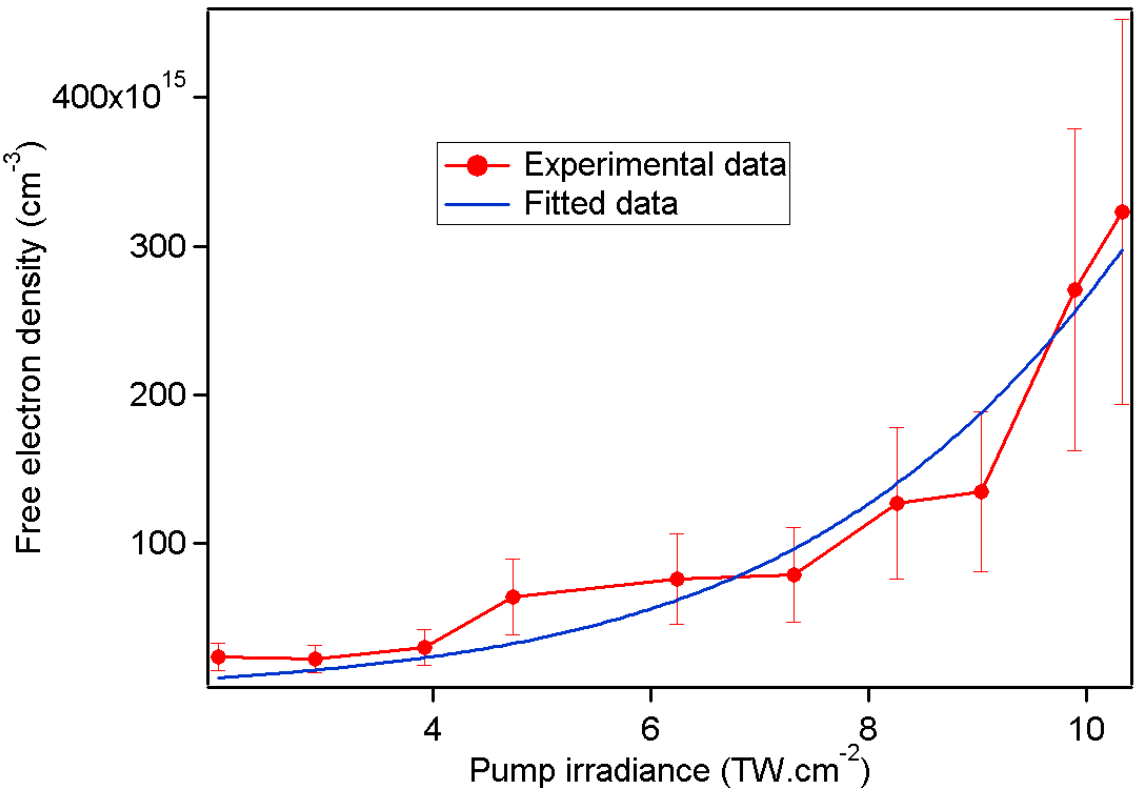

Figure 61: Evolution of the free electron density versus the pump irradiance at the sample. The error bars are 40% of the experimental values.

Even if we expected a free electron density lower for our glass than for fused silica, it is surprising to observe such a big difference between the two measurements. Two reasons can explain this discrepancy. First, although the irradiances are comparable, the pulse energies used in both experiments are very different, as low as 80 nJ for our glass, and about 400 nJ for fused silica [Tem06]. Second, the number of pulses hitting the sample due to the high repetition rate of our laser significantly plays a role in the formation of the silver clusters.

9.6. Cumulative effect investigation by THG microscopy

We have seen that the formation of silver clusters in the silver zinc phosphate glass is strongly correlated to the thermal diffusion and therefore to pulse after pulse cumulative effects. In order to investigate these cumulative effects, we propose to use THG microscopy.

This technique is appropriate for this kind of study because the third-harmonic is generated at the vicinity of interfaces. As the clusters are formed, an interface is created. By analyzing the third-harmonic signal emitted with respect to the number of pulses hitting the glass, information about the dynamic of the formation of silver clusters can be obtained.

The t-Pulse 500 laser is used in this experiment. The pulses are focused into a fixed sample, 200 µm below the surface, with a reflection microscope objective (*NA* = 0.52, *working distance* = 15 mm). The fundamental and third-harmonic beams are collected with another identical objective. The fundamental beam is filtered and the third-harmonic beam is analyzed with a PM tube linked to a digital oscilloscope. The beam waist is estimated to be 1 µm. A lock-in amplifier at the laser repetition rate is used to increase the signal/noise ratio. The pump irradiance was varied from 2 to 12 TW.cm^{-2}. The irradiance is computed assuming a Gaussian spatial profile and a rectangular temporal profile of the laser beam.

Figure 62 presents the evolution of the THG signal versus the number of pulses (from 0 to 1.2×10^7 pulses) hitting the sample for different irradiances, from 1.55 to 12.21 TW.cm^{-2}. Figure 63 is a zoom of figure 62, for pulses ranging from 0 to 8×10^5. Results show a THG threshold at about 7 TW.cm^{-2}, below the refractive index change threshold at 9 TW.cm^{-2}.

For irradiances up to 8.86 TW.cm^{-2}, two tendencies of the evolution of the THG signal are observed: first an increase until 10^6 pulses, and then a slight decrease. The first part of this evolution can easily be explained. As the number of pulses increases, the number of photo-induced clusters increases, leading to a larger change in its optical properties with respect to the bulk and therefore to an enhancement of the THG signal. The second part of the evolution is more difficult to explain. It can be due to several reasons. After 10^6 pulses, the glass starts to be damaged and the third-harmonic is scattered. As a result, less third-harmonic is collected by the PMT, and the THG signal is artificially reduced. Another cause would be that, the

combination of the change in the refractive index/change in the third-order susceptibility after 10^6 pulses is such that the THG signal decreases.

For irradiances at 8.86 TW.cm^{-2}, the THG signal increases until 10^6 pulses and then saturates. The irradiance is not high enough to induce damage in the glass, and therefore, once all the available Ag^+ ions are consumed after 10^6 pulses and the clusters are formed, the THG signal remains constant.

For irradiances at 7.31 TW.cm^{-2}, the THG signal increases with the number of pulses. The irradiance is not high enough to consume all the available Ag^+ ions within our pulse range. Therefore, silver clusters are created but their concentration and the change in their optical properties are not optimal.

For irradiances down to 7.31 TW.cm^{-2}, the THG signal is within the measurement noise. The silver cluster formation threshold is not reached.

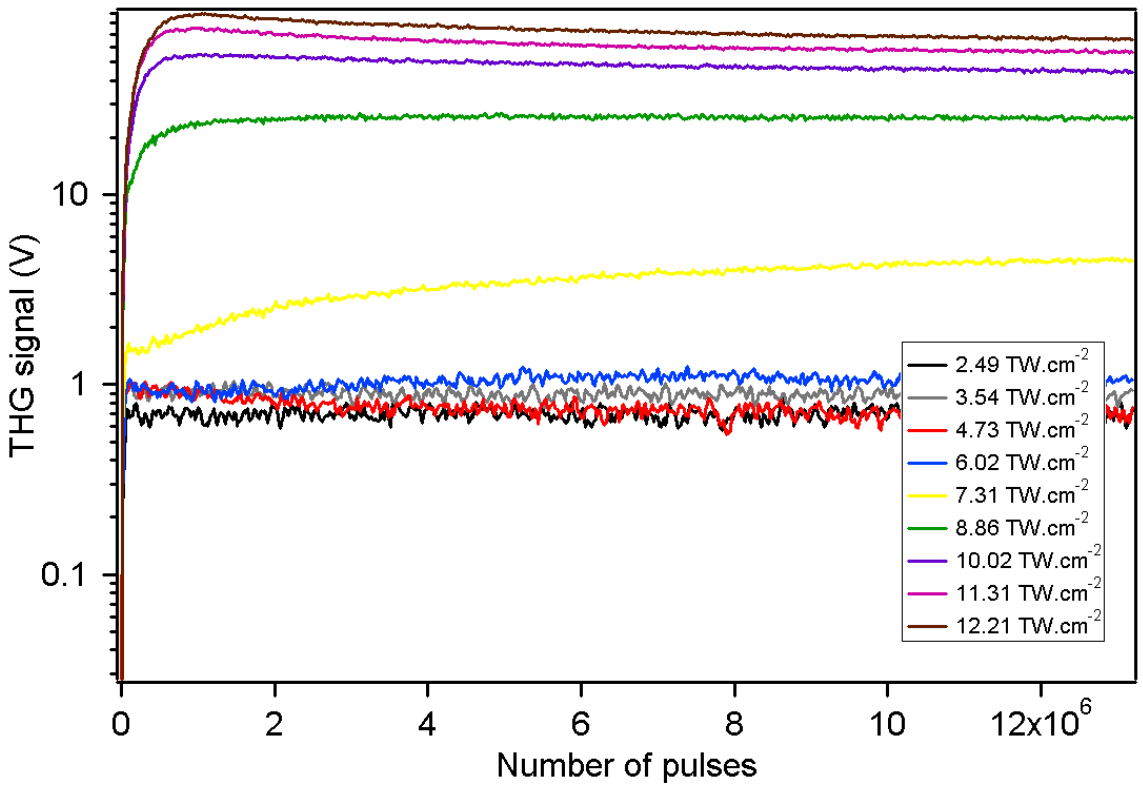

Figure 62: Evolution of the THG signal (in log scale) versus the number of pulses (from 0 to 1.2×10^7) hitting the glass.

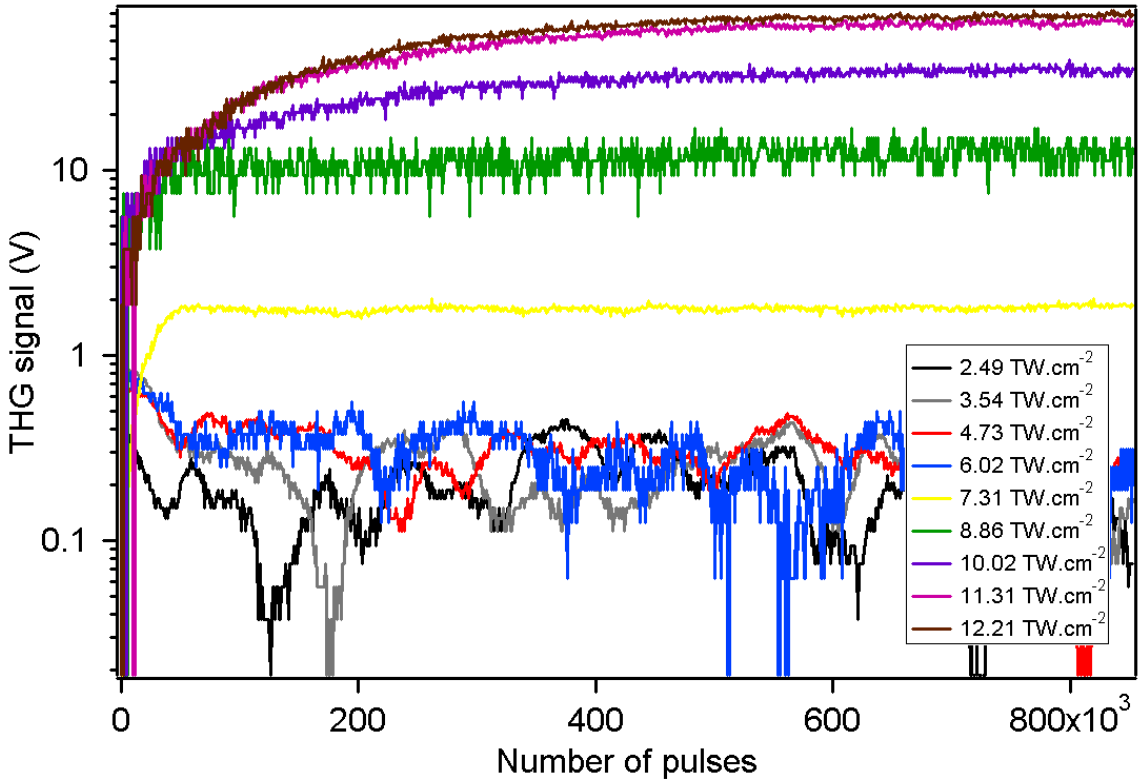

Figure 63: Evolution of the THG signal (in log scale) versus the number of pulses (from 0 to 8×10^5) hitting the glass.

The same experiment was performed with circular polarization using a quarter wave plate before the focusing element. Let remind us that THG with circularly polarized beams gives information about the symmetry properties of the material. In our case, no significant third-harmonic is detected when the incident laser beam is circularly polarized. Therefore, the photo-induced clusters are isotropic.

To conclude about the influence of the cumulative effects in this glass with this laser, 10^6 pulses seems to be the limit value for the consumption of all the available Ag^+ ions in the exposed area for irradiances higher than 7.31 TW.cm^{-2}. After 10^6 pulses and for irradiances up to 8.86 TW.cm^{-2}, the glass becomes damaged. Thus, to get the maximal amount of non-damaged silver clusters, one would work below 8.86 TW.cm^{-2} and 10^6 pulses.

9.7. Summary

In summary, in this chapter, several oxide glasses have been exposed to femtosecond pulses. Following exposure, each glass responds in a different way:

- The sodium-borophosphate glass containing 9.55% of niobium oxide presents micro-cracks and nanocrystallites.

- The silicate glass reveals nanogratings, like in fused silica, with a period on the order of magnitude of $\lambda_0/2n$.

- The same silicate glass, but containing 1.27% of silver, behaves differently; it exhibits fluorescent ring structures when the repetition rate of the laser is high enough (1 MHz) to enable cumulative thermal effects to take place. On the contrary, when the repetition rate of the laser is too low (100 kHz) for thermal effects to occur, fluorescent arbitrary shape structures are created.

- The zinc phosphate glass containing 4% of silver has been studied more in detail. This glass presents, as in the case of the silver-doped silicate, fluorescent ring structures. This ring is composed of photo-induced silver clusters and has a thickness on the order of 80 nm, well below the diffraction limit usually achieved in 3D laser direct writing. The free electron density has been measured; it is on the order of 10^{17} cm^{-3} and is four orders of magnitude below the critical density 10^{21} cm^{-3}. This measurement can be compared to values reported in the literature for fused silica [Aud94] [Tem06] [Pap07]. In these studies, values of free electron density are on the order of 10^{19} cm^{-3} and our measurement is still two orders of magnitude below this level. Thus, we can conclude that, during the irradiation, we do not create a plasma but an electron gas. Four-photon absorption has been found to the ionization mechanism in this glass. The influence of thermal cumulative effects has also been studied for this glass. The results show that these effects are of large importance in the structuring of this

glass; the laser repetition rate must be higher than 1 MHz and the number of pulses hitting the sample less than 10^6 for irradiances below 8.86 $TW.cm^{-2}$.

CHAPTER TEN: CONCLUSION AND PERSPECTIVES

In conclusion, this dissertation summarizes findings on nonlinear optical characterization and femtosecond laser structuring of different oxide glasses. Within the context of the Born-Oppenheimer approximation, the electronic and nuclear nonlinear optical properties of two glass families, fused silica and sodium-borophosphate niobium oxide containing, have been measured. Their relative weight to the total nonlinearity has been determined. Fused silica exhibits a maximal nuclear contribution on the order of 6% in our particular experimental conditions. In parallel, the maximal nuclear contribution in the sodium-borophosphate glass containing 38.78% of niobium oxide is ten times higher, on the order of 60%. This latter glass confirms to be a good candidate as a Raman amplifier. Moreover, since the nuclear contribution strongly depends on the laser pulse duration, the total nonlinearity of this glass can be modulated by adjusting this parameter.

In this dissertation, we bring our contribution to the understanding on femtosecond laser structuring in glasses. In particular, three commercially available fused silica samples presenting different fabrication conditions (therefore distinct impurity levels) have been irradiated with a near infrared femtosecond laser. The photo-induced structures have been identified by means of several spectroscopic techniques, which have revealed the formation of color centers and a densification. Their linear (refractive index) and nonlinear (third-order susceptibility) properties have been measured and the “nanogratings” behavior at a subwavelength scale has been observed.

In addition to fused silica, several oxide glasses presenting very distinct chemical compositions have been studied. Each of these glasses has responded in a different way to femtosecond laser exposure. The sodium-borophosphate glass containing niobium oxide exhibited micro-cracks and nano-crystallites. The silicate glass revealed “nanograting”

structures. The same glass but silver containing showed fluorescent ring structures. The zinc phosphate glass containing silver presented too fluorescent ring structures, with a size on the order of 80 nm, well below the diffraction limit. This latter glass was chosen to study in details the involved effects in laser-glass interaction. It was found that the absorption mechanism of the laser energy for this glass is four-photon absorption. The generated free electron density was measured, on the order of 10^{17} cm^{-3}. This permitted to conclude that an electron gas rather than a plasma was formed during the laser irradiation.

The zinc phosphate silver containing glass is of particular interest. Various properties of the photo-induced structures in this glass could be exploited in the photonics and plasmonics fields. As an example, the silver clusters exhibit strong nonlinearities without modifying the linear refractive index. Thus, efficient 3D optical data storage can be realized in the glass [Can08]. The silver clusters, distributed in an area below the diffraction limit, are local fluorescent emitters. Moreover, silver clusters can agglomerate into nanoparticles following thermal treatment. The latter exhibit many properties, such as plasmon resonance absorption, local field enhancement, local refractive index modification, etc… Designing 3D nanostructures containing nanoparticles offers a new alternative for the fabrication of 3D photonics crystals, metamaterials and plasmonic devices.

APPENDIX A: INTER-UNIVERSITY AGREEMENT ON JOINT DOCTORATE SUPERVISION BETWEEN UNIVERSITY OF BORDEAUX 1 AND UNIVERSITY OF CENTRAL FLORIDA

University of Bordeaux 1 recognizes the validity of the thesis and therefore awards
le grade de docteur de l'Université Bordeaux 1

par Arnaud ROYON

Spécialité : Lasers, Matière et Nanosciences

This thesis is under the joint supervision of:

- at the University of Bordeaux 1:

Dr. Lionel CANIONI	Professor (Optics and Physics)
And Dr. Laurent SARGER	Professor (Optics and Physics)

- at the University of Central Florida:

Dr. Martin C. RICHARDSON	Professor (Optics and Physics)
And Dr. David J. HAGAN	Professor (Optics and Physics)

APPENDIX B: RESUME

La structuration laser femtoseconde en trois dimensions rencontre un intérêt grandissant du fait de sa facilité de mise en œuvre et des nombreuses applications qu'elle peut couvrir dans le domaine des composants photoniques. Des structures telles que des guides d'onde, des réseaux de diffraction, des mémoires optiques ou des cristaux photoniques peuvent être fabriquées grâce à cette technique. Son emploi sur des verres oxydes est prometteur car ces derniers présentent des avantages certains ; ils sont très résistants au flux et au vieillissement, leur composition chimique peut être changée facilement afin de s'adapter à un cahier des charges précis. On les retrouve déjà dans les amplificateurs Raman, les fibres optiques, les lasers à fibres, etc…

Le travail de cette thèse s'articule autour de deux grands axes. Le premier axe consiste à caractériser les propriétés optiques linéaires et non-linéaires de matériaux vitreux massifs afin d'optimiser leur composition en vue d'une application particulière. Dans ce contexte, les propriétés optiques non-linéaires, leurs origines physiques (électronique et nucléaire) ainsi que leurs temps de réponse caractéristiques (de quelques femtosecondes à quelques centaines de picosecondes) sont décrits dans le cadre de l'approximation de Born-Oppenheimer. Ainsi, la silice fondue et plusieurs verres sodo-borophosphates contenant différentes concentrations en oxyde de niobium ont été étudiés. Les résultats montrent que les propriétés optiques non-linéaires dans la silice fondue sont majoritairement d'origine électronique, alors que dans les verres sodo-borophosphates, la contribution d'origine nucléaire peut devenir prépondérante lorsque la concentration en oxyde de niobium dépasse 30%.

Le second axe s'articule autour de la structuration des matériaux. Trois échantillons commerciaux de silice fondue présentant des conditions de fabrication différentes (donc des taux d'impuretés distincts) et irradiés avec un laser femtoseconde proche infrarouge ont été

étudiés. Les défauts induits par laser ont été identifiés au moyen de plusieurs techniques de spectroscopie. Elles ont montré la formation de centres colorés ainsi qu'une densification au niveau de la zone irradiée. Leurs propriétés optiques linéaire (indice de réfraction) et non-linéaire (susceptibilité du troisième ordre) ont été mesurées. De plus, la structuration de la silice fondue à l'échelle sub-micrométrique sous forme de « nano-réseaux » est observée et la biréfringence de forme induite par ces structures est discutée.

En plus des échantillons de silice fondue, plusieurs verres oxydes présentant des compositions chimiques très distinctes ont été étudiés. Un verre sodo-borophosphate contenant de l'oxyde de niobium exhibe des micro-craquelures et des nano-crystallites après irradiation. Un verre silicate contenant ou non de l'argent dévoile des structures en anneau fluorescentes ou en « nano-réseaux ». Un verre zinc phosphate contenant de l'argent présente lui aussi des structures en anneau fluorescentes, d'une taille de l'ordre de 80 nm, bien inférieure à la limite de diffraction. Des techniques pompe-sonde sous microscope ont été mises en œuvre sur ce dernier verre pour étudier l'interaction laser-verre. Le mécanisme d'absorption de l'énergie lumineuse pour ce verre est l'absorption à quatre photons. La densité d'électrons libres générée est de l'ordre de 10^{17} cm^{-3}, ce qui permet de conclure qu'un gaz d'électrons plutôt qu'un plasma se forme pendant l'irradiation laser.

LIST OF REFERENCES

[Abe00] J. E. Aber, M. C. Newstein and B. A. Garetz, *"Femtosecond optical Kerr effect measurements in silicate glasses"*, Journal of the Optical Society of America B **17**, 120-127 (2000).

[Ams08] M. Ams, G. D. Marshall, P. Dekker, M. Dubov, V. K. Mezentsev, I. Bennion and M. J. Withford, *"Investigation of ultrafast laser–photonic material interactions: challenges for directly written glass photonics"* (2008).

[Aud94] P. Audebert, Ph. Daguzan, A. Dos Santos, J. C. Gauthier, J. P. Geindre, S. Guizard, G. Hamoniaux, K. Krastev, P. Martin, G. Petite and A. Antonetti, *"Space-Time Observation of an Electron Gas in SiO_2"*, Physical Review Letters **73**, 1990-1993 (1994).

[Bar97] Y. Barad, H. Eisenberg, M. Horowitz and Y. Silberberg, *"Nonlinear scanning laser microscopy by third harmonic generation"*, Applied Physics Letters **70**, 922-924 (1997).

[Bar02] R. Barille, L. Canioni, L. Sarger and G. Rivoire, *"Nonlinearity measurements of thin films by third-harmonic-generation microscopy"*, Physical Review E **66**, 067602 (2002).

[Bha06] V. R. Bhardwaj, E. Simova, P. P. Rajeev, C. Hnatovsky, R. S. Taylor, D. M. Rayner and P. B. Corkum, *"Optically Produced Arrays of Planar Nanostructures inside Fused Silica"*, Physical Review Letters **96**, 057404 (2006).

[Blo06] D. Blömer, A. Szameit, F. Dreisow, T. Schreiber, S. Nolte and A. Tünnermann, *"Nonlinear refractive-index of fs-laser-written waveguides in fused silica"*, Optics Express **14**, 2151-2157 (2006).

[Bor99] M. Born and E. Wolf, *"Principles of Optics"*, 7th edition, Cambridge University Press (1999).

[Bou80] A. Boudou and J. Sapriel, *"Raman-scattering investigations in tetragonal tungsten bronze compounds. I. $Ba_2NaNb_5O_{15}$ and related crystals"*, Physical Review B **21**, 61-69 (1980).

[Bou03] E. Bouziane, M. D. Fontana and M. Ayadi, *"Study of the low-frequency Raman scattering in $NaNbO_3$ crystal"*, Journal of Physics: Condensed Matter **15**, 1387-1395 (2003).

[Boy99] R. W. Boyd, *"Topical review: Order-of-magnitude estimates of the nonlinear optical susceptibility"*, Journal of Modern Optics **46**, 367-378 (1999).

[Boy07] R. W. Boyd, "*Nonlinear Optics"*, 3rd edition, Academic Press (2007).

[Bri04] E. Bricchi, B. G. Klappauf and P. G. Kazansky, *"Form birefringence and negative index change created by femtosecond direct writing in transparent materials"*, Optics Letters **29**, 119-121 (2004).

[Bro05] A. Brocas, *"Microscopies non-linéaires : Analyses et Instrumentations"*, Thesis, University of Bordeaux 1, France (2005).

[Buc96] E. L. Buckland and R. W. Boyd, *"Electrostrictive contribution to the intensity-dependent refractive index of optical fibers"*, Optics Letters **21**, 1117-1119 (1996).

[But90] P. N. Butcher and D. Cotter, *"The Elements of Nonlinear Optics"*, Cambridge University Press (1990).

[Can08] L. Canioni, M. Bellec, A. Royon, B. Bousquet and T. Cardinal, *"Three-dimensional optical data storage using third-harmonic generation in silver zinc phosphate glass"*, Optics Letters **33**, 360-362 (2008).

[Car96] T. Cardinal, E. Fargin, G. Le Flem, M. Couzi, L. Canioni, P. Segonds, L. Sarger, A. Ducasse and F. Adamietz, *"Nonlinear optical properties of some niobium (V) oxide*

glasses", European Journal of Solid State and Inorganic Chemistry **33**, 597-605 (1996).

[Car97] T. Cardinal, E. Fargin, G. Le Flem and S. Leboiteux, *"Correlations between structural properties of Nb_2O_5-$NaPO_3$-$Na_2B_4O_7$ glasses and non-linear optical activities"*, Journal of Non-Crystalline Solids **222**, 228-234 (1997).

[Cha03] J. W. Chan, T. R. Huser, S. H. Risbud, J. S. Hayden and D. M. Krol, *"Waveguide fabrication in phosphate glasses using femtosecond laser pulses"*, Applied Physics Letters **82**, 2371-2373 (2003).

[Dai07] Y. Dai, B. Zhu, J. Qiu, H. Ma, B. Lu and B. Yu, *"Space-selective precipitation of functional crystals in glass by using a high repetition rate femtosecond laser"*, Chemical Physics Letters **443**, 253-257 (2007).

[Dav96] K. M. Davis, K. Miura, N. Sugimoto and K. Hirao, *"Writing waveguides in glass with a femtosecond laser"*, Optics Letters **21**, 1729-1731 (1996).

[Ehr04] D. Ehrt, T. Kittel, M. Will, S. Nolte and A. Tünnermann, *"Femtosecond-laser-writing in various glasses"*, Journal of Non-Crystalline Solids **345 & 346**, 332-337 (2004).

[Far99] M. A. Farahani and T. Gogolla, *"Spontaneous Raman Scattering in Optical Fibers with Modulated Probe Light for Distributed Temperature Raman Remote Sensing"*, Journal of Lightwave Technology **17**, 1379-1391 (1999).

[Gai04] L. N. Gaier, M. Lein, M. I. Stockman, P. L. Knight, P. B. Corkum, M. Yu Ivanov and G. L. Yudin, *"Ultrafast multiphoton forest fires and fractals in clusters and dielectrics"*, Journal of Physics B: Atomic, Molecular and Optical Physics **37**, L57-L67 (2004).

[Gai05] L. N. Gaier, M. Lein, M. I. Stockman, G. L. Yudin, P. B. Corkum, M. Yu Ivanov and P. L. Knight, *"Hole-assisted energy deposition in dielectrics and clusters in the multiphoton regime"*, Journal of Modern Optics **52**, 1019-1030 (2005).

[Gal78] F. L. Galeener, J. C. Mikkelsen Jr., R. H. Geils and W. J. Mosby, *"The relative Raman cross sections of vitreous SiO_2, GeO_2, B_2O_3, and P_2O_5"*, Applied Physics Letters **32**, 34-36 (1978).

[Gal83] F. L. Galeener and A. E. Geissberger, *"Vibrational dynamics in ^{30}Si-substituted vitreous SiO_2"*, Physical Review B **27**, 6199-6204 (1983).

[Gat08] R. R. Gattass and E. Mazur, *"Femtosecond laser micromachining in transparent materials"*, Nature Photonics **2**, 219-225 (2008).

[Gle96] E. N. Glezer, M. Milosavljevic, L. Huang, R. J. Finlay, T.-H. Her, J. Callan and E. Mazur, *"Three-dimensional optical storage inside transparent materials"*, Optics Letters **21**, 2023-2025 (1996).

[Hei79] D. Heiman, R. W. Hellwarth and D. S. Hamilton, *"Raman scattering and nonlinear refractive index measurements of optical glasses"*, Journal of Non-Crystalline Solids **34**, 63-79 (1979).

[Hel63] R. W. Hellwarth, *"Theory of Stimulated Raman Scattering"*, Physical Review **130**, 1850-1852 (1963).

[Hel75] R. W. Hellwarth, J. Cherlow and T.-T. Yang, *"Origin and frequency dependence of nonlinear optical susceptibilities of glasses"*, Physical Review B **11**, 964-967 (1975).

[Hel77] R. W. Hellwarth, *"Third-order optical susceptibilities of liquids and solids"*, Progress in Quantum Electronics **5**, 1-68 (1977).

[Hir98] K. Hirao and K. Miura, *"Writing waveguides and gratings in silica and related materials by a femtosecond laser"*, Journal of Non-Crystalline Solids **239**, 91-95 (1998).

[Hna05] C. Hnatovsky, R. S. Taylor, P. P. Rajeev, E. Simova, V. R. Bhardwaj, D. M. Rayner and P. B. Corkum *"Pulse duration dependence of femtosecond-laser-fabricated nanogratings in fused silica"*, Applied Physics Letters **87**, 014104 (2005).

[Hul81] H. C. van de Hulst, "*Light Scattering by Small Particles"*, Dover Publications (1981).

[Kan96] I. Kang, S. Smolorz, T. Krauss, F. Wise, B. G. Aitken and N. F. Borrelli, *"Time domain observation of nuclear contributions to the optical nonlinearities of glasses"*, Physical Review B **54**, R12641-R12644 (1996).

[Kat71] Y. Kato and H. Takuma, *"Absolute Measurement of Raman-Scattering Cross Sections of Liquids"*, Journal of the Optical Society of America **61**, 347-350 (1971).

[Kat71bis] Y. Kato and H. Takuma, *"Experimental Study on the Wavelength Dependence of the Raman Scattering Cross Sections"*, The Journal of Chemical Physics **54**, 5398-5402 (1971).

[Kaz07] P. G. Kazansky, W. Yang, E. Bricchi, J. Bovatsek, A. Arai, Y. Shimotsuma, K. Miura and K. Hirao, *""Quill" writing with ultrashort light pulses in transparent materials"*, Applied Physics Letters **90**, 151120 (2007).

[Kel65] L. V. Keldysh, *"Ionization in the field of a strong electromagnetic wave"*, Soviet Physics JETP **20**, 1307-1314 (1965).

[Lip03] A. A. Lipovskii, D. K. Tagantsev, A. A. Vetrov, O. V. Yanush, *"Raman spectroscopy and the origin of electrooptical Kerr phenomenon in niobium alkali-silicate glasses"*, Optical Materials **21**, 749-757 (2003).

[Mal05] A. Malakho, M. Dussauze, E. Fargin, B. Lazoryak, V. Rodriguez and F. Adamietz, *"Crystallization and second harmonic generation in thermally poled niobium borophosphate glasses"*, Journal of Solid State Chemistry **178**, 1888-1897 (2005).

[Mao04] S. S. Mao, F. Quéré, S. Guizard, X. Mao, R. E. Russo, G. Petite and P. Martin, *"Dynamics of femtosecond laser interactions with dielectrics"*, Applied Physics A **79**, 1695-1709 (2004).

[Mar97] P. Martin, S. Guizard, Ph. Daguzan, G. Petite, P. D'Oliveira, P. Meynadier and M. Perdrix, *"Subpicosecond study of carrier trapping dynamics in wide-band-gap crystals"*, Physical Review B **55**, 5799-5810 (1997).

[Mas03] M. Masuda, K. Sugioka, Y. Cheng, N. Aoki, M. Kawachi, K. Shihoyama, K. Toyoda, H. Helvajian and K. Midorikawa, *"3-D microstructuring inside photosensitive glass by femtosecond laser excitation"*, Applied Physics A **76**, 857-860 (2003).

[Mil88] A. E. Miller, K. Nassau, K. B. Lyons and M. E. Lines, *"The intensity of Raman scattering in glasses containing heavy metal oxides"*, Journal of Non-Crystalline Solids **99**, 289-307 (1988).

[Mon98] S. Montant, A. Le Calvez, E. Freysz, A. Ducasse and M. Couzi, *"Time-domain separation of nuclear and electronic contributions to the third-order nonlinearity in glasses"*, Journal of the Optical Society of America B **15**, 2802-2807 (1998).

[Mon08] S. Montant, E. Freysz and M. Couzi, *"Nuclear and electronic contributions to the third-order nonlinearity in different glasses"*, Optics Communication **281**, 769-775 (2008).

[Mov95] I. A. Movtchan, R. W. Dreyfus, W. Marine, M. Sentis, M. Autric, G. Le Lay, N. Merk, *"Luminescence from a Si-SiO2 nanocluster-like structure prepared by laser ablation"*, Thin Solid Films **255**, 286-289 (1995).

[Oli04] T. Olivier, *"Contribution à la métrologie de l'indice de réfraction et de l'absorption non-linéaires dans le régime nanoseconde : amélioration de la méthode de Z-scan et simulations numériques"*, Thesis, University of Aix-Marseille 3, France (2004).

[Oro03] D. Oron, E. Tal and Y. Silberberg, *"Depth-resolved multiphoton polarization microscopy by third-harmonic generation",* Optics Letters **28** (2003).

[Oro04] D. Oron, D. Yelin, E. Tal, S. Raz, R. Fachima and Y. Silberberg, *"Depth-resolved structural imaging by third-harmonic generation microscopy*", Journal of Structural Biology, **147**, 3-11 (2004).

[Pan95] Z. Pan, S. H. Morgan, B. H. Long, *"Raman scattering cross-section and non-linear optical response of lead borate glasses"*, Journal of Non-Crystalline Solids **185**, 127-134 (1995).

[Pap07] D. G. Papazoglou, I. Zergioti and S. Tzortzakis, *"Plasma strings from ultraviolet laser filaments drive permanent structural modifications in fused silica"*, Optics Letters **32**, 2055-2057 (2007).

[Pas98] A. Pasquarello and R. Car, *"Identification of Raman Defect Lines as Signatures of Ring Structures in Vitreous Silica"*, Physical Review Letters **80**, 5145-5147 (1998).

[Pou08] B. Poumellec, M. Lancry, J. C. Poulin and S. Ani-Joseph, *"Non reciprocal writing and chirality in femtosecond laser irradiated silica"*, Optics Express **16**, 18354-18361 (2008).

[Raj06] P. P. Rajeev, M. Gertsvolf, E. Simova, C. Hnatovsky, R. S. Taylor, V. R. Bhardwaj, D. M. Rayner and P. B. Corkum, *"Memory in Nonlinear Ionization of Transparent Solids"*, Physical Review Letters **97**, 253001 (2006).

[Ray05] D. M. Rayner, A. Naumov and P. B. Corkum, *"Ultrashort pulse non-linear optical absorption in transparent media"*, Optics Express **13**, 3208-3217 (2005).

[Rei06] W. J. Reichman, D. M. Krol, L. Shah, F. Yoshino, A. Arai, S. M. Eaton and P. Herman, *"A spectroscopic comparison of femtosecond-laser-modified fused silica using kilohertz and megahertz laser systems"*, Journal of Applied Physics **99**, 123112 (2006).

[Riv04] C. Rivero, K. Richardson, R. Stegeman, G. Stegeman, T. Cardinal, E. Fargin, M. Couzi and V. Rodriguez, *"Quantifying Raman gain coefficients in tellurite glasses"*, Journal of Non-Crystalline Solids **345 & 346**, 396-401 (2004).

[Riv05] C. Rivero, K. Richardson, R. Stegeman, G. Stegeman, T. Cardinal, E. Fargin and M. Couzi, *"Characterization of the performance parameters of some new broadband glasses for Raman amplification"*, Proceedings VII European Society of Glass Science and Technology Conference, Athens, Greece, 25-28 April 2004, Glass Technology **46**, 80-84 (2005).

[Ri05bis] C. Rivero, *"High gain/broadband oxide glasses for next generation Raman amplifiers"*, Thesis, University of Central Florida, USA (2005).

[Riv05bisbis] C. Rivero, R. Stegeman, M. Couzi, D. Talaga, T. Cardinal, K. Richardson and G. Stegeman, *"Resolved discrepancies between visible spontaneous Raman cross-section and direct near-infrared Raman gain measurements in TeO_2-based glasses"*, Optics Express **13**, 4759-4769 (2005).

[Roy06] A. Royon, B. Bousquet, L. Canioni, M. Treguer, T.Cardinal, E. Fargin, D. G. Kim and S. H. Park, *"Third-harmonic generation microscopy for material characterization"*, Journal of the Optical Society of Korea **10**, 188-195 (2006).

[Roy07] A. Royon, L. Canioni, B. Bousquet, V. Rodriguez, M. Couzi, C. Rivero, T. Cardinal, E. Fargin, M. Richardson and K. Richardson, *"Strong nuclear contribution to the optical Kerr effect in niobium oxide containing glasses"*, Physical Review B **75**, 104207 (2007).

[Sak00] Y. Sakurai, *"The 3.1 eV photoluminescence band in oxygen-deficient silica glass"*, Journal of Non-Crystalline Solids **271**, 218-223 (2000).

[Sak06] Y. Sakurai, *"Correlation between the 2.7 eV and 4.3 eV photoluminescence bands in silica glass"*, Journal of Non-Crystalline Solids **352**, 2917-2920 (2006).

[Sal06] A. Saliminia, N. T. Nguyen, S. L. Chin and R. Vallée, *"Densification of silica glass induced by 0.8 and 1.5 μm intense femtosecond laser pulses"*, Journal of Applied Physics **99**, 093104 (2006).

[San04] S. Santran, L. Canioni, L. Sarger, T. Cardinal and E. Fargin, *"Precise and absolute measurements of the complex third-order optical susceptibility"*, Journal of the Optical Society of America B **21**, 2180-2190 (2004).

[Sch01] C. B. Schaffer, A. Brodeur and E. Mazur, *"Laser-induced breakdown and damage in bulk transparent materials induced by tightly focused femtosecond laser pulses"*, Measurement Science and Technology **12**, 1784-1794 (2001).

[She95] Z. X. Shen, Z. P. Hu, T. C. Chong, C. Y. Beh, S. H. Tang and M. H. Kuok, *"Pressure-induced strong mode coupling and phase transitions in $KNbO_3$"*, Physical Review B **52**, 3976-3980 (1995).

[She04] M. Sheik-Bahae, *"Nonlinear Optics Basics: Kramers-Krönig Relations in Nonlinear Optics"*, Encyclopedia of Modern Optics, Academic Press, London (2004).

[Shi03] Y. Shimotsuma, P. G. Kazansky, J. Qiu and K. Hirao, *"Self-Organized Nanogratings in Glass Irradiated by Ultrashort Light Pulses"*, Physical Review Letters **91**, 247405 (2003).

[Shi05] Y. Shimotsuma, K. Hirao, J. Qiu and P. G. Kazansky, *"Nano-modification inside transparent materials by femtosecond laser single beam"*, Modern Physics Letters B **19**, 225-238 (2005).

[Sku98] L. Skuja, *"Optically active oxygen-deficiency-related centers in amorphous silicon dioxide"*, Journal of Non-Crystalline Solids **239**, 16-48 (1998).

[Smo99] S. Smolorz, F. Wise and N. F. Borrelli, *"Measurement of the nonlinear optical response of optical fiber materials by use of spectrally resolved two-beam coupling"*, Optics Letters **24**, 1103-1105 (1999).

[Ste03] R. Stegeman, L. Jankovic, H. Kim, C. Rivero, G. Stegeman, K. Richardson, P. Delfyett, Y. Guo, A. Schulte and T. Cardinal, *"Tellurite glasses with peak absolute Raman gain coefficients up to 30 times that of fused silica"*, Optics Letters **28**, 1126-1128 (2003).

[Sto73] R. H. Stolen and E. P. Ippen, *"Raman gain in glass optical waveguides"*, Applied Physics Letters **22**, 275-278 (1973).

[Sto92] R. H. Stolen, J. P. Gordon, W. J. Tomlinson and H. A. Haus, *"Raman response function of silica-core fibers"*, Journal of the Optical Society of America B **6**, 1159-1166 (1989).

[Str02] A. M. Streltsov and N. F. Borrelli, *"Study of femtosecond-laser-written waveguides in glasses"*, Journal of the Optical Society of America B **19**, 2496-2504 (2002).

[Stu96] B. C. Stuart, M. D. Feit, S. Herman, A. M. Rubenchik, B. W. Shore and M. D. Perry, *"Nanosecond-to-femtosecond laser-induced breakdown in dielectrics"*, Physical Review B **53**, 1749-1761 (1996).

[Sud01] L. Sudrie, M. Franco, B. Prade and A. Mysyrowicz, *"Study of damage in fused silica induced by ultra-short IR laser pulses"*, Optics Communications **191**, 333-339 (2001).

[Sun99] H.-B. Sun, Y. Xu, S. Matsuo and H. Misawa, *"Microfabrication and Characteristics of Two-Dimensional Photonic Crystal Structures in Vitreous Silica"*, Optical Review **6**, 396-398 (1999).

[Sza05] A. Szameit, D. Blömer, J. Burghoff, T. Schreiber, T. Pertsch, S. Nolte and A. Tünnermann, *"Discrete nonlinear localization in femtosecond laser written waveguides in fused silica"*, Optics Express **13**, 10552-10557 (2005).

[Tay07] R. S. Taylor, C. Hnatovsky, E. Simova, P. P. Rajeev, D. M. Rayner and P. B. Corkum, *"Femtosecond laser erasing and rewriting of self-organized planar nanocracks in fused silica glass"*, Optics Letters **32**, 2888-2890 (2007).

[Tay08] R. Taylor, C. Hnatovsky and E. Simova, , *"Applications of femtosecond laser induced self-organized planar nanocracks inside fused silica glass"*, Laser & Photonics Reviews **2**, 26-46 (2008).

[Tem06] V. V. Temnov, K. Sokolowski-Tinten, P. Zhou, A. El-Khamhawy and D. von ver Linde, *"Multiphoton Ionization in Dielectrics: Comparison of Circular and Linear Polarization"*, Physical Review Letters **97**, 237403 (2006).

[Tho85] J. Thomazeau, J. Etchepare, G. Grillon and A. Migus, *"Electronic nonlinear optical susceptibilities of silicate glasses"*, Optics Letters **10**, 223-225 (1985).

[Wil02] M. Will, S. Nolte, B. N. Chichkov and A. Tünnermann, *"Optical properties of waveguides fabricated in fused silica by femtosecond laser pulses"*, Applied Optics **41**, 4360-4364 (2002).

[Zou04] A. Zoubir, *"Towards direct writing of 3-D photonic circuits using ultrafast lasers"*, Thesis, University of Central Florida, USA (2004).

[Zou05] A. Zoubir, M. Richardson, L. Canioni, A. Brocas and L. Sarger, *"Optical properties of infrared femtosecond laser-modified fused silica and application to waveguide fabrication"*, Journal of the Optical Society of America B **22**, 2138-2143 (2005).

[Zou06] A. Zoubir, C. Rivero, R. Grodsky, K. Richardson, M. Richardson, T. Cardinal and M. Couzi, *"Laser-induced defects in fused silica by femtosecond IR irradiation"*, Physical Review B **73**, 224117 (2006).